Spin Crossover under Extreme Conditions: A Structural Approach

HELENA JANE SHEPHERD

Spin Crossover under Extreme Conditions: A Structural Approach

Helena J. Shepherd

Thesis submitted in part fulfilment of the requirements for the degree of
Doctor of Philosophy at Durham University

Department of Chemistry
Durham University
2009

Memorandum

The work described herein was carried out by Helena J. Shepherd at Durham University between October 2006 and November 2009 under the supervision of Dr. A.E. Goeta and Prof. J.A.K. Howard. This thesis is the work of the author, except where acknowledged by reference and has not been submitted for any other degree at this or any other university.

Statement of Copyright

Spin Crossover under Extreme Conditions: A Structural Approach

Submitted for the degree of Doctor of Philosophy by Helena J. Shepherd

Durham University

November 2009

Abstract

Structural studies of several iron complexes that show spin crossover (SCO) properties are presented and intrinsic links between the structure and properties have been established for these systems. X-ray diffraction experiments of samples under extremes of temperature and pressure and after irradiation with laser light have been performed to characterise the structure of these various compounds.

The incomplete thermal SCO observed in the dinuclear species [{Fe(bbp)$(NCS)_2$}$_2$4,4'-bipy]•2MeOH has been investigated, revealing a complex series of crystallographic phase transitions that result in a material with a mixture of high spin (HS) and low spin (LS) states that displays long-range order at low temperature. The meta-stable high spin (HS*) state that arises as a result of the Light Induced Excited Spin State Trapping (LIESST) effect has also been structurally characterised at 30 K. Further single crystal X-ray diffraction experiments at high pressure have shown that it is possible to achieve a complete spin transition to a fully LS state, which is not thermally accessible. Another species that shows crystallographic ordering of mixed spin states is an Fe^{III} complex with a hexadentate Schiff base ligand, which has been studied using both single crystal and powder diffraction techniques.

The structure of the photo-induced HS* state of [Fe(bapbpy)$(NCS)_2$] has been determined at 30 K from diffraction data which comprise contributions from both the HS* state and the residual LS component of the crystal, which is non-merrohedrally twinned.

The structure of [Fe(picen)$(NCS)_2$] has been determined at 30 K after a range of cooling speeds, showing that cooling of the sample results in partial population of the HS* state. The photo-induced HS* state, and that induced by thermal trapping are shown to be structurally similar.

A gradual spin transition has been identified purely from structural analysis in an Fe^{II} complex with a hexadentate N_6-donating ligand. The gradual nature of the spin transition may be attributed to the poor cooperativiy observed between iron centres.

This study shows how structural features can be used to gain insights into some of the more unusual aspects of the SCO phenomenon such as stepped spin transitions, ordered mixed spin intermediate phases, trapping of meta-stable states as a result of light irradiation or temperature and pressure-induced spin transitions.

Acknowledgements

My sincerest thanks to:

Andrés Goeta, for all his support, patience and friendship over the past three years. Thank you for giving me the freedom to explore my own ideas while still being there to answer the many silly questions I have asked. Thank you also for the coffee in the office and beers in Japan, I have been very lucky to have such a warm and friendly supervisor.

Judith Howard, for advice, support and generosity. Thank you for all the opportunities you have given me during the course of my PhD, they have been invaluable and will no doubt shape my future.

Philippe Guionneau, Patrick Rosa, Gábor Molnár, Sylvesyre Bonnet, Grace Morgan and Helge Müeller-Bunz for providing many samples which have been challenging but ultimately fascinating and for making my stays in Bordeaux, Toulouse and Dublin so enjoyable.

Keith Dillon and Pippa Monks, for providing me with no end of interesting and unusual crystals for me to hone my crystallographic skills!

The Olex2 team; Oleg Dolomanov, Horst Puschman and Richard Gildea not only for creating a program which has made my work during the last few years much more successful, but also for accommodating my suggestions and requests. And thanks for Thursdays.

Mike Probert, for listening to my often unintelligible questions and not always laughing at me. Thanks for all your help with machine and high-pressure related issues, for being a great friend and for sharing so many good times and words of wisdom in Japan, Erice and everywhere else.

Mike Turner, for encouraging me to be myself and helping me get through some of the less exciting times. Thanks for making me laugh!

Hazel Sparkes, for advice in so many areas and a suitable amount of gossip to keep me entertained!

Kirsty Anderson, for wine, magazines, breaks from work and for being my twin. Almost.

Phil Dyer, for proof reading and listening to me complain about most things on far too many occasions, and for all the pints of Big Lamp.

The friends I made in Durham, Bath, Indiana, Southampton and all over the world. Thank you for contributing so much fun to my life, I hope the fun continues for many years to come.

My family, for their love and support, especially Mum and Dad, who have given me so much.

Contents

List of Figures

List of Tables

1 Introduction to Spin Crossover

1.1 Ligand Field Theory

Ligand field theory is a form of Molecular Orbital (MO) theory specifically applied to transition metal systems and can be used to help understand bonding, reactivity and structural features of transition metal (TM) complexes. In this ligand field theory (LFT) approach, the metal centre is regarded as a positive point charge, with the ligands considered as negative point charges. According to LFT, electrons located in the d-orbitals of TMs are energetically degenerate until placed into a non-spherical ligand field, whereupon the relative energies of these electrons change depending on the extent of interaction with the ligands (Figure 1.1). Electrons in d-orbitals that point directly toward the ligands will be raised in energy, while those which are oriented between the ligands will be lowered in energy relative to the barycentre. However, it should be noted that the total energy of the system when all orbitals are fully occupied will not change.

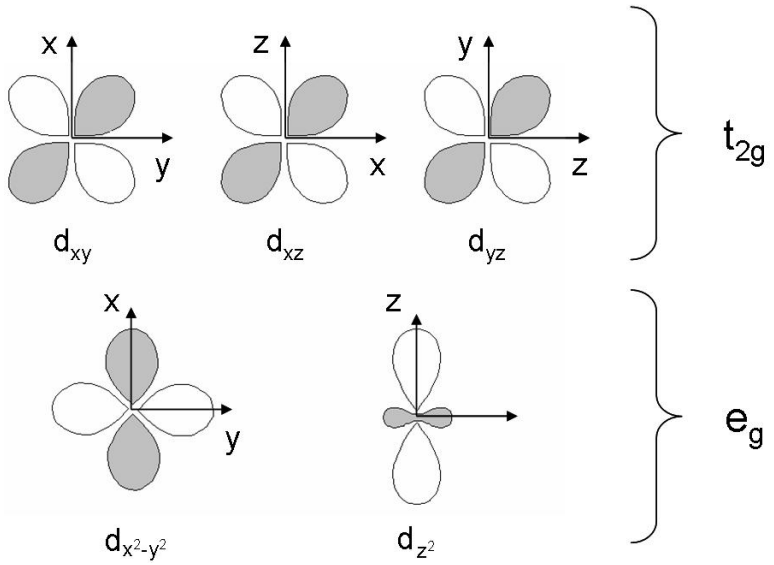

Figure 1.1. The orientation of the 5 d-orbitals of a transition metal relative to a Cartesian coordinate system

Arguably the simplest case explained by LFT is that of an octahedral TM complex, and it is this case that has most relevance to Spin Crossover (SCO). If ligands are placed at the corners of an octahedron as shown in Figure 1.2 it is clear that the d_{xy}, d_{xz} and d_{yz}

orbitals (the t_{2g} subset) will be lowered in energy as they lie between the axes, while the $d_{x^2-y^2}$ and d_{z^2} orbitals (e_g subset) will be raised in energy as a result of electron – electron repulsion.

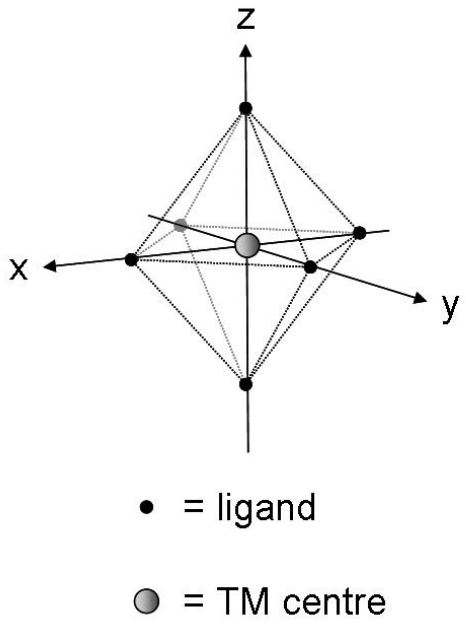

Figure 1.2. Transition metal at the centre of on octahedral ligand field

The effect on the d-orbitals of placing a metal ion into an octahedral ligand field is shown in Figure 1.3. The resulting energy difference between the t_{2g} and e_g subsets is known as ligand field splitting (Δ_{oct}) and its magnitude is influenced by the type and oxidation state of the metal, as well as the nature of the ligands. In the case of a specific metal ion, it is the nature of the ligand alone that dictates the size of this energy difference. Strong field ligands such as CO and CN^- result in a large Δ_{oct}, while weak field ligands such as halides result in a smaller energy difference. For a given ligand set[1] and metal ion Δ_{oct} depends on metal-ligand distance (r).

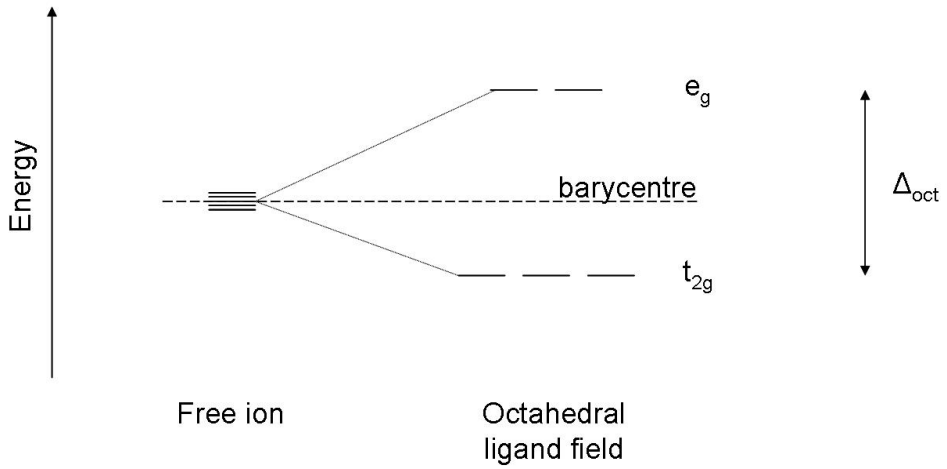

Figure 1.3. The effect on the relative energy of the d-orbitals of placing a TM ion into an octahedral ligand field

The order of occupation of the d-orbitals by electrons is determined by the magnitude of Δ_{oct} and the energy required to spin-pair electrons within an orbital (the pairing energy, P). If Δ_{oct} is larger than P, the electrons will fill the d-orbitals according to the Aufbau Principle, meaning that the lower energy t_{2g} subset will be completely filled before filling the higher energy e_g set. If Δ_{oct} is smaller than P, the d-orbitals (in both t_{2g} and e_g sets) will become singly occupied prior to spin-pairing of electrons within the same orbital, in accordance with Hund's Rules. In the case of metal ions with d^4 – d^7 configuration this can lead to two different configurations, the high spin (HS), which has the maximum spin multiplicity, and the low spin (LS), which has the minimum spin multiplicity possible for that system. These two cases are shown in Figure 1.4, using the example of a d^6 metal ion such as Fe^{II}.

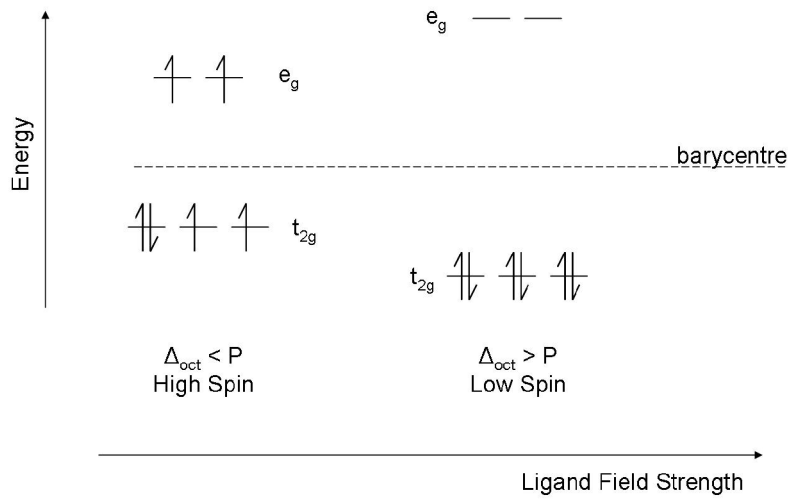

Figure 1.4. Effect of ligand field strength on the magnitude of Δ_{oct} and the occupation of the d-orbitals for the case of a d^6 metal ion

There are a number of magnetic, structural and optical differences between HS and LS metal ions. In the HS state there is a greater number of unpaired electrons than in the LS state, leading to a greater paramagnetic contribution to the complex's magnetic moment. In the case of a d^6 ion the low spin state is fully diamagnetic and the high spin state has four unpaired electrons, resulting in very significant paramagnetism.

It can be shown using MO theory that the e_g subset of orbitals is anti-bonding in nature, while the t_{2g} set is largely non-bonding. Consequently, increased occupation of the e_g orbitals (as in the case of the HS state) will effectively weaken and concomitantly lengthen the metal-ligand bond.[1] For the case of an octahedral Fe^{II} ion bearing six nitrogen based donor atoms the Fe – N bonds are ~ 2.2 Å and ~ 2.0 Å in the HS and LS states respectively.[2] The large difference in bond lengths between the two states can be distinguished using X-ray diffraction (XRD) techniques allowing identification of the spin state based on structural studies. Figure 1.5 shows the effect of the difference in orbital occupation between the HS and LS states on the size of the coordination octahedron. In the case of Fe^{II} this volume[2] is expected to be ~ 13 $Å^3$ in the HS state, while in the LS state it is closer to ~ 10 $Å^3$. There is also a difference in the coordination geometry of the metal ion between spin states, with the HS complex being more distorted from a regular octahedron than the LS complex.

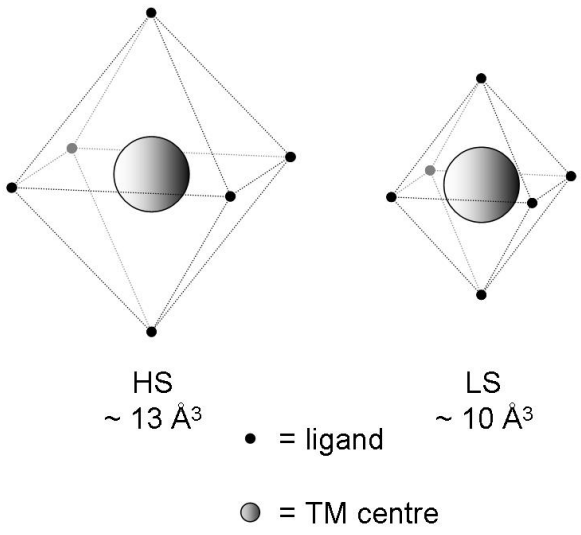

Figure 1.5. Illustration of the relative size of the coordination octahedron of a transition metal in the high spin and low spin states

1.2 Thermal Spin Crossover

Prior to the 1930s it was believed that the only way to alter the spin state of a metal ion was to change the ligand (and hence the ligand field strength) to one that favoured the other state.[3] However, a process called Spin Crossover (SCO), allows for a change of spin state not by a modification to the ligand, but rather by altering the sample environment, for example by changing the temperature of the system. This is possible when the difference in zero-point energy between the HS and LS states (ΔE^0_{HL}) is approximately equal to the thermal energy, i.e. $\Delta E^0_{HL} = E^0_{HS} - E^0_{LS} \approx k_B T$. [1,4,5] This is shown schematically in Figure 1.6.[1,3]

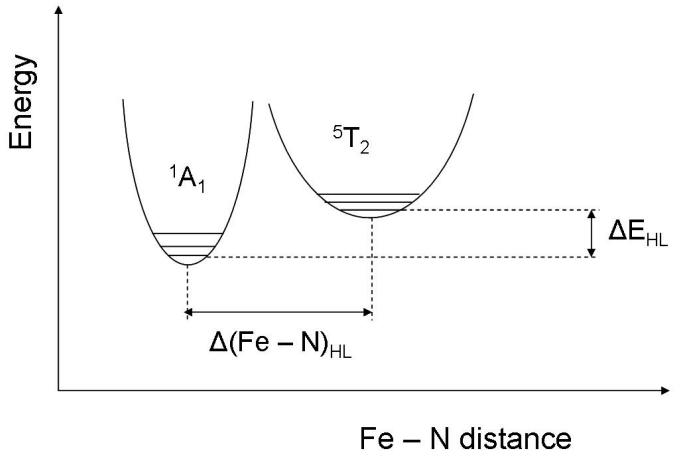

Figure 1.6. Potential wells for the HS ($^5T_2$) and LS ($^1A_1$) states in a Fe^{II} spin crossover system as a function of the Fe - N bond distance

Since the first reports of spin crossover systems in the literature,[5] much research has been directed towards understanding the phenomenon. Amongst the most commonly studied systems are those that have Fe^{II} in an N_6 coordination environment, where the nitrogen donor atoms are part of heterocyclic rings or *N*-thiocyanato groups,[4] although examples of many other metal ligand combinations are known to have the potential for spin crossover behaviour. It has also been observed that a variety of stimuli other than temperature may also produce a change in the spin state of the system. Pressure,[6,7] light irradiation,[8,9,10] hard X-rays[11] and external magnetic field[12] all have the potential to induce spin transitions in certain transition metal systems.

1.2.1 Classifying SCO Systems

The temperature at which a spin crossover material consists of high spin and low spin sites in an equal ratio[5] is called $T_{½}$. This value is often quoted as the temperature at which SCO occurs; in the case of simple, complete, single-step spin transition this can be a useful quantity to describe the behaviour of the system. However, more information is required to describe fully a material that shows more complex features such as broad, stepped or incomplete transitions.

Therefore, when discussing the behaviour of a spin crossover material it is important to consider not only $T_{½}$, but also the degree of cooperativity observed in the system, often attributed as the cause of these more complex features. The character of the

cooperative effects that govern the nature of spin crossover systems has been the subject of some debate. Spiering and co-workers proposed the so-called 'elasticity theory' to explain the nature of the cooperative effects in spin crossover systems.[13] This theory suggests that the highly cooperative nature of some spin transitions is a result of the large difference in the metal – ligand bond distance between the HS and LS states. Such a considerable difference at the metal centre will lead to a 'point defect' that will act as a kind of internal pressure – or 'image pressure' – which is felt equally by all SCO centres within the lattice. It is believed that this pressure is spread throughout the lattice *via* long-range electron-phonon coupling interactions. The result is a 'snow-ball' effect, making the overall transition much more abrupt than if no interactions were taking place.

It has been suggested that cooperativity relies heavily on intermolecular interactions to connect the metal centres throughout the lattice.[14] There are many solid state interactions which may be considered as promoting cooperativity, including hydrogen bonding, π-π stacking and Van der Waals interactions.[15,16] These increase the cohesion of the lattice, enabling the long range interactions to propagate the spin transition throughout the material. This result has led some to attempt the synthesis of materials that involve multiple SCO centres linked through direct covalent bonding, such as multinuclear molecular systems and coordination polymers, which extend infinitely in 1-, 2- or 3-dimensions.[17,18,19]

Spin transition curves help to visualise the different type of spin crossover behaviour observed in the solid state that occur largely as a result of cooperative interactions. These curves consist of a plot of the molar fraction of the high spin component (γ_{HS}) as a function of temperature and can be derived from measurements of physical properties such as magnetism (susceptibility measurements), nuclear environment (Mössbauer spectroscopy), colour (UV-vis spectroscopy) and bond lengths and other structural features (diffraction techniques). Figure 1.7 shows a series of spin transition curves that are most commonly observed in crystalline materials.[20,21]

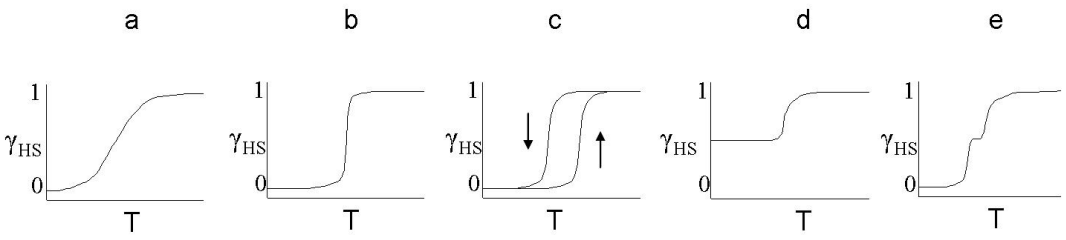

Figure 1.7. Spin transition curves for the most frequently observed types of transition. Molar fraction of the high spin species (γ_{HS}) as a function of temperature (T)

Perhaps the simplest system to consider is that in which very few cooperative interactions between metal centres are present. The result is a very gradual spin transition (Figure 1.7a), which may occur over several tens or hundreds of Kelvin. This kind of gradual transition is also observed in solution, and may be considered as a Boltzmann distribution across the available spin states, randomly distributed throughout the crystal. Where cooperative interactions have a strong effect on the SCO process, abrupt transitions (Figure 1.7b) are observed often accompanied by hysteresis (Figure 1.7c), which is when the transition occurs at a higher temperature on warming than on cooling. This kind of hysteretic behaviour is important to potential applications for these systems as it represents a form of molecular bistability, which is discussed in more detail in section 1.7. As there are two temperatures at which the ratio of HS:LS states is equal it is necessary to define two values of $T_{½}$, one recorded on cooling ($T_{½}\downarrow$), the other on warming ($T_{½}\uparrow$). It is possible for spin crossover processes to be incomplete (Figure 1.7d), where only some of the TM centres undergo spin crossover, or stepped (Figure 1.7e), where SCO centres undergo the spin transition at distinct temperatures, separated by an intermediate state that contains both HS and LS sites. In these cases the concept of $T_{½}$ could again be ambiguous and so a critical temperature (T_c) may be quoted. This represents the temperature at which the ratio of HS:LS states is equal when considering only those that do undergo a spin transition in the specified temperature range.[20,21]

Evidence for cooperative spin crossover effects in the solid state has been gathered through metal dilution experiments. This involves replacement of some of the spin crossover metal centres with a different metal that has no magnetic contribution, for example Zn^{II}, which has d^{10} configuration. Zn^{II} will not undergo a spin transition and hence no 'point defect' will be created at that site. With increasing doping the

transition becomes more gradual and is shifted to lower temperature. Eventually the distribution will resemble that of a Boltzmann distribution as all cooperative effects are negated.[22]

1.3 Stepped Spin Crossover

Stepped spin crossover has been known to exist since the late 1960s.[23] There are some classes of systems where this behaviour is markedly more common, for example the family of dinuclear bipyrimidine (bpym)[24] bridged Fe^{II} species, and analogous 3,5-bis(pyridin-2-yl)pyrazolate (bpypz) and 4,7-phenanthroline-5,6-diamine (phdia) bridged complexes.[25] Mononuclear complexes also show stepped transitions but are somewhat less common in the literature.

Questions raised by the stepped spin crossover phenomenon concern the structural and magnetic nature of the intermediate state, and what implications this has for the mechanism of spin crossover in these species. These questions are by no means trivial to answer, and it should be stated that the structure of the complex in all spin states, has an impact on how the structure of the intermediate phase is interpreted.

A system (mono or multi-nuclear) that has more than one crystallographically distinct SCO site prior to a stepped transition may be interpreted in terms of the individual sites having different intermolecular interactions and hence slightly different ligand field environments or cooperative effects. That such TM sites may undergo spin crossover at somewhat different temperatures is no surprise. Such behaviour has been observed in the mononuclear system $[Fe(btr)_3](ClO_4)_2$, where btr = (4,4'-bis-1,2,4-triazole).[26] In this complex the high temperature phase consists of two independent HS sites, one of which undergoes a spin transition at ~222 K. The intermediate phase, with one site in each of the HS and LS sites, is stable until ~184 K, at which point the second iron site becomes low spin. The three phases are isostructural across the investigated temperature range and as such the stepped ST behaviour may be considered a product of the packing forces that cause the iron sites to be inequivalent.

In cases where all SCO centres are crystallographically equivalent prior to the spin transition, it is clear that a more complex model of cooperativity is required to explain stepped spin crossover behaviour. Theoretical studies incorporating only the long-range elastic interactions which were used by Spiering to explain cooperative

behaviour in single-step systems[13] cannot predict 2-step behaviour.[27] As a result, models have been developed that introduce short-range anti-ferromagnetic interactions, which are strong enough in some complexes to compete with the long-range interactions to produce unusual SCO phenomena including stepped transitions. These models tend to be based on sublattices of HS and LS sites, where interactions within each sublattice are allowed to differ from those between them.[28] However, if this sublattice model is correct, one would expect to observe superlattice reflections using X-ray diffraction techniques at temperatures equating to the plateau in the magnetic behaviour. A thermodynamic model was thus developed, incorporating the idea of competition between long-range ferromagnetic and short-range antiferromagnetic interactions, in an attempt to explain systems that do not show this crystallographic ordering of the intermediate state.[29]

1.3.1 Dinuclear Stepped Spin Crossover

In dinuclear species, where direct covalent bonding connects spin crossover centres, short-range antiferromagnetic interactions between metals are expected to be relatively strong and may be of a similar order to long-range cooperative elastic interactions. As such, these species are perhaps more likely to undergo stepped spin transitions. The intermediate state in dinuclear systems may consist of mixed spin HS-LS molecules or molecules in which both metals have the same spin state. In either case the spin states may be crystallographically ordered, located in domains or randomly distributed throughout the crystal.

The {[Fe(L)$(NCE)_2$]$_2$bpym} family of complexes (where L = bpym or 2,2'-bithiazoline(bt), E = S, Se) (Figure 1.8) has been shown to undergo stepped spin transitions, with a plateau corresponding to approximately 50% of the Fe centres becoming LS.[24,30,31] The question as to whether the intermediate phase consists of HS-LS pairs of molecules where both Fe centres in the molecule posses the same spin state has been addressed using Mössbauer and calorimetric measurements. By analogy to the related [{Fe(phdia)$(NCS)_2$}$_2$(phdia)] system,[32] these methods have confirmed the hypothesis of the presence of HS-LS mixed spin molecules in the intermediate phase.[23] Indeed, it has been shown in studies using the application of hydrostatic pressure that HS-LS molecules are preferentially formed in the intermediate phase for these systems.[33] In the case of {[Fe(bt)$(NCE)_2$]bpym}, the volume change of one iron centre

in the molecule upon SCO leads to an increase of the energy gap between the HS and the LS levels of the second iron site, leading to a shift of the crossover temperature of the second centre towards higher temperatures, generating a two-step spin transition.[34]

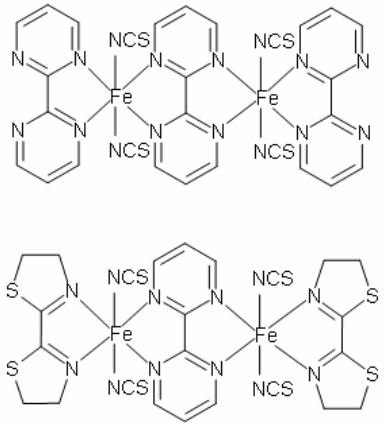

Figure 1.8. {[Fe(bpym)(NCS)$_2$]bpym} (top) and {[Fe(bt)(NCS)$_2$]bpym} (bottom)

Differentiation between HS-LS units and domains of HS-HS/LS-LS molecules is relatively simple using single crystal diffraction, but as these species could not be characterised in this manner a new Mössbauer technique was developed using applied magnetic field to differentiate between HS and LS sites on a microscopic scale.[35] The stabilisation of these HS-LS units had been attributed to the interplay between cooperative intermolecular interactions and anti-ferromagnetic intra-molecular coupling between Fe centres.[25] Subsequent crystallographic studies revealed that although each molecule contains one HS and one LS ion, these molecules are randomly oriented throughout the lattice, resulting in a mixed spin phase that does not show long range ordering.[36]

The opposite case in which the intermediate state in a dinuclear stepped spin crossover consists of molecules that are entirely HS or LS has also been identified for [{Fe(NCBH$_3$)(4phpy)}$_2$(μ-bpypz)$_2$][37] (Figure 1.9). In this example, the intermediate state was characterised unambiguously using single crystal XRD, and revealed alternating chains of HS-HS and LS-LS dinuclear units throughout the crystal lattice as a result of first order phase transitions either side of the plateau temperature range. While the fully HS and fully LS phases were isostructural, the intermediate phase has a unit cell of twice the volume; the space group was the same (P$\bar{1}$) in all phases. The authors

attributed the stability of the intermediate phase to strong intermolecular interactions within the system, *i.e.* antiferromagnetic interactions between molecules are stronger than those between ions within each individual molecule as a result of these strong non-bonding interactions. In this system there is long range ordering of spin states throughout the crystal.

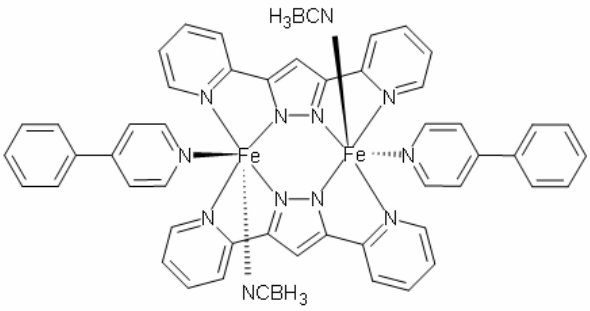

Figure 1.9. [{Fe(NCBH$_3$)(4phpy)}$_2$(μ-bpypz)$_2$]

1.3.2 Mononuclear Stepped Spin Crossover

One of the earliest mononuclear stepped SCO materials to be discovered was [Fe(2-pic)$_3$]Cl$_2$•EtOH and has since become the most widely studied.[38,39,40] The complex cation in this species is shown in Figure 1.10. There is a plateau in the magnetic spin transition between 114 and 122 K, indicating a stable intermediate spin state. For some time it was believed that there was no crystallographic phase transition and the structure was isomorphous at all temperatures. Indeed it was studies of this species and the perceived absence of a crystallographically ordered intermediate state that prompted the development of the thermodynamic model to describe stepped SCO.[29] Subsequent detailed X-ray diffraction studies using synchrotron radiation revealed the presence of two first order crystallographic phase transitions separated in temperature by an intermediate mixed spin (MS) phase showing long range order of HS and LS sites.[39] While the HS and LS phases are isostructural, the MS phase had a unit cell with twice the volume. The observed ordering of spin states supports the sublattice model described above.

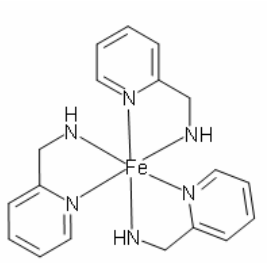

Figure 1.10. $[Fe(2\text{-}pic)_3]^{2+}$ ion

A recent example of stepped spin crossover behaviour in a mononuclear species is given by $[Fe(bapbpy)(NCS)_2]$[41,50] (Figure 1.11). This compound shows a stepped spin transition, from 100% HS → mixed spin phase (⅓ HS, ⅔ LS) → 100 % LS. Each step is accompanied by a crystallographic phase transition, with the mixed spin phase showing long range magnetic and structural order. Again, the stabilisation of the intermediate mixed spin state is attributed to the competition between long-range and short-range interactions within the crystal.

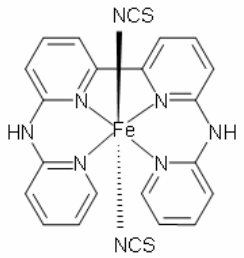

Figure 1.11. $[Fe(bapbpy)(NCS)_2]$

1.4 Pressure-Induced SCO

The phenomenon of spin crossover at high pressure is fundamental to some of the processes that take place in the Earth's lower mantle. Pressures of up to 100 GPa cause the iron atoms in perovskite, post-perovskite and magnesiowüstite to undergo a spin transition.[42,43,44] While this may have vital implications to the way in which geologists and geophysicists understand and interpret mantle dynamics, high pressure studies have also been used to understand and manipulate the spin crossover process in molecular-based systems.[45]

Higher pressures raise the energy of the $^5T_2$ (HS) potential well, as shown in Figure 1.12. The result is a decrease in activation energy (ΔW_{HL}) and an increase in the difference in zero point energy (ΔE_{HL}), thus favouring the low spin state.[46]

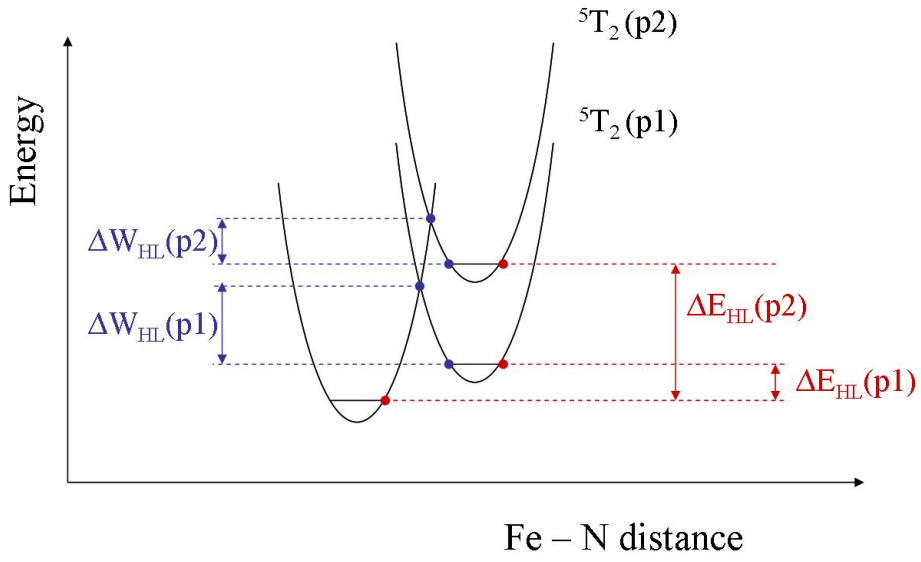

Figure 1.12. Effect of pressure (p) on the HS and LS potential wells in Fe^{II}, where (p2) > (p1)[46]

As stated previously, molecules in the low spin state occupy a smaller volume in the solid state than those in the high spin state; high pressure studies take advantage of this difference in volume as the LS state is favoured as pressure increases. The first high-pressure studies of spin crossover materials were carried out in the 1960s and focussed on a series of Fe^{III} complexes.[47] Since then many SCO systems have been studied under the influence of applied pressure. In general the application of pressure raises the temperature of the spin transition, causes it to become more gradual and decreases the width of hysteresis loops. For complexes with an $Fe^{II}N_6$ core the temperature of the spin transition increases by ~15 K/kbar, although exceptions to this behaviour are known.[48]

In some species the hysteresis width has been shown to increase, which is believed to occur as a result of a pressure induced crystallographic phase transition within the sample.[46] This behaviour is demonstrated by the compounds $[Fe(PM\text{-}BiA)_2(NCS)_2]$ and $[Fe(PM\text{-}AzA)_2(NCS)_2]$, where PM-BiA = (N-(2'-pyridylmethylene)-4-aminobiphenyl) and PM-AzA = (N-(2'-pyridylmethylene)-4-(azophenyl)aniline, (Figure 1.13).[49]

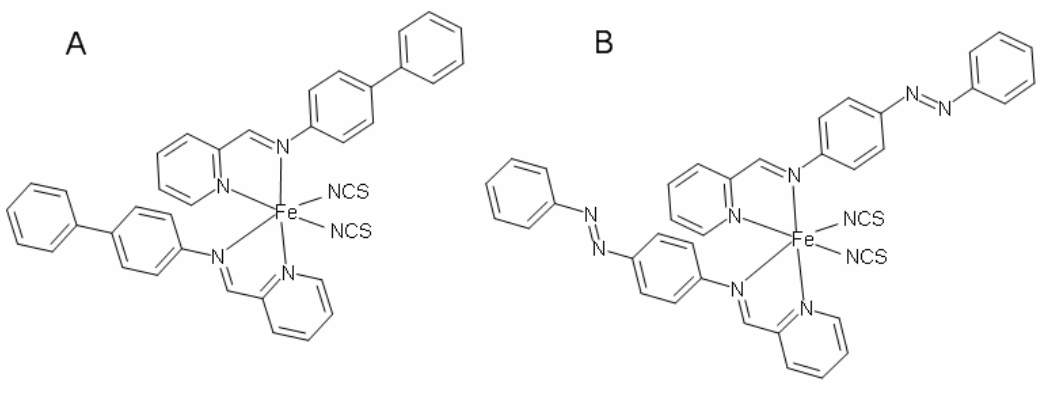

Figure 1.13. [Fe(PM-BiA)$_2$(NCS)$_2$] (A) and [Fe(PM-AzA)$_2$(NCS)$_2$] (B)

[Fe(PM-BiA)$_2$(NCS)$_2$] undergoes an abrupt thermal spin transition at ambient pressure, which is accompanied by a small (~5 K) hysteresis loop. $T_{½}$ increases and the hysteresis is reduced with increasing pressure up to 6.1 kbar, above which a reversible crystallographic phase transition causes the hysteresis loop to widen significantly.[45,49] [Fe(PM-AzA)$_2$(NCS)$_2$] undergoes a gradual thermal spin transition, also with a slight hysteresis. The temperature of the spin transition changes from 186 K at ambient pressure, to 210 K at 2.5 kbar, and to temperatures well in excess of 300 K at 10.8 kbar.[49] Here it is apparent that fine detail in the structure of the compound has a significant impact on the properties of the material.

High pressure may also induce spin transitions in complexes that do not show thermal SCO properties, for example in [Fe(abpt)$_2$(NCS)$_2$], where abpt = 4-amino-3,5-bis(pyridin-2-ly)-1,2,4-triazole). In this case, ΔE_{HL} (Figure 1.12) changes from a negative to a positive value, *i.e.* the ground state changes from the high spin to the low spin state.[45] Somewhat more difficult to explain is the effect of pressure on [Fe(bapbpy)(NCS)$_2$], in which a partial spin transition is suppressed.[50] This species has yet to be structurally characterised at high pressure and consequently the possible structural origin of this unusual behaviour is not well understood.

High-pressure studies can be used to elucidate the effect of structure and phase transitions upon spin crossover properties. The change in molecular volume observed upon spin crossover plays an important role in cooperative elastic interactions and can be influenced by externally applied pressure, thus shedding light on the nature of these interactions in the solid state.

1.5 Light Induced Excited Spin State Trapping

More than fifty years after the first observation of spin crossover, Decurtins and co-workers published their discovery of a previously unknown physical process involving the population of a meta-stable high-spin (HS*) state from the thermal LS species *via* irradiation with light.[51] This process was dubbed light induced excited spin state trapping, or the LIESST effect. The work initially focussed on $[Fe(ptz)_6](BF_4)_2$, although the LIESST effect has since been shown to be possible in many of the systems that undergo a thermal transition.[9,10,52]

The mechanism of LIESST in Fe^{II} complexes was first proposed in 1985[53] and was subsequently confirmed using optical spectroscopy, magnetic susceptibility measurements and theoretical studies.[54,55,56] It involves irradiating the sample with light of sufficient energy to populate the $^1T_1$ energy level via a spin-allowed transition from the $^1A_1$ ground state at low temperatures. This excitation is followed by rapid radiationless decay, known as intersystem crossing, from the $^1T_1$ to the $^3T_2$ level and subsequently to both the HS* $^5T_2$ state and back to the $^1A_1$ ground state. Radiative relaxation from the $^5T_2$ to the $^1A_1$ state is spin-forbidden and decay *via* thermal tunnelling is slow at low temperatures, leading to significant lifetimes for the HS* state.

It has also been observed that at low temperatures, the HS* state may be returned to the LS state using light of a different wavelength to that initially used to induce this meta-stable state. In this case excitation occurs from the $^5T_2$ to the ^5E state, with intersystem crossing to the $^3T_2$ state, again followed by the subsequent relaxation to both $^5T_2$ (HS) and the $^1A_1$ states. This process has been dubbed reverse LIESST.[52] A schematic illustration of both LIESST and reverse LIESST is shown in Figure 1.14. A typical spin transition curve for a complex showing a thermal spin transition and LIESST behaviour is shown in Figure 1.15.

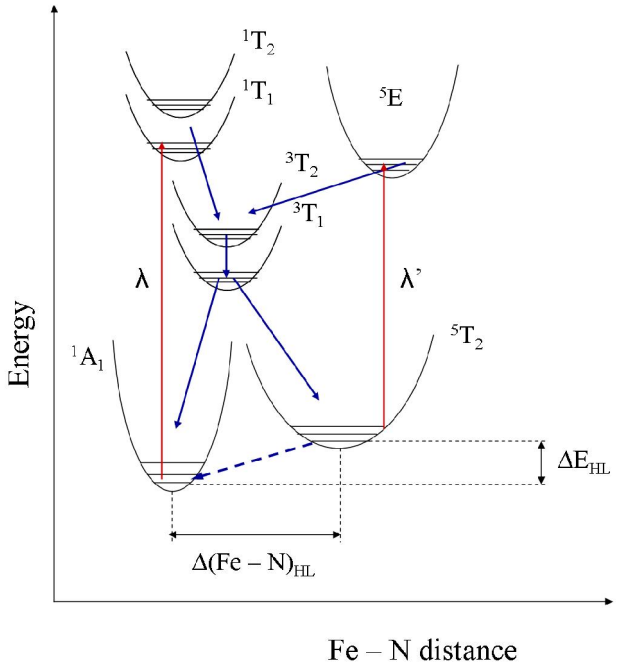

Figure 1.14. Mechanism of LIESST and reverse LIESST for a Fe^{II} ion.[24] Irradiation processes are shown in red, intersystem crossing processes are shown in blue, the dashed arrow represents the slow HS* → LS tunnelling process at low temperatures

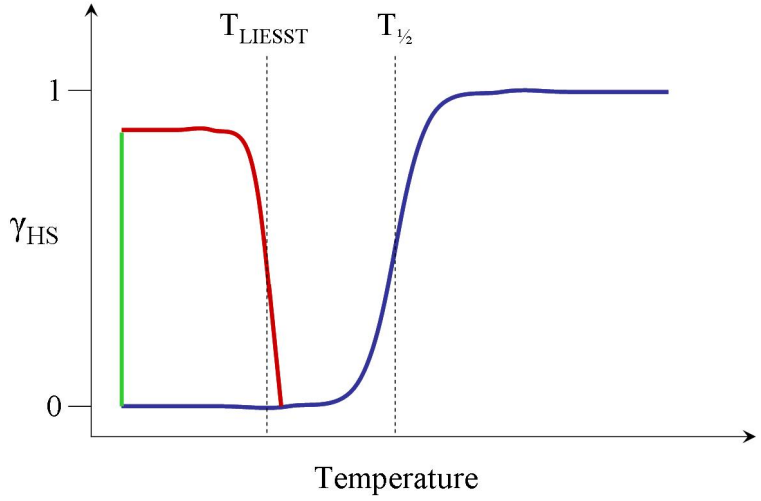

Figure 1.15. Typical spin transition curve for a complex that shows a thermal spin transition and LIESST behaviour. The mole fraction of high spin (χHS) decreases as a function of temperature on cooling (blue), increases during laser irradiation at constant temperature (green) and decreases on warming after the laser is switched off (red). $T_{½}$ and T_{LIESST} are defined in the text

For many Fe^{II} species the lifetime of the meta-stable high spin state at temperatures below 50 K ranges from hours[57] to weeks,[9] allowing enough time for a full structural characterisation of the HS* state using single crystal X-ray diffraction.

The HS* state will relax back to the LS ground state above a temperature characteristic to that compound, T_{LIESST}. T_{LIESST} is strictly defined as the minimum of the derivative of the magnetic product ($\chi_M T$) as a function of temperature, and is often used when discussing the LIESST process in individual compounds.[9] The value of T_{LIESST} is different for each compound, and in general functional operation at temperatures approaching room temperature is desirable in order for the possible technological applications of the LIESST effect to be realised. These potential applications will be discussed in more detail later in the chapter. The highest value of T_{LIESST} so far reported in a molecular species is 132 K for $[Fe(L)(CN)_2]\bullet H_2O$,[58,59] (Figure 1.16), showing that stabilisation of the HS* state is possible at relatively high temperatures.

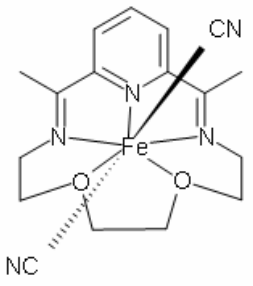

Figure 1.16. $[Fe(L)(CN)_2]$, where L = 2,13-dimethyl-6,9-dioxa-3,12,18-riazabicyclo[12.3.1]-octadeca- 1(18),2,12,14,16-pentaene

A study of more than 60 octahedral Fe^{II} SCO compounds has revealed trends in the photomagnetic behaviour, identifying a relationship between T_{LIESST}, $T_{½}$ and the type of ligand system in the complex, by plotting a graph of T_{LIESST} vs. $T_{½}$.[60] The general formula proposed by the authors is $T_{LIESST} = T_0 - 0.3\ T_{½}$ where T_0 is the value of T_{LIESST} when $T_{½}$ tends to 0 for a group of compounds related by a similar ligand system. T_0 (and hence T_{LIEST}) values for molecular species are smallest for complexes with six monodentate ligands and increase with denticity of the chelating ligands, as demonstrated in Figure 1.17. It is thus possible to have some degree of rationality in the design of new spin crossover complexes with a high T_{LIESST}.

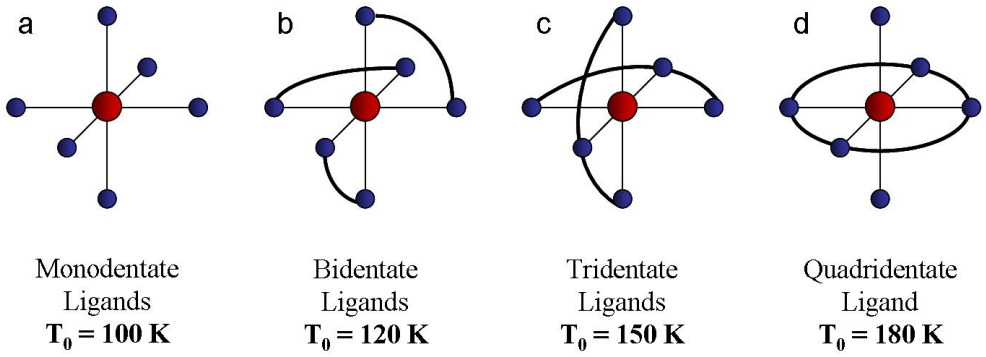

Figure 1.17. T_0 values for selected ligand systems[60]

In the case of $[Fe(L)(CN)_2](H_2O)$ (Figure 1.16), one of the iron – oxygen bonds associated with the macrocyclic pentadentate ligand breaks during the spin transition, leaving a ligand system described by that shown in Figure 1.17d. This complex shows the importance of structural investigations in the study of spin crossover and that rational design of spin crossover complexes with specific properties is not always straightforward.

It is worth noting here that it is also possible to switch between high spin and low spin states using laser irradiation within the hysteresis loop (centred at 216 K) of the thermal spin transition in $[Fe(L)(CN)_2](H_2O)$.[61] This effect is distinct from LIESST and descriptions of this effect in the literature are scarce, with only two other systems reported to show this unusual photomagnetic effect.[62,63,64,65] The process has been attributed to the cooperative character of the photoexcitation process.

1.6 Spin Crossover and Structure

Molecular structure and bulk properties are intrinsically linked and X-ray diffraction studies form an important part of many of the studies in this field. A number of parameters have been defined which help to quantitatively define the structure of the metal centre and relate these characteristics to features of the spin crossover properties. In addition to the bond lengths and volume of the coordination octahedron, described in section 1.1, the parameters Σ and Θ have also been identified as means of quantifying the distortion of the metal coordination octahedron.

1.6.1 The Σ Parameter

The Σ parameter is defined as the sum of the deviations from 90° of the 12 *cis* φ in the coordination sphere, shown in Figure 1.18.[2,66] In a regular octahedron these angles would all be 90° and hence Σ would be equal to zero. This value quantifies the distortion of the octahedral environment, which neither bond length, nor volume of the coordination octahedron can do alone. Due to the greater distortion of the metal centred octahedron when in the high spin state,[2] the value of Σ is spin state dependant and can be used to aid in the assignment of HS and LS sites. The value of Σ also depends on the nature of the ligand, but for the same complex, higher values are indicative of HS complexes, and lower values are associated with LS complexes. Variation in values of Σ between the HS and LS states[2] is typically between 30% and 55%.

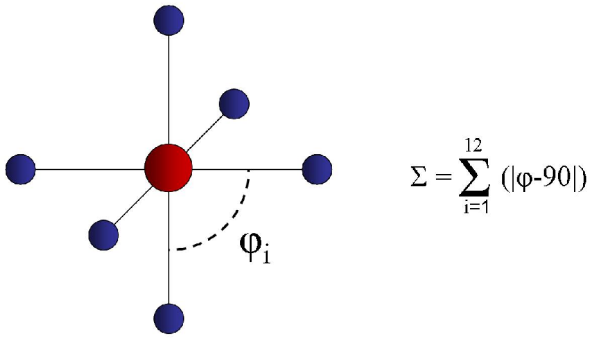

Figure 1.18. Definition of the structural parameter Σ, calculated from the 12 cis angles that are defined as right angles in a perfect octahedron

1.6.2 The Θ Parameter

The parameter θ is derived from the 'trigonal twist' motion of the opposite trigonal faces of an octahedron, and would be expected to be equal to 60° in an ideal octahedron.[67] This parameter was used to asses the specific distortion associated with the thiocyanate ligands in a series of $[FeL_n(NCS)_2]$ complexes (θ_{NCS}), which is a function of the intermolecular interactions in which these ligands were principally involved for this type of complex.[68] In all of the studied complexes the thiocyanate ligands were cis to each other and θ_{NCS} was defined as the opposite N – Fe – N angle to the NCS ligands, when viewed in an orientation such that each trigonal face contains one of these groups, as shown in Figure 1.19.

The related parameter Θ was developed for situations in which a more general measure of the octahedral distortion is required – one that is not related to the interactions associated with specific ligands.[68] Θ is the sum of the deviation from 60° of the 24 unique θ angles in an octahedron, as defined in Figure 1.19. While the magnitude of θ depends on the orientation of the octahedron, the value of Θ incorporates all 24 θ angles and as such is independent of orientation. Like Σ, Θ values are to some extent dependent upon the geometry of the ligating molecule and hence comparisons across a range of complexes with vastly differing ligand systems are not necessarily meaningful.

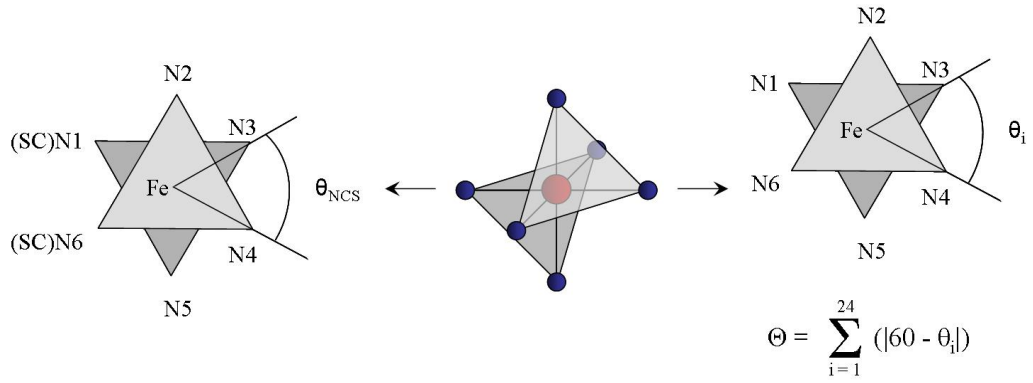

Figure 1.19. Definition of θ_{NCS} (left) and Θ (right), based on the 'trigonal twist' between opposite trigonal faces of an octahedron

Investigations have shown that as Θ increases, spin transitions in the $[FeL_n(NCS)_2]$ series become more abrupt, which has been attributed to a strong relationship between the distortion of the metal centre on spin crossover and cooperative interactions.[68] As part of the same study a positive correlation was also established between $\Delta\Theta_{HL}$ (the difference in Θ between HS and LS states) and T_{LIESST}. This relationship is may be understood in light of the link between Θ and the type of ligand system as described in Figure 1.17. This previous study serves to demonstrate that the link between structure and properties in spin crossover complexes is clearly intricate and deserving of attention.

1.7 Applications of Spin Crossover Materials

For the past 50 years, the advancing capability for miniaturisation of electronic devices has produced incredible advances in technology. A so-called 'top-down' approach has

been used to manufacture ever smaller components from silicon based materials, but there are technological and financial limits as to how long this miniaturisation can continue.[69] As a result, there has been much recent interest in nano-scale molecular materials that possess relevant properties for these applications - effectively a 'bottom-up' approach. One such promising area of research is that of spin crossover materials, potentially useful as molecular switches, as well as components in display devices, data storage and pressure sensors.[70]

The following sections discuss the properties required for these applications, the extent to which these properties are displayed by spin crossover materials and the advances needed for these materials to become functional components of these future technologies.

1.7.1 Molecular Switches

The definition of a molecular switch is that it possesses two states – an 'on' state and an 'off' state – so called molecular bistability.[70] This can be interpreted as binary code – the strings of 1s and 0s that are used for encoding of information in digital computing and communication systems. For usable technologies to be made from these systems the interconversion between on and off states must be repeatable many times without deterioration, the individual states must be accessible with simple input and readable output functions and switching between the states must be rapid. Furthermore these materials must be chemically stable on a surface or in a matrix, with the state of each switch being independent of that of its neighbours to ensure reliability of writing and readout functions.

The on and off states of a molecular switch are realised in spin crossover materials as the high spin and low spin states. The simplest input functions for switching between these states are temperature, pressure and light irradiation, as discussed previously. A detectable output function is shown by the differences in colour (absorption) or magnetic moment between the HS and LS states.

Multinuclear SCO systems provide the potential for more complex multistep molecular switches, where more than two states are accessible and hence more complex uses are possible.[71]

1.7.2 Data Storage

As in the case of molecular switches, systems with molecular-based memory must have two accessible states – on and off. The distinction is that species used in data storage must remain in the chosen state after the input function has been removed, until that piece of information is required.[70] This is shown by the LIESST and reverse-LIESST phenomena in spin crossover compounds, where switching between the LS and HS* states is possible using laser irradiation. The HS* state has long lifetimes at cryogenic temperatures, but unless T_{LIESST} can be substantially increased it is unlikely that this aspect of spin crossover could be successfully exploited in usable technologies.

Another way of achieving this memory effect is exploitation of the photomagnetic effect within the thermal hysteresis loop. There is one known system where it is possible to change the spin state of the system using laser irradiation at room temperature.[65] This system shows promising photoexcitation behaviour, but the hysteresis is only 14 K wide (centred around 298 K) and it has been suggested that for practical application these systems would have to show hysteresis of at least 100 K spanning the temperature range 253 K – 353 K.[9]

Hysteresis is the result of cooperative interactions between a series of molecules and consequently spin crossover materials designed for data storage consist of an array of SCO centres rather than individual sites used as molecular switches.[72] A thermal hysteresis loop in the dielectric constant of a spin crossover molecule is important for applications in molecular based memory devices. This has been observed at room temperature for several complexes and represents another step toward the application of these complexes in future technologies.[73]

Another interesting and unusual complex within this class of molecular based memory devices is $[Fe(HB(pyrazoyl)_3)_2]$,[74] which shows a deterioration in response after one thermal SCO cycle, but consistent behaviour thereafter. This type of system has been suggested as the starting point for development of molecular based read-only memory (ROM) devices, in which stored data cannot be overwritten.

1.7.3 Data Display Devices

The potential for SCO complexes to be used in display devices has been addressed by O. Kahn et al.[75] and J.-F Létard et al.[70] General requirements include a strong thermochromic response to the spin state change with good thermal reproducibility, room temperature operation and abrupt transitions. Iron 1,2,4-triazole derivatives have been studied in detail for this purpose and much work has gone into tuning the transition temperature of these species. The first approach to try to do this involved choosing a system which has a spin transition above room temperature and replacing a fraction of the Fe^{II} centres with metals such as Zn^{II}, which does not undergo a spin transition. While the transition temperature did vary as a function of metal dilution it had the undesirable side effect of severely dulling the thermochromic properties of these materials.

Another approach involved making "molecular alloys" in which mixed ligand systems were used to tune the temperature of the spin transition. By using a combination of different triazole ligands that produce high and low temperature transitions, it is possible to tune the transition to room temperature. Mixing counterions was also performed in a similar manner. Both of these approaches proved successful and one compound in particular, $[Fe(NH_2trz)_3](NO_3)_{1.7}(BF_4)_{0.3}$, shows a hysteresis of 60 K located across room temperature.[75]

A functioning display device has been created using triazole derivatives by J.-F Létard et al.[70] In this case the spin crossover materials are suspended in an ink which is printed onto a screen. A heating element is placed below the screen in combination with a mask incorporating the design of the visual display and when the temperature is increased the design is revealed.

1.7.4 Sensors

The temperature and pressure dependence of a spin transition has also led to interest in SCO complexes being developed as sensors. The coordination polymer $\{Fe(pmd)(H_2O)[Ag(CN)_2]_2\}(H_2O)$ (where pmd = pyrimidine) shows piezohysteresis at room temperature as well as the potential to tune the width and temperature of the thermal hystersis.[72] These properties demonstrate the requirements for both pressure and temperature based sensors. Both magnetic and spectroscopic studies revealed that

the thermal spin transition in this compound remains abrupt up to the highest investigated pressure of 0.34 GPa, which is a requirement for technological applications. The thermal hysteresis decreases slightly from 8 K at ambient pressure to 7 K at pressures between 0.19 GPa and 0.25 GPa. Between 0.25 GPa and 0.30 GPa the hysteresis opens up significantly to 31 K, assumed to be the result of a structural phase transition. On decreasing pressure this wide hysteresis is observed down to ~ 0.15 GPa, revealing the piezohysteresis is likely to be the result of a structural phase transition which occurs at a different points on the pressurisation and depressurisation curves.

The nature of this pressure-induced phase transition is not reported, but again shows the influence of structure on properties and deserves further investigation. Structural studies are of great importance to understanding the origin of the unusual spin crossover features in many species and could enable the rational design of SCO compounds which show these features for a wide range of applications.

1.8 Overview

This chapter has introduced the concept of spin crossover induced by changes in temperature, pressure and light irradiation and described the potential applications one can foresee for this class of materials. There are many fascinating features in the field of SCO, including cooperative effects and interactions, stepped spin transitions and structural phase transitions. X-ray diffraction techniques offer not only a means for identifying the spin state of the metal centres, but can also provide insights into the structural origins of many of these unusual aspects of solid state transition metal chemistry.

Chapter 2 details some of the more unusual crystallographic techniques employed during the course of this study; it presents not only the specific details of experiments performed, but also provides a more general introduction to some of these techniques. Chapters 3 to 8 describe the research carried out using these techniques, largely in relation to Fe^{II} complexes. The exception is Chapter 5, which describes a Fe^{III} complex as well as a brief introduction to the slight differences from the Fe^{II} case, associated with SCO in ferric systems. Final conclusions and suggested future work on these compounds are contained in Chapter 9. Appendix A details the courses and

conferences attended during the course of my doctoral studies and publications resulting from work presented within this manuscript. Appendix B contains tables of crystallographic data for all structures presented during the course of this investigation, along with crystallographic information files (cifs); it is located on a CD attached to the inside back cover of this manuscript.

---

[1] A. Hauser, P. Gütlich, H. A. Goodwin *Top. Curr. Chem*., 2004, **233,** 49

[2] P. Guionneau, M. Marchivie, G. Bravic, J.-F. Létard and D. Chasseau, *Top. Curr. Chem*., 2004, **234,** 97

[3] P. Gütlich, Y Garcia, H. A. Goodwin, *Chem. Soc. Rev*., 2000, **29**, 419

[4] P. Gütlich, A. Hauser, H. Spiering, *Angew. Chem. Int. Ed. Engl*., 1994, **33**, 2024 and references therein

[5] P. Gütlich, H. A. Goodwin *Top. Curr. Chem*., 2004, **233**:1-47 and references therein

[6] V. Ksenofontov, A. B. Gaspar, P. Gütlich, H. A. Goodwin *Top. Curr. Chem*., 2004, **235**:23-64 and references therein

[7] G. Molnár, T. Guillon, N. Ould Moussa, L. Rechignat, T. Kitazawa, M. Nardone and A. Bousseksou, *Chem. Phys. Lett*., 2006, **423**, 152

[8] S. Decurtins, P. Gütlich, C. P. Köhler, H. Spiering and A. Hauser, *Chem. Phys. Lett*., 1984, **105**, 1

[9] J.-F. Létard, *J. Mater. Chem*., 2006, **16**, 2550

[10] A. Hauser, P. Gütlich, H. A. Goodwin, *Top. Curr. Chem*., 2004, **234**, 155

[11] G. Vankó, F. Renz, G. Molnár, T. Neisius, and S. Kárpáti, *Angew. Chem. Int. Ed*., 2007, **46**, 5306

[12] A. Bousseksou, F. Varret, M. Goiran, K. Boukheddaden, J.-P. Tuchagues, P. Gütlich and H. A. Goodwin, *Top. Curr. Chem*., 2004, **235**, 65

[13] H. Spiering and N.Willenbacher, *J. Phys.: Condens. Mat*., 1989, **1**, 10089

[14] J. A. Real, A. B. Gaspar, V. Niel and M. Carmen Muñoz, *Coord. Chem. Rev*., 2003, **236**, 121

[15] B. Weber, E. S. Kaps, C. Desplanches, J.-F. Létard, K. Achterhold, and F. G. Parak, *Eur. J. Inorg. Chem.*, 2008, 4891

[16] R. Pritchard, C. A. Kilner and M. A. Halcrow, *Chem. Commun.*, 2007, 577

[17] Y. Garcia, V. Niel, M. Carmen Muñoz and J. A. Real, *Top. Curr. Chem.*, 2004 **233**:229-257 and references therein

[18] K. S. Murray and C. J. Kepert, *Top. Curr. Chem.* 2004 **233**, 195 and references therein

[19] K. S. Murray, *Aust. J. Chem.*, 2009, **62**, 1081

[20] H. A. Goodwin, Y. Garcia and P. Gütlich, *Chem. Soc. Rev.*, 2000, **29**, 419

[21] P. Gütlich and H. A. Goodwin, *Top. Curr. Chem.*, 2004 **233**, 1

[22] P. Gütlich, A. Hauser and H. Spiering, *Angew. Chem. Int. Ed. Engl.*, 1994, **33**, 2024 and references therein

[23] J. A. Real, H. Bolvin, A. Bousseksou, A. Dworkin, O. Kahn, F. Varret and J. Zarembowitch, *J. Am. Chem. Soc.* 1992 **114**, 12, 4650 and references therein.

[24] J. A. Real, J. Zarembowitch, O. Kahn, and X. Solans, *Inorg. Chem.*, 1987, **26**, 2939

[25] J.A. Real, A.B. Gaspar, M.C. Muñoz, P. Gütlich, V. Ksenofontov, H. Spiering, *Top. Curr. Chem.*, 2004, **233**, 167

[26] Y. Garcia, O. Kahn, L. Rabardel, B. Chansou, L. Salmon, and J. P. Tuchagues, *Inorg. Chem.*, 1999, **38**, 4663

[27] H. Spiering, T. Kohlhaas, H. Romstedt, A. Hauser, C. Bruns-Yilmaz, J. Kusz and P. Gütlich *Coord. Chem. Rev.*, 1999, **190–192**, 629

[28] N. Sasaki and T. Kambara, *Phys. Rev. B.*, 1989, **40**, 4, 2442

[29] H. Romstedt, H. Spiering and P. Gütlich, *J. Phys. Chem Solids*, 1998, **59**, 8, 1353

[30] J.-F. Létard, J. A. Real, N. Moliner, A. B. Gaspar, L. Capes, O. Cador, and O. Kahn *J. Am. Chem. Soc.*, 1999, **121**, 10630

[31] J. A. Real, I. Castro, A. Bousseksou, M. Verdaguer, R. Burriel, M. Castro, J. Linares, and F. Varret, *Inorg. Chem.*, 1997, **36**, 455

[32] V. Ksenofontov, A. B. Gaspar, V. Niel, S. Reiman, J. A. Real, and P. Gütlich, *Chem. Eur. J.*, 2004, **10**, 1291

[33] V. Ksenofontov, A. B. Gaspar, J. A. Real, and P. Gütlich, *J. Phys. Chem. B*. 2001, **105**, 12266

[34] D. Chernyshov, H.-B. Bürgi, M. Hostettler and K. W. Törnroos, *Phys. Rev. B*, 2004, **70**, 094116

[35] V. Ksenofontov, H. Spiering, S. Reimen, Y. Garcia, A. B. Gaspar, N. Moliner, J. A. Real and P. Gütlich, *Chem. Phys. Lett.*, 2001, **348**, 381

[36] N. Ould Moussa, E. Trzop, S. Mouri, S. Zein, G. Molnár, A. B. Gaspar, E. Collet, M. Buron-Le Cointe, J. A. Real, S. Borshch, K. Tanaka, H. Cailleau and A. Bousseksou, *Phys. Rev B*, 2007, **75**, 054101

[37] K. Nakano, S. Kawata, K. Yoneda, A. Fuyuhiro, T. Yagi, S. Nasu, S. Morimoto and S. Kaizaki, *Chem. Commun.*, 2004, 2892

[38] B. A Katz and C. E. Strouse, *J. Am. Chem. Soc.*, 1979 **101**, 21

[39] D. Chernyshov, M. Hostettler, K. W. Törnroos, and H.-B. Bürgi, *Angew. Chem. Int. Ed.*, 2003, **42**, 3825 and references therein

[40] J. Kusz, P. Gütlich and H. Spiering, *Top. Curr. Chem.*, 2004, 234:129-153

[41] S. Bonnet, M. A. Siegler, J. Sánchez Costa, G. Molnár, A. Bousseksou, A. L. Spek, P. Gameza and J. Reedijk, *Chem. Commun.*, 2008, 5619

[42] S. Speziale, A. Milner, V. E. Lee, S. M. Clark, M. P. Pasternak, and R. Jeanloz, *PNAS*, 2005, **102**, 50, 17918

[43] C. McCammon, I. Kantor, O. Narygina, J. Rouquette, U. Ponkratz, I. Sergueev, M. Mezouar, V. Prakapenka and L. Dubrovinsky, *Nature Geoscience*, 2008, **1**, 684

[44] J.-F. Lin, H Watson, G. Vankó, E. E. Alp, V. B. Prakapenka, P. Dera, V. V. Struzhkin, A. Kubo, J. Zhao, C. McCammon and W. J. Evans, *Nature Geoscience*, 2008, **1**, 688

[45] P. Gütlich, V. Ksenofontov and A. B. Gaspar, *Coord. Chem. Rev.*, 2005, **249**, 1811

[46] V. Ksenofontov, A. B. Gaspar, P. Gütlich, *Top. Cur. Chem.* 2004 **235**, 23

[47] A. H. Ewald, R. L. Martin, E. Sinn, and A. H. White, *Inorg. Chem.*, 1969, **8**, 9, 1837

[48] A. Bousseksou, G. Molnár and G. Matouzenko, *Eur. J. Inorg. Chem.*, 2004, 4353

[49] V. Ksenofontov, G. Levchenko, H. Spiering, P. Gütlich, J.-F. Létard, Yacine Bouhedja and O. Kahn, *Chem. Phys. Lett.*, 1998, **294**, 545

[50] S. Bonnet, G. Molnár, J. Sánchez Costa, M. A. Siegler, A. L. Spek, A. Bousseksou, W.-T. Fu, P. Gamez, and Jan Reedijk, *Chem. Mater.*, 2009, **21**, 1123

[51] S. Decurtins, P. Gütlich, C. P. Köhler, H. Spiering and A Hauser, *Chem. Phys. Lett.*, 1984, **105**, 1,

[52] A. Hauser, P. Gütlich and H. A. Goodwin, *Top. Curr. Chem.*, 2004, **234**, 155

[53] S. Decurtins. P. Gütlich, K. M. Hasselbach, A. Hauser, and H. Spiering, *Inorg. Chem.*, 1985, **24**, 2174

[54] A. Hauser, *J. Chem. Phys.*, 1991, **94**, 4, 2741

[55] A. Hauser, *Coord. Chem. Rev.*, 1991, **111**, 275

[56] M. Kondo and K. Yoshizawa, *Chem. Phys. Lett.*, 2003, **372**, 519

[57] M. Marchive, P. Guionneau, J. A. K. Howard, G. Chastanet, J.-F. Létard, A. E. Goeta and D. Chasseau, *J. Am. Chem. Soc.*, 2002, **124**, 2, 194

[58] S. Hayami, Z.-Z. Gu, Y Einaga, Y. Kobayashi, Y. Ishikawa, Y. Yamada, A. Fujishima and O. Sato, *Inorg. Chem.*, 2001, **40**, 3240

[59] P. Guionneau, F. Le Gac, A. Kaiba, J. Sánchez Costa, D. Chasseau and J.-F. Létard, *Chem. Commun.*, 2007, 3723

[60] J.-F. Létard, P. Guionneau, O. Nguyen, J. Sánchez Costa, S. Marcén, G. Chastanet, M. Marchivie and Laurence Goux-Capes, *Chem. Eur. J.*, 2005, **11**, 4582

[61] H. Liu, A. Fijishima and O. Sato, *Appl. Phys. Lett.*, 2005, **86**, 122511

[62] E. Freysz, S. Montant, S. Létard and J.-F. Létard, *Chem. Phys. Lett.*, 2004, **394**, 318

[63] S. Bonhommeau, G. Molnár, A. Galet, A. Zwick, J.-A. Real, J. J. McGarvey and A.Bousseksou, *Angew. Chem. Int. Ed.*, 2005, **44**, 4069

[64] S. Bonhommeau, G. Molnár, S. Cobo, D. Ostrovskii and A. Bousseksou, *Polyhedron*, 2009, **28**, 1610

[65] S. Cobo, D. Ostrovskii, S. Bonhommeau, L. Vendier, G. Molnár, L. Salmon, K. Tanaka, and A. Bousseksou, *J. Am. Chem. Soc.*, 2008, **130**, 9019

[66] P. Guionneau, M. Marchive, G. Bravic, J.-F. Létard and D. Chasseau, *J. Mat. Chem.*, 2002, **12**, 2546

[67] J. K. McCusker, A. L. Rheingold and D. N. Hendrickson, *Inorg. Chem.*, 1996, **35**, 2100

[68] M. Marchive, P. Guionneau, J.-F. Létard and D. Chasseau, *Acta. Cryst.*, 2003, **B59**, 479

[69] F. M. Raymo, *Adv. Mater.*, 2002, **14**, 6, 401

[70] J.-F. Létard, P. Guionneau, L. Goux-Capes, *Top. Curr. Chem.*, 2004 **235**:221-249

[71] A. B. Gaspar, M. C. Muñoz and J. A. Real, *J. Mater. Chem.*, 2006, **16**, 2522

[72] A. Galet, A. B. Gaspar, M. C. Muñoz, G. V. Bukin, G. Levchenko, and J. A. Real, *Adv. Mater.*, 2005, **17**, 2949

[73] A. Bousseksou, G. Molnár, P. Demont and J. Menegotto, *J. Mater. Chem.*, 2003, **13**, 2069

[74] L. Salmon, G. Molnár, S. Cobo, P. Oulié, M. Etienne, T. Mahfoud, P. Demont, A. Eguchi, H. Watanabe, K. Tanakae and A. Bousseksou, *New J. Chem.*, 2009, **33**, 1283

[75] O. Kahn and C. Jay Martinez, *Science*, 1998, **279**, 44

2 Experimental Theory and Practice

X-ray diffraction techniques have been in used for the identification of crystal structure for over 70 years. The principles behind all aspects of standard experiments – from data collection to structure solution and refinement – have been previously considered in detail.[1] Consequently this chapter will only discuss the more unusual techniques within crystallography and the experimental procedures that were employed to carry out the work presented herein.

2.1 Low Temperature Single Crystal X-ray Diffraction

Single crystal X-ray diffraction experiments were carried out on a Bruker SMART 1K 3-circle diffractometer unless otherwise stated. In general, the temperature of the sample was controlled using an Oxford Cryosystems Cryostream cooling device[2] for diffraction experiments between 100 K and 500 K or an Oxford Cryosystems HeliX[3] for datasets below 100 K. Both of these devices employ an open-flow gas stream, the gas being nitrogen in the case of the Cryostream and helium in the case of the HeliX.

In the Cryostream, liquid nitrogen is pumped from a Dewar vessel into the 'coldhead' and then passes through a heater, evaporating the liquid into the gas phase. The gas is then pumped through the heat exchanger and temperature controller to the inlet of a diaphragm pump. It is then passed through a line dryer to ensure there is no moisture in the gas which can cause icing around the crystal. The stream is then diverted back to the coldhead, along another length of the heat exchanger to cool the gas again; the temperature of the gas is regulated by a heater and sensor before passing out of the nozzle and over the sample.

In the HeliX, helium gas is cooled through heat exchangers mounted on a two-stage closed cycle refrigerator. The HeliX has a beryllium end nozzle which fits around the crystal, much closer than for the Cryostream. This is necessary to achieve a laminar flow of helium gas, which is much less dense than nitrogen and hence to ensure that the crystal is cooled to the required temperature. When collecting data using the HeliX, the crystal to detector distance was increased from 4.5 cm (whch is the standard distance when using the Cryostream) to 5.5 cm to avoid a collision between the detector and the head of the HeliX.

2.2 In-situ Laser Irradiation

All laser irradiation experiments were performed in-situ on the diffractometer while the crystal was cooled using the HeliX. The laser sits in a clamp which is fixed to the detector arm. A series of adjustable mirrors and prisms direct the laser beam onto the crystal. The laser beam remains focussed on the crystal when any on the three circles are moved, enabling laser irradiation during data collection if required. In general laser irradiation experiments were performed at 30 K. In order to irradiate the crystal uniformly, it was rotated (around φ) during irradiation; the laser was subsequently turned off prior to data collection. Figure 2.1 shows the SMART 1K diffractometer, Cryostream, Helix and laser mount setup.

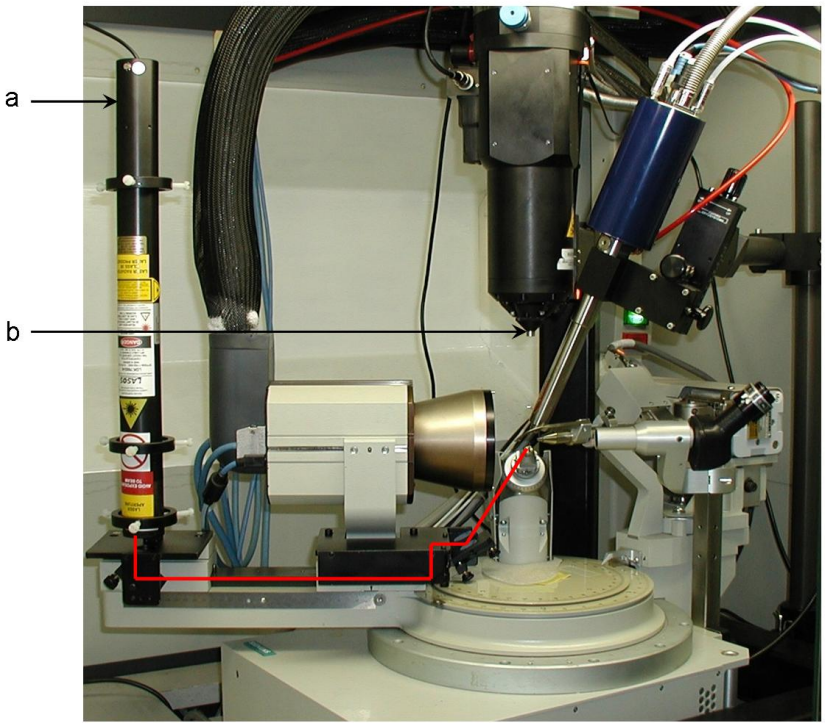

Figure 2.1. Laser (a) mounted on the Bruker 1K diffractometer. The red line indicates the path of the laser beam. During irradiation the Helix head is lowered and the beryllium nozzle (b) sits around the crystal

2.3 High Pressure Diffraction Experiments

Pressure is a thermodynamic parameter, and its effect on a wide variety of materials is of great interest to solid state scientists. A series of developments starting in the 1950s led to a device known as the diamond anvil cell (DAC), which has resulted in

experiments utilising high pressure becoming relatively widespread. While X-ray diffraction was amongst the first techniques to utilise the capabilities of the DAC, many analytical techniques have since been applied to investigate the effect of pressure on a wide range of materials using this method.[4] This section focuses on the equipment and methodology used for single crystal X-ray diffraction experiments using the DAC.

2.3.1 The Diamond Anvil Cell

The diamond anvil cell used in the majority of modern high pressure experiments consists of two opposing diamonds separated by a metal gasket, as shown in Figure 2.2. A sample is held within a hole in the gasket and with the use of a pressure transmitting fluid, a near hydrostatic environment can be achieved. Pressures up to 300 GPa have been attained using a DAC, although single crystal experiments tend to operate at a significantly lower pressure. The pressure is attained by applying a relatively small load onto the large back faces of the diamonds; the culets (front faces) of the diamonds are much smaller in area and hence the pressure obtained can be very large.

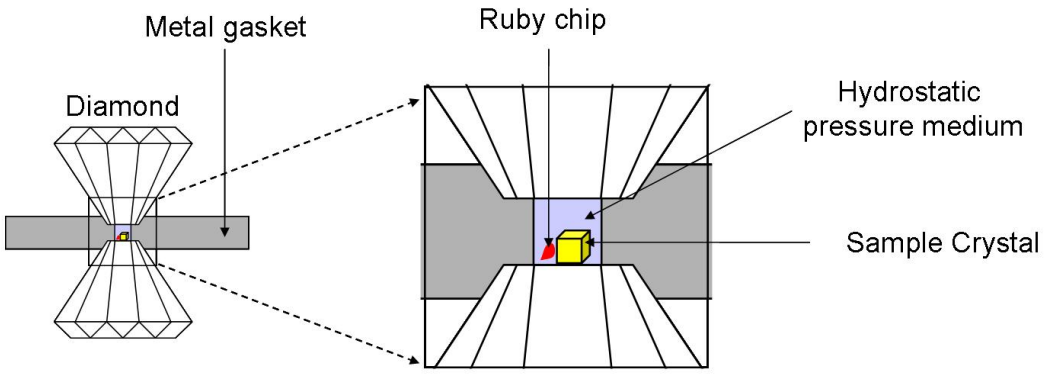

Figure 2.2. Schematic of a diamond anvil cell

There have been many designs of diamond anvil cells used in high pressure scientific experiments, but the most common types used for X-ray diffraction experiments in recent years are the transmission-geometry DACs.[5] These are cells in which both the primary and diffracted beams both pass through the diamonds which encase the sample. In general the diamonds are supported by a backing seat which is set into a steel body support. The support needs to be sufficiently strong to prevent mechanical

failure of the cell and damage to the diamonds at the high pressures associated with these techniques.

The anvils traditionally used in DACs tend to be drukker or brilliant cut diamonds set in beryllium backing seats,[5] as shown in Figure 2.3a. Beryllium is a low Z metal and consequently is a relatively weak absorber of X-rays, compared to heavier metals. Therefore the full opening angle of the steel cell body is accessible during the diffraction experiment when using the beryllium backing seats. However, when the orientation of the DAC is such that the x-axis of the cell is not collinear with the primary beam, the beam passes through the beryllium backing seat, causing diffraction from the beryllium, which can be problematic when data collection is performed using a CCD area detector.

When using a point detector, the diffracted beam can be collimated and so background diffraction from the DAC can simply be left unmeasured. This collimation is much more difficult when using an area detector, where large regions of data are recorded simultaneously. Thus a diffraction pattern measured using this kind of device includes that which comes from the DAC itself rather than the sample. In addition to diffraction from the beryllium, strong reflections from the diamonds are also observed. In an effort to reduce the background diffraction from the DAC, the anvils and backing seats of some diamond anvil cells can be modified to incorporate Boehler-Almax diamonds and a tungsten carbide backing seat,[5] as shown in Figure 2.3b. This design provides sufficient support for the diamonds, while maintaining the opening angle of the DAC and significantly reducing the background diffraction from the cell.

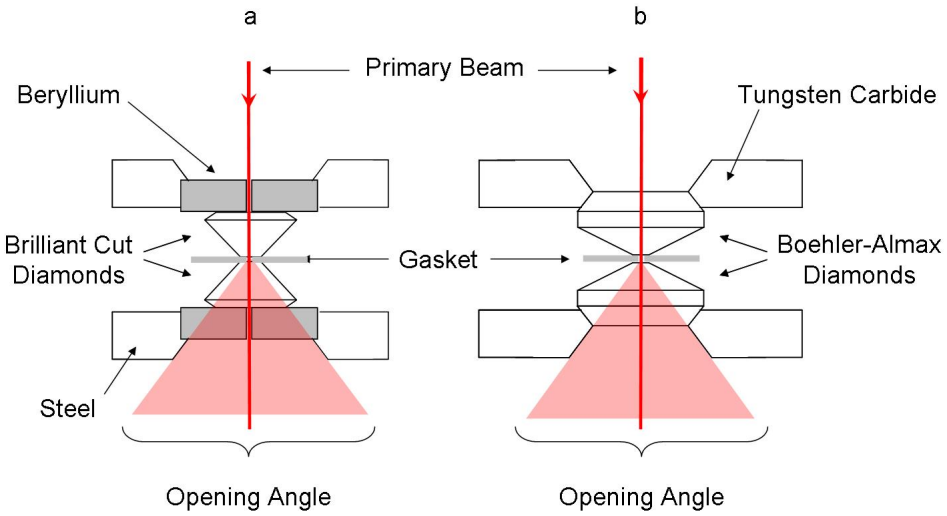

Figure 2.3. Illustration (not to scale) of the anvil and backing seat design for a. beryllium backed and b. tungsten carbide backed diamonds. In this orientation of the cell the path of the primary beam coincides with the x-axis of the cell

The diamond anvil cell used for high pressure data collections in this study was the Diacell Bragg-LT(S), which is shown in Figure 2.4. It has anvils with 0.8 mm culets, supported by beryllium backing seats and can achieve pressures up to 95 GPa.[6] The upper diamond is mounted into a piston (Figure 2.4e) that fits into the cylinder (Figure 2.4d), in which the lower diamond is mounted. The gasket (Figure 2.4b) is placed into the gasket holder on top of the lower diamond. Insertion and removal of the piston is achieved using the insertion tool (Figure 2.4f). After insertion of the piston into the cylinder the insertion tool is removed and the face plate (Figure 2.4c) is placed on top and pressure is applied by tightening two allen screws (Figure 2.4a), each with opposing threads, to avoid torque.

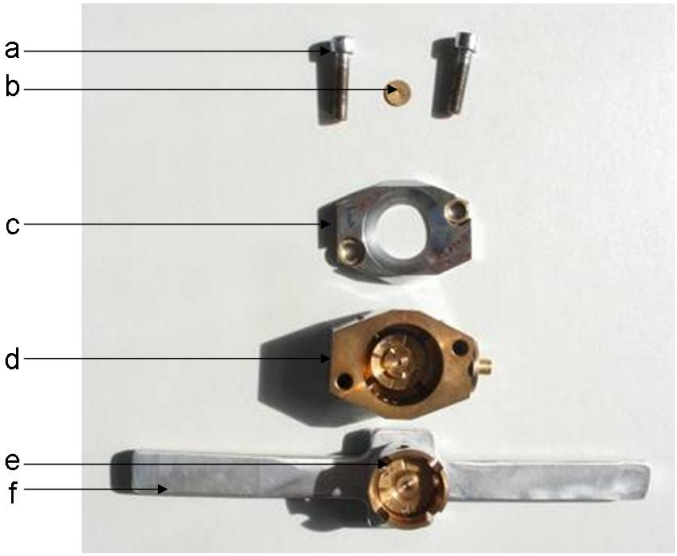

Figure 2.4. The Diacell Bragg-LT(S) diamond anvil cell. See text for definition of component parts

While the choice of backing plates is important in reducing background scattering from the DAC, other methods have also been attempted to achieve this.[7] As mentioned previously, collimation of the diffracted beam such that X-rays diffracted only by the sample crystal have access to the detector is one way of omitting background scattering. This, however, is not straightforward when using image plate or CCD detectors. Another method is to reduce the divergence of the primary beam, reducing the area of the DAC with which the primary beam comes into contact and hence reducing the background scatter. This can be achieved at synchrotron sources, where using very narrow, focussed beams is common practice, or by very narrow collimation of the primary beam in the home laboratory. The latter method will result in low intensity of the primary beam and so it has been suggested that the size of the beam passing through the DAC can be controlled by using a highly absorbing gasket material such as tungsten or rhenium.[7]

2.3.2 Gasket Preparation

The gaskets used during data collection were made of either tungsten or a beryllium copper alloy. While tungsten serves to reduce background scatter from the DAC it is also very hard and brittle. Specialist equipment is required to cut and drill sheets of tungsten to make it suitable for use as a gasket. The tungsten gaskets used were cut

and drilled by Dr. S. Moggach at the University of Edinburgh. Additional high pressure experiments were carried out using gaskets made of a beryllium copper alloy. Although this choice of material results in higher background scattering, it is much softer and can be drilled in house.

The gaskets were pre-indented to a thickness of between 150 μm and 80 μm and a hole was subsequently drilled in the centre of the indentation. The hole was drilled using an electro-erosion device for the tungsten gaskets and a hand-held micro drill for the beryllium copper gaskets.

2.3.3 Sample Loading

A crystal of suitable quality was selected and cut to the appropriate dimensions to fit within the confines of the gasket hole. The crystal was then fixed to the culet of the top diamond using inert perflouropolyether oil, along with a small ruby chip. The gasket was fitted on top of the lower diamond and the drilled hole was filled with paraffin oil, which was to act as the pressure transmitting medium. The top diamond was then placed on top of the lower diamond and gasket, ensuring the sample crystal aligned with the hole in the gasket, and the cell closed. Pressure was applied to the cell using the allen screws.

2.3.4 Centring

Due to the restrictions of the diamond anvil cell body (the sample is only visible along the x-axis of the DAC, through the gasket holes) it is not possible to centre the sample in the conventional manner used for standard data collections. Procedures for centring the DAC have been published previously[7] and include optical sample centring and centring by diffraction. The former method requires a microscope with variable focal length attached to the diffractometer, while the latter method is not trivial to perform on a 3-circle diffractometer. A method called gasket-shadow centring has also been suggested and allows for an increase in the precision of centring from ~ 0.1 mm using the optical method to ~ 0.02 mm.[8]

Gasket-shadow centring of the sample crystal relies on the diameter of the primary X-ray beam being larger than the gasket hole and assumes that the sample to be investigated is in the centre of that hole. During centring using this method the flux of the primary beam is significantly reduced and the beamstop is removed. An image of

the primary beam after passing through the DAC is acquired using a CCD area detector. The shape and position of the spot on the detector from the primary beam depends on the position of the DAC. A definition of the diamond anvil cell axes used in the following discussion is given in Figure 2.5.

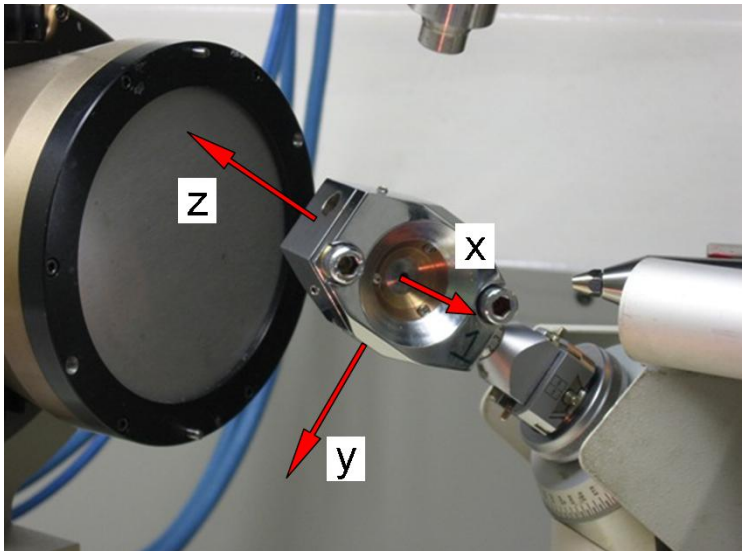

Figure 2.5. Definition of the laboratory axes with respect to the DAC. The z – axis of the DAC is collinear with the φ – axis of the diffractometer when mounted on a three-circle (fixed χ) goniometer. When the ω – circle is in the zero position the x – axis of the DAC is parallel to the primary X-ray beam

When centring in the yz plane, two primary beam images are obtained from two positions of the DAC, related by a 180° rotation of the cell about the x-axis. This rotation would be achieved in practice by a 180° rotation of the χ-circle on a 4-circle diffractometer. The position of the beam exiting the cell can be compared by subtracting one image from another. If the cell is centred in the yz plane the two images will overlap perfectly; if this is not the case, the cell position can be altered and the procedure repeated until overlap is achieved. Illustrations of typical images obtained using this procedure are shown in Figure 2.6.

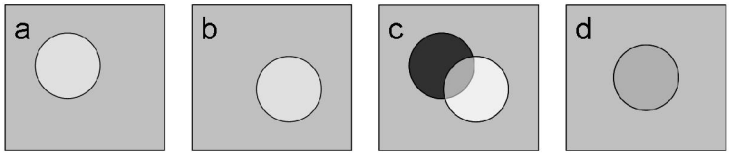

Figure 2.6. Illustration of the procedure for centring in the yz plane using the gasket-shadow centring method.[8] a and b show primary beam images obtained from the DAC in two different positions, related by a 180° rotation about the x-direction. c shows the image obtained on subtraction of a from b and reveals the cell to be off-centre in the yz plane. d shows the image obtained when the cell is centred in the yz plane. White indicates areas where intensity is positive, black indicates areas of negative intensity and grey indicates areas of zero intensity

Once centring in the yz plane has been achieved, centring along the x direction is conducted also by comparing images of the primary beam with the diamond anvil cell at two different positions. The relationship between the images in this case should be a rotation of a few degrees away from the position perpendicular to the primary beam in positive and negative directions. Figure 2.7 illustrates the procedure used for centring the DAC along the x-direction.

Data collections using the DAC in this study were performed on a three circle diffractometer with a fixed χ-angle, which does not have a microscope that allows fine translation along the viewing direction. Consequently a combination of the optical centring (for the yz plane) and gasket-shadow centring (for the x-direction) was chosen for sample centring.

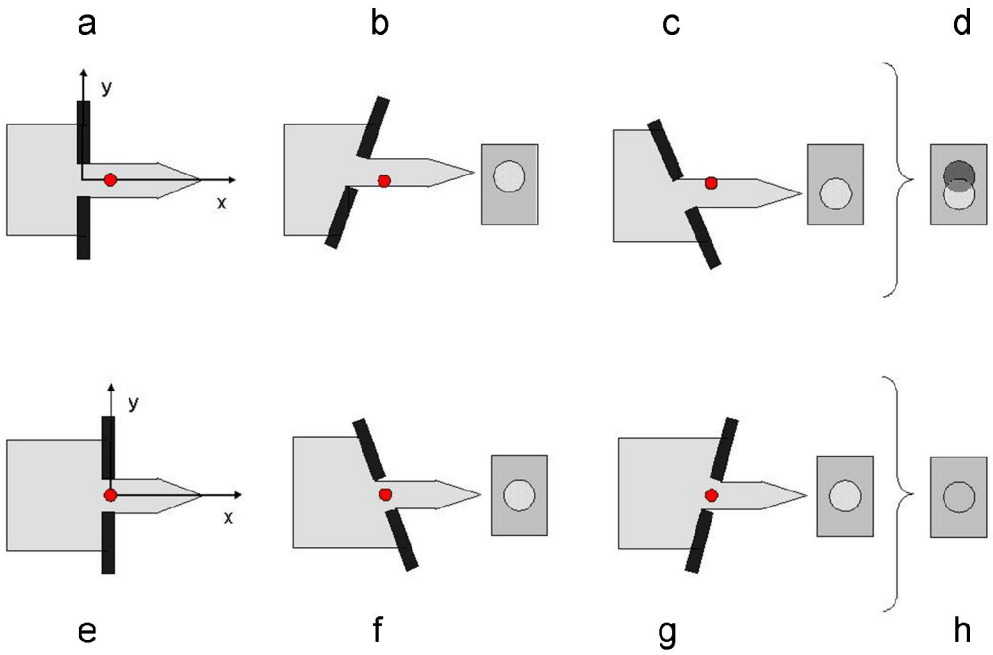

Figure 2.7. Illustration of the procedure for centring in the x-direction using the gasket-shadow centring method.[4] The gasket is shown in black, the primary beam in light grey and the centre of the diffractometer is shown as a red circle. a shows the position of the gasket in a DAC that is not centred in the x-direction. b and c show the position of the gasket when rotated +20° and -20° in ω and the effect this has on the position of the beam exiting the DAC and the image obtained on the detector. d shows the image obtained when the image shown in b is subtracted from that in c. e, f, g and h are equivalent to a, b, c and d respectively for a DAC that is centred in the x-direction

The DAC is mounted on the diffractometer using a Huber goniometer head with a modified sample mounting collar. The DAC is then oriented such that the x-axis of the goniometer head[9] is parallel to the x-axis of the diamond anvil cell and the y-axis is perpendicular to the plane of view. The sample was optically centred in the y- and z-directions. Crude centring in the x-direction was achieved by adjusting the position of the DAC along x until the sample was in focus. The DAC was rotated by 180° around the z-axis (equivalent to a 180° rotation of the φ-circle) and the sample brought back into focus by adjustment in the x-direction. A final adjustment was performed such that the final position of the DAC was half way between the two focussed positions. Fine centring in the x-direction was subsequently performed using the gasket shadowing method described above.

2.3.5 Data Collection

X-ray diffraction data collection was performed on a 3-circle fixed χ diffractometer equipped with a SMART 1K CCD area detector. A shortened collimator was used so as to accommodate the large body of the DAC. The beam stop was also removed for the same reason and data collection was performed at values of 2θ so as to ensure the detector was never coincident with the direct beam. The sample – detector distance was 7 cm. A series of 8 ω-scans were performed at different positions in φ at two settings of 2θ, using the Bruker SMART software.[10]

2.3.6 Indexing and Integration

Unlike in standard single crystal data collections, indexing data obtained using a DAC is often performed after the full dataset is collected. First a thresholding procedure was performed using the Bruker SMART software[10] to harvest reflections from the raw frame data. These reflections are then viewed and sorted using the reciprocal lattice viewer RLATT,[11] as shown in Figure 2.8. Sample reflections were indexed with the SMART software.[10]

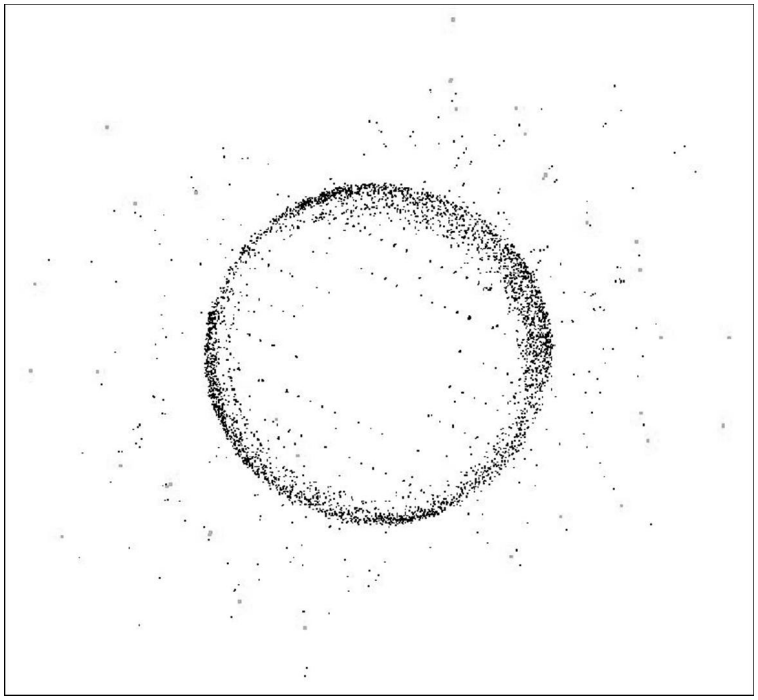

Figure 2.8. Diffraction pattern from a sample in a DAC viewed in the reciprocal lattice viewer RLATT. Sample reflections are identified as forming clear reciprocal lattice lines

2.3.7 Masking Procedure

During the integration process, the images collected from the CCD during the diffraction experiment are transformed into a list of diffracted intensities. As stated previously, there is a lot of background diffraction observed when using a DAC to collect X-ray data, originating from the beryllium backing seats and the diamonds themselves. In regions where this diffraction is strong integrated intensities will be significantly higher than those expected from the sample alone. There are also areas of the detector which will be shadowed by the steel body of the cell, where the diffracted beams cannot reach the detector. In these areas the integrated intensity will be much lower than expected for the sample crystal. Regions that are shaded by the cell body and areas of relatively intense background diffraction should be masked out during integration, effectively ensuring that integration is not carried out in these regions of reciprocal space.

The beryllium powder rings and regions of shadowing from the DAC body may be masked out using ECLIPSE, a program written by Simon Parsons at Edinburgh University.

It has previously been shown that the quality of data collected using a DAC can be significantly improved by masking the diamond reflections which are coincident with the position of expected reflections,[12] in addition to the powder-like regions caused by the beryllium backing plates. It was found during the course of this study that the data collected using this detector could be further improved by masking out not only those diamond reflections that are expected to overlap with sample reflections, but also those which are particularly strong on any frame.

Create_Mask is a program written by Dr. M. R. Probert in the Dept. of Chemistry, Durham University, which allows for the generation of mask files which exclude from the integration any area of the frame image specified by the operator. Another program, Merge_Mask, subsequently merges these mask files with those generated by ECLIPSE to produce a final mask file which is then used for integration. The masking procedure is summarised in Figure 2.9.

Once the orientation matrix of the sample crystal was determined and mask files were written for the whole dataset, the raw data were integrated using the Bruker SAINT program.[13]

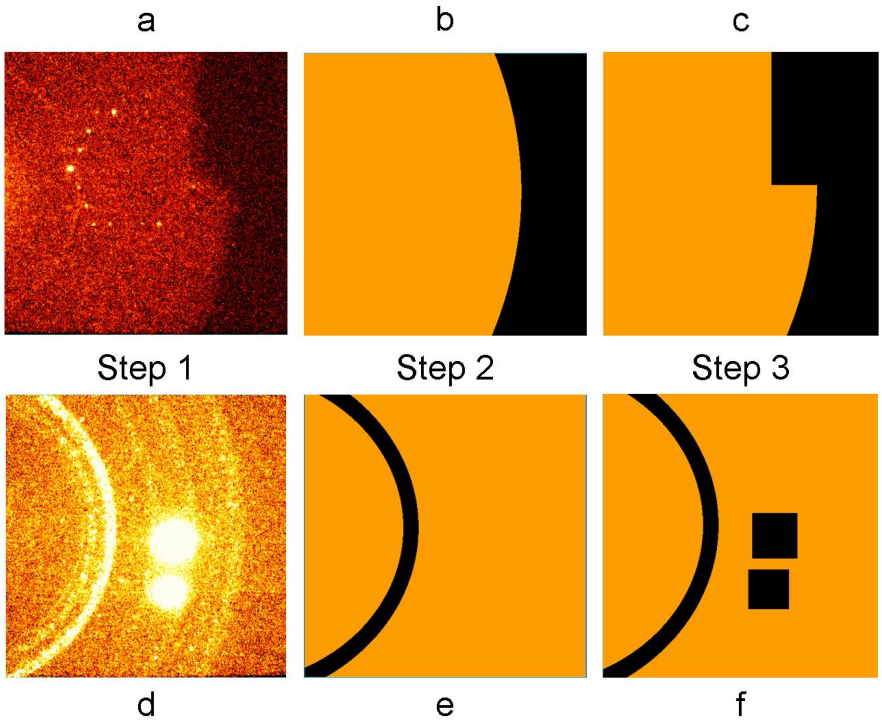

Figure 2.9. Demonstration of the masking procedure used for data collected using the DAC. Step 1 – Identify areas on the detector shadowed by the DAC body (image a), beryllium powder rings and strong diamond reflections (d). Step 2 – Generate files using ECLIPSE, masking the beryllium contribution (e) and the shadowing from the cell body (b). Step 3 – generate a final mask file removing areas of the detector shadowed by bolts (c) and reflections from diamonds (f)

2.3.8 Pressure Determination

The R_1 ruby fluorescence signal varies linearly with applied pressure and is well calibrated up to pressures well in excess of those attained the studies presented herein.[4] The relationship between pressure and the shift of this line[14] is given by Equation 2.1.

$$P = 1.328\ \Delta\bar{\nu}$$

$\Delta\bar{\nu}$ = shift in wavenumbers
P = pressure in kbar

Equation 2.1. Relationship between the shift of the R1 ruby fluorescence line in wavenumbers and pressure in kbar

The shift of the R_1 ruby fluorescence line was measured by Mr. Lucas Applegarth in the Dept. of Chemistry, Durham University. The signal was measured for a sample under ambient conditions as well as for the ruby chip inside the pressure cell. Figure 2.10 shows an example of the fluorescence response of the ruby chips under ambient conditions and at elevated pressure. The difference in wavenumber of the maxima was 5.35 cm^{-1} in this case, which corresponds to a pressure of 7.1 kbar.

The laser used during the fluorescence experiment has the capacity to induce a spin transition in a SCO sample in an analogous manner to that observed during the LIESST effect.[15] However, Raman experiments are rarely performed at temperatures below T_{LIESST} and hence the meta-stable high spin state does not become "trapped" as in the case of LIESST. In an effort to ensure any structural changes observed were the result of pressure and not light irradiation it was decided that for all SCO complexes the pressure should be measured after the diffraction experiment had taken place.

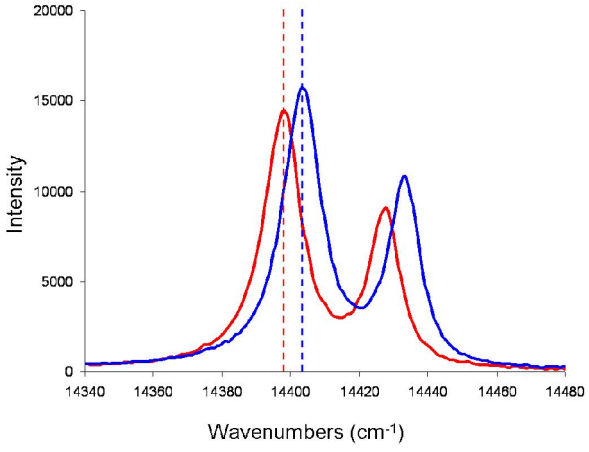

Figure 2.10. Fluorescence signal of ruby chip under ambient conditions (blue) and under pressure (red). Dashed lines indicate the position of maxima used for calculating the pressure within the cell

2.3.9 Structure Solution and Refinement

The proportion of observable unique data in a high pressure single crystal X-ray diffraction experiment is often exceptionally low. This is a product both of the limited access to reciprocal space caused by the restrictions of the sample environment and the crystal system of the sample. None of the samples investigated at high pressure during this study was of higher symmetry than monoclinic and consequently structure solution and refinement were affected by the low amount of data available. In general the ambient phase structure was used as a starting point for refinement against the high pressure data so as to avoid structure solution.

A number of measures were taken to increase the data:parameter ratio during structure refinement. Additional data in the form of chemical information were used in the form of least-squares restraints. These restraints were used for aromatic ring systems, ensuring planarity and applying predetermined bond distances.

The inherently non-spherical resolution of data collected using a DAC may result in poorly defined anisotropic temperature factors (U_{aniso}). Unless a high degree of thermal libration is apparent in the structure, atomic displacement parameters (ADPs) are expected to be approximately isotropic for data of good quality and spherical resolution.[16] Consequently during refinement of structures obtained from the DAC in this study, the temperature factors were either modelled using an isotropic representation of the temperature factor (U_{iso}), or using a restrained anisotropic model. Refinement of U_{iso} rather than U_{aniso} also serves to reduce the ratio of data to parameters. U_{iso} requires the refinement of one parameter per atom in addition to the three fractional coordinates that define its position in the unit cell. Refinement of U_{aniso} requires six parameters defining the shape and orientation of an ellipsoid to be refined during the least-squares process, in addition to the three parameters defining the coordinates of the atom.

2.4 Twinning

Twinning is the term which describes the collation of more than one crystal domain within one 'crystal', leading to complications with structure solution and/or refinement. The relative orientation of different components of the twinned crystal can be related to one another through a geometrical relationship, known as the twin law.

This relationship may involve a rotation, reflection or inversion of one unit cell domain relative to that of another. The fraction of the structure in each orientation is called the twin scale factor. The diffraction pattern recorded from a twinned crystal will include reflections from all domains present. Reflections may be coincident with those from another domain, surreptitiously increasing the intensity of these reflections.

2.4.1 Twinning by Merohedry

When a symmetry operation of the lattice is not present in the point group of the crystal structure it may act as a twin law, relating two domains within that crystal. For example the point group of the crystal lattice (also called holohedral point group) for hexagonal systems is 6/mmm. The point group 6/m is a subgroup (also called merohedral point group) of the holohedral point group 6/mmm. A 2-fold rotation about the [110] direction is a symmetry operation which occurs in 6/mmm but not 6/m. Hence a crystal with the point group 6/m twinned by a 2-fold rotation about [110] would be said to be twinned by merohedry.

2.4.2 Twinning by Inversion

Since all lattices (and hence holohedral point groups) have inversion symmetry, all non-centrosymmetric space groups may be twinned by inversion. This is a relatively common cause of twinning. The crystal of a compound in such a space group may contain domains of each enantiomer, in which case the twin law is just the inversion operator. Inversion twinning may be considered as a special case of merohedral twinning. The scale factor between domains of an inversion twin is known as the Flack parameter and should be checked whenever a non-centrosymmetric space group is encountered, unless the sample is known to be enantiomerically pure.

2.4.3 Twinning by *Pseudo*-Merohedry

Twinning may occur when the unit cell has a higher metric symmetry than is *actually* present, for example a monoclinic cell which has a β angle close to 90°, making it resemble an orthorhombic system. A 180° rotation about the a or c axes may then lead to a situation in which the unit cells can fit together in different orientations without compromising the packing. It has been noted that this form of twinning will only occur when the intermolecular interactions across the domain boundary are similar in both orientations.[17]

Twinning often results when a high symmetry crystal looses symmetry on going through a phase transition as a result of an external influence such as a change in temperature or pressure. In this case the symmetry element that has "disappeared" may act as the twin law in the lower symmetry case.

Twinning by *pseudo*-merohedry is distinct from twinning by merohedry in that the symmetry operation that corresponds to the twin law does not belong to a higher symmetry holohedral point group of the same crystal system. That the lower symmetry system possesses appropriate metric symmetry for this type of twinning is purely coincidental.

When a crystal is twinned by merohedry or *pseudo*-merohedry, reflections from one domain overlap with those of the other and all reflections are affected. In this case the presence of twinning may not be detected until a full dataset has been collected.

In all cases during this investigation twinning by *pseudo*-merohedry resulted from the lowering of symmetry during a phase transition. Hence derivation of the twin law was relatively straight forward by comparison of the symmetry elements present in the higher symmetry phase(s) with those in the lower symmetry phase. Once the twin law is known it can be input into SHELXL[18] in matrix form to enable refinement of the structure and the twin scale factor.

2.4.4 Non-Merohedral Twinning

Reflections from crystals twinned by non-merohedry do not necessarily contain a contribution from each twin domain. This could occur when a supercell of higher symmetry can be formed from the true unit cell, for example a tetragonal unit cell where $2c \approx a$ can form a cubic supercell. In this case any symmetry operation belonging to the cubic group could act as a potential twin law. Only certain zones of reflections would be affected by overlap, resulting in many more reflections in the diffraction pattern than if twinning was not present. Indexing can prove difficult in this case.

Once indexing has been achieved and the data has been integrated two different reflection files can be created. The first is one in which either the equivalent reflections from each component are averaged or those from one component are ignored

completely, while the other lists reflections from each component separately along with an identifier to describe which twin component each reflection originates from. In SHELX these reflection files are known as hkl4 and hkl5 format files respectively. The hkl4 format file is used for structure solution, while the hkl5 file is used for the refinement process.

---

[1] See for example C. Giacovazzo et al. *Fundamentals of Crystallography*, 1992, Oxford University Press

[2] J. Cosier and A. M. Glazer, *J.Appl. Cryst.*, 1986, **19**, 105

[3] A. E. Goeta, L. K. Thompson, C. L. Sheppard, S. S. Tandon, C. W. Lehmann, J. Cosier, C. Webster and J. A. K. Howard, *Acta Cryst.*, 1999, **C55**, 1243

[4] W. A. Bassett, *High Pressure Research*, 2009, **29**, 2, 163

[5] S. A. Moggach, D. R. Allan. S. Parsons and J. E. Warren, *J. Appl. Cryst.*, 2008, **41**, 249 and references therein

[6] Diacell Bragg-LT(S) Technical Manual, DXR-6B, 2005

[7] A. Katrusiak, *High Pressure Crystallography*, NATO Science Series, II. Mathematics, Physics and Chemistry – Vol. 140, Proceedings of the NATO Advanced Research Workshop on High-Pressure Crystallography, Erice, Italy, 2003, pg 57 - 68

[8] A. Budzianowski, A. Katrusiak, *High Pressure Crystallography*, NATO Science Series, II. Mathematics, Physics and Chemistry – Vol. 140, Proceedings of the NATO Advanced Research Workshop on High-Pressure Crystallography, Erice, Italy, 2003, pg 101 - 112

[9] Goniometer head axes as defined in the Apex II User Manual, Version 2, June 2006, Part Number M86-E01078, Bruker Analytical X-ray Instruments Inc.

[10] SMART-NT, Data Collection Software, version 6.1, Bruker Analytical X-ray Instruments Inc., Madison, WI, USA, 2000

[11] RLATT, Reciprocal lattice viewer, version 3.0, Analytical X-ray Instruments Inc., Madison, WI, USA, 2000

[12] N. Casati, P. Macchi and A. Sironi, *J. Appl. Cryst*., 2007, **40**, 628

[13] SAINT-NT, Data Reduction Software, version 6.1, Bruker Analytical X-ray Instruments Inc., Madison, WI, USA, 2000

[14] G. J. Piermarini, S. Block, J. D. Barnett and R. A. Foreman, *J. Appl. Phys*., 1975, **46**, 2774

[15] S. Bonnet, G. Molnár, J. Sánchez Costa, M. A. Siegler, A. L. Spek, A. Bousseksou, W.-T. Fu, P. Gamez, and J. Reedijk, *Chem. Mater*., 2009, **21**, 1123

[16] D. Watkin, Acta Cryst., 1994, **A50**, 411

[17] S. Parsons, *Acta Cryst*., 2003, **D59**, 1995

[18] G. M. Sheldrick, *Acta Cryst*., 2008, **A64**, 112

3 Thermal and Light Induced Spin Transitions in [{Fe(bbp)(NCS)$_2$}$_2$4,4'-bipy]•2MeOH

3.1 Introduction

[{Fe(bbp)(NCS)$_2$}$_2$4,4'-bipy]•2MeOH (bbp = 2,6-Bis(3-pyrazolyl)pyridine, bipy = 4,4'-bipyridine) is a dinuclear Fe^{II} species shown in Figure 3.1. It has been shown by D. Fedaoui *et al.*[1] using SQUID magnetometry to undergo a partial spin transition at ~118 K, equating to 50% of the iron centres becoming low spin (Figure 3.2). The magnetic data also show that it is possible to induce a spin transition at low temperatures using light irradiation. χT during laser irradiation at low temperature demonstrates full population of the meta-stable high spin (HS*) state. T_{LIESST} was determined to be 72 K by plotting the derivative of χT vs. T on warming after laser irradiation.

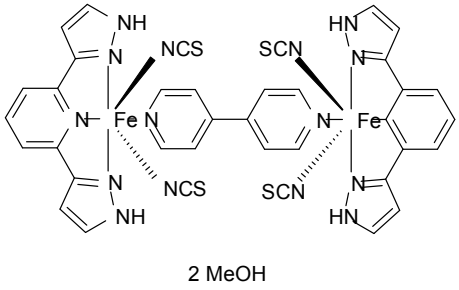

Figure 3.1. [{Fe(bbp)(NCS)$_2$}$_2$4,4'-bipy]•2MeOH, where bbp = 2,6-bis(parazol-3-yl)pyridine

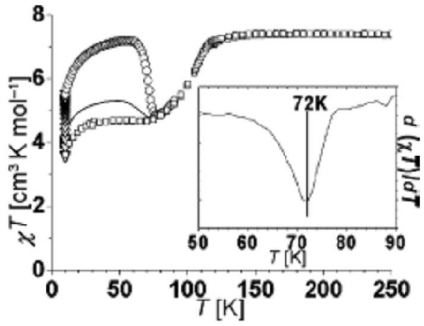

Figure 3.2. Magnetic susceptibility data for [{Fe(bbp)(NCS)$_2$}$_2$4,4'-bipy]•2MeOH.[1*] The abrupt decrease at 118 K is indicative of a partial spin transition, where χT decreases by half. The inset shows the derivative of χT vs. T on warming after laser irradiation

*** Complexation of 2,6-Bis(3-pyrazolyl)pyridine–Bis(thiocyanato)iron(II) with a Bridging 4,4'-Bipyridine: A New Example of a Dinuclear Spin Crossover Complex. Dalila Fedaoui, Yacine Bouhadja, Abdellah Kaiba, Philippe Guionneau, Jean-François Létard, Patrick Rosa.. Eur. J. Inorg. Chem. 2008, 1022–1026. Copyright Wiley-VCH Verlag GmbH & Co. KGaA. Reproduced with permission.**

3.2 Experimental Details

A crystalline sample of the title compound was obtained from Dr. Philippe Guionneau and co-workers at the ICMCB in Bordeaux, France.

A single crystal of [{Fe(bbp)(NCS)$_2$}$_2$4,4'-bipy]•2MeOH was mounted on a glass fibre using epoxy resin glue. This crystal was used for all ambient pressure structure determinations. X-ray data were collected at 290, 140 and 30 K using graphite-monochromated Mo-Kα radiation (λ = 0.71073 Å) on a Bruker SMART-CCD 1 K diffractometer. A series of narrow ω-scans (0.3°) were performed at several φ-settings in such a way as to cover a sphere of data to a maximum resolution of 0.75 Å. Cell parameters were determined and refined using SMART software,[2] and raw frame data were integrated with the SAINT program.[3] The structures were solved by direct methods using SHELXS,[4] and refined by full-matrix least-squares on F^2 using SHELXL-97[4] and the graphical user interface Olex2.[5]

The temperature was controlled using a Cryostream N_2 open flow cooling device[6] (for the datasets at 290 K and 140 K) and an Oxford Cryosystems Helix[7] for the 30 K datasets. Laser irradiation of the single crystal was performed at 30 K for 1 hour using a 5 mW laser (670nm), which was turned off prior to data collection.

The study of the evolution of cell parameters as a function of temperature was performed by continuously collecting 50 frames with a scan width of 1° in ω at 0° and 90° in φ, while ramping in temperature (using the Helix) at such a rate as to ensure each set of 50 frames was collected over no more than 2.5 K. Data were collected between 250 K and 30 K. A unit cell was determined from the first and second sets of 50 frames, the second and third, third and fourth and so on using a program called SMARTreduce written by Dr. M. R. Probert in the Department of Chemistry, Durham University, yielding a data point every 2.5 K. SMARTreduce is a script which runs SMART[2] automatically, harvesting reflections, indexing the cell and refining the parameters using least squares cycles in an iterative manner across the entire temperature range. This automation allows for easier collection of unit cell parameters at much smaller temperature intervals than if the procedure was carried out manually.

The high pressure study was carried out using a different crystal of similar quality and smaller size due to the restrictions of the size of the sample chamber in the diamond

anvil cell (DAC). The general procedure for loading and centring of the DAC, along with the methods for data collection, processing and pressure measurement are given in Chapter 2.3. The pressure transmitting medium used was paraffin oil, chosen because the sample is soluble in many of the common fluids used for this task, such as methanol/ethanol.

3.3 Results

3.3.1 Structure at 290 K – Phase 1

A full structural determination of the title compound was carried out at 290 K, yielding a structure with the asymmetric unit containing half a dinuclear unit (related to the rest of the molecule by an inversion centre located between the central carbon atoms (C14 and C14′) of the bipy unit) and one methanol molecule of solvation (Figure 3.3).

From inspection of the iron-nitrogen bond distances (Table 3.1), it is clear that the iron centre is in the high spin (HS) state, which is in agreement with the magnetic data. The volume of the distorted octahedron surrounding the iron centres is 12.980(7) Å^3; again indicating the system is in the HS state. This structure is entirely in agreement with that previously published in the paper by D. Fedaoui *et al.*,[1] which largely serves to describe the synthesis and magnetic behaviour of the system.

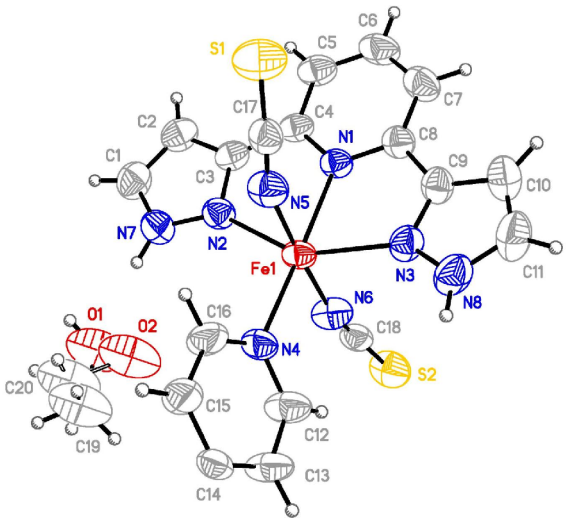

Figure 3.3. Asymmetric unit of [{Fe(bbp)(NCS)$_2$}$_2$4,4′-bipy]•2MeOH at 290 K. Atomic Displacement Parameters (ADPs) are shown at 50% probability

Table 3.1. Fe – N bonding distances in [{Fe(bbp)(NCS)$_2$}$_2$4,4′-bipy]•2MeOH at 290 K

Bond	Distance (Å)
Fe1 – N1	2.143(1)
Fe1 – N2	2.203(2)
Fe1 – N3	2.228(2)
Fe1 – N4	2.164(2)
Fe1 – N5	2.152(2)
Fe1 – N6	2.109(2)

Selected crystallographic data for Phase 1 and that of all others is given in Table 3.8.

3.3.2 Thermal Behaviour

The unit cell parameters were investigated as a function of temperature in order to explore the structural behaviour of [{Fe(bbp)(NCS)$_2$}$_2$4,4′-bipy]•2MeOH between room temperature and 30 K. The results of this study are shown in Figure 3.4. There are two obvious phase transitions, the first at 170 K, leading to a 4-fold increase in cell volume and the second at 118 K, which is the temperature associated with the Spin Transition, as identified using magnetic measurements.

In light of these findings, further datasets were collected at 140 K and 30 K with the aim of examining the structural behaviour and thus determining the effect of the structure upon physical properties.

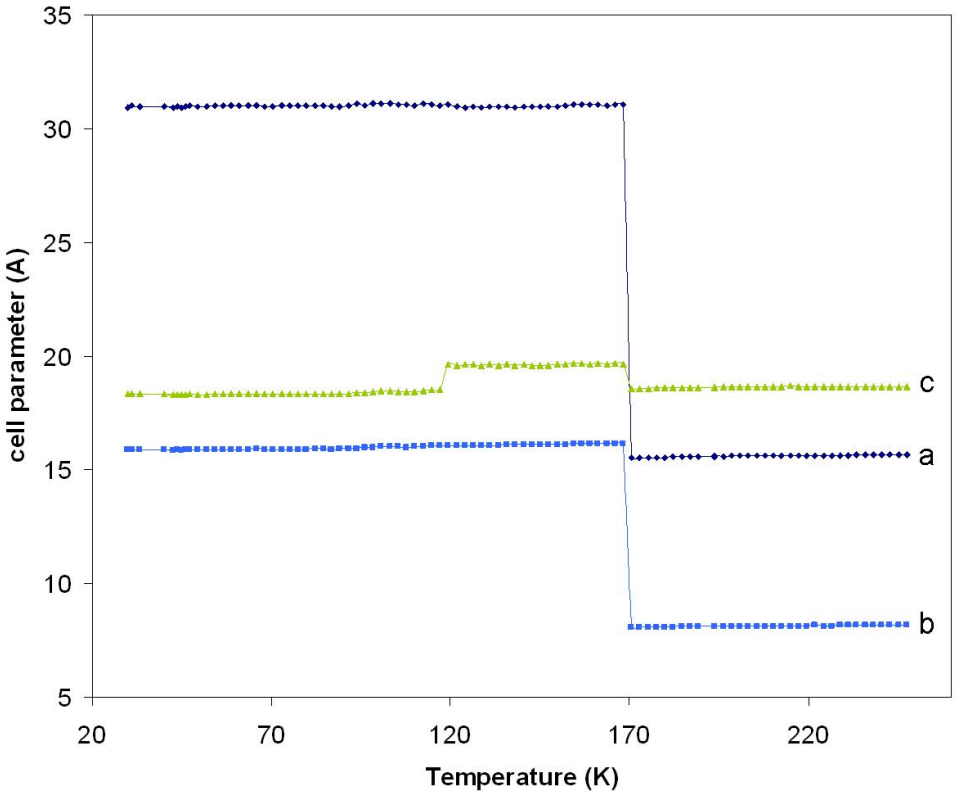

Figure 3.4. Cell parameter evolution as a function of temperature. Errors on all values are contained within data points

3.3.3 Structure at 140 K – Phase 2

A full data collection was carried out at 140 K, to determine the nature of the phase transition that increases the cell volume by a factor of four relative to Phase 1.

The pattern indexed with a C-centered lattice, with the third cell axis being slightly longer than that in the higher temperature structure and a concomitant increase in the unique angle, β. The structure solved and was refined in the space group Cc, with an inversion twin law, and a batch scale factor that refined to ~0.4.

The driving force for this phase transition appears to be a twisting of the bridging bipyridine ligand. This twisting removes the inversion centre that was previously located between the two bipyridine rings, resulting in each iron site in the molecule becoming crystallographically-independent. The number of molecules in the

asymmetric unit (Z′) is now 2 (giving 4 independent iron centres) as shown in Figure 3.5.

The C15 – C14 – C14′ – C13′ torsion angles are 20.4(5)° and -16.1(5)° for molecules A-B and C-D respectively. The opposite directions of this twist result in the two molecules having opposite chirality.

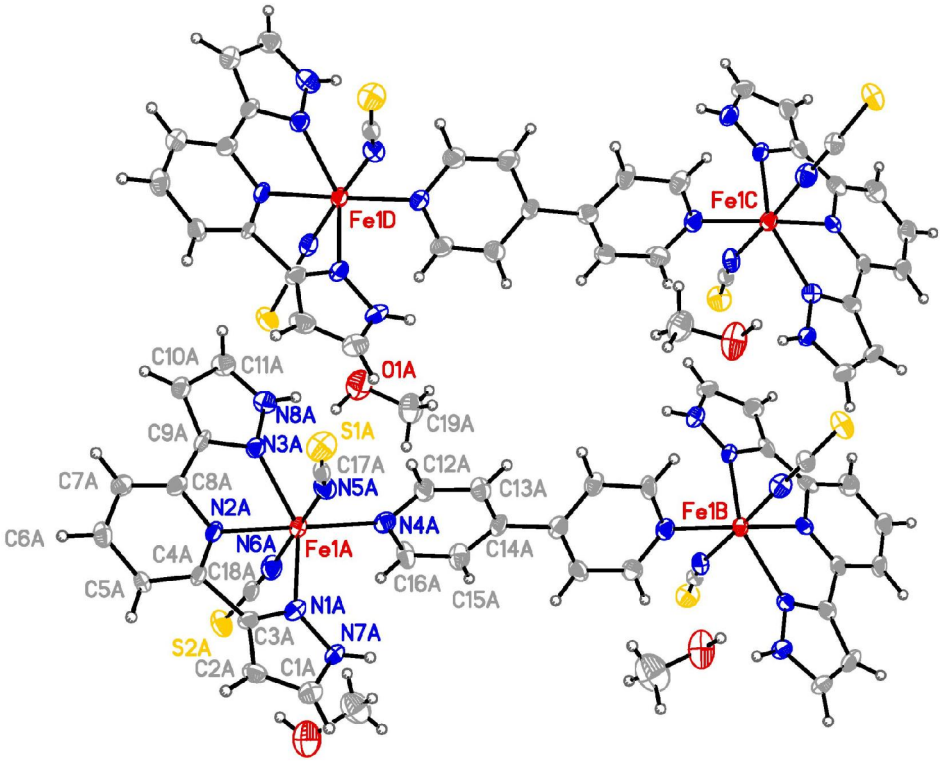

Figure 3.5. Asymmetric unit of [{Fe(bbp)(NCS)$_2$}$_2$4,4′-bipy]•2MeOH at 140 K in the space group Cc. ADPs are drawn at 50% probability. The numbering scheme is shown for the half molecule containing Fe1A but is consistent throughout the structure, replacing the suffix with that of the associated iron atom

As expected from the magnetic data, all four of the crystallographically unique iron atoms are in the high spin state, as evidenced by the volume of the Fe – N_6 coordination octahedron and Fe – N bond distances, shown in Table 3.2 and Table 3.3 respectively.

Table 3.2. Volume of coordination octahedron for the four unique iron atoms

	Octahedral volume (Å^3)
Fe1A	12.97(2)
Fe1B	12.96(2)
Fe1C	12.95(2)
Fe1D	12.75(2)

Table 3.3. Fe – N bond distances (Å) for the compound at 140 K (Phase 2)

	N1	N2	N3	N4	N5	N6
Fe1A	2.215(5)	2.153(4)	2.207(4)	2.160(4)	2.153(5)	2.110(5)
Fe1B	2.230(4)	2.130(4)	2.204(4)	2.176(4)	2.093(5)	2.150(5)
Fe1C	2.200(5)	2.134(4)	2.231(5)	2.184(4)	2.143(5)	2.092(5)
Fe1D	2.210(5)	2.141(4)	2.188(5)	2.117(4)	2.144(5)	2.117(5)

3.3.4 Structure at 30 K – Phase 3

On further cooling to 30 K the system undergoes a partial spin transition equating to half of the Fe centres becoming low spin. The orientation of the unit cell may be considered analogous to that of Phase 1 but with a doubling of the *a* and *b* axes, and C-centering. The lattice is metrically C-centred, but the c-glide has disappeared, resulting in the non-conventional space group Cī (Phase 3*). For simplicity the cell was transformed into the primitive setting and solved and refined in the space group Pī (Phase 3), including a twin law corresponding to a 180° rotation about the [010] direct lattice direction of the original C centred cell.

The asymmetric unit of the structure in Phase 3 again consists of two separate dinuclear units (Z′ = 2) and four methanol solvent molecules, as shown in Figure 3.6.

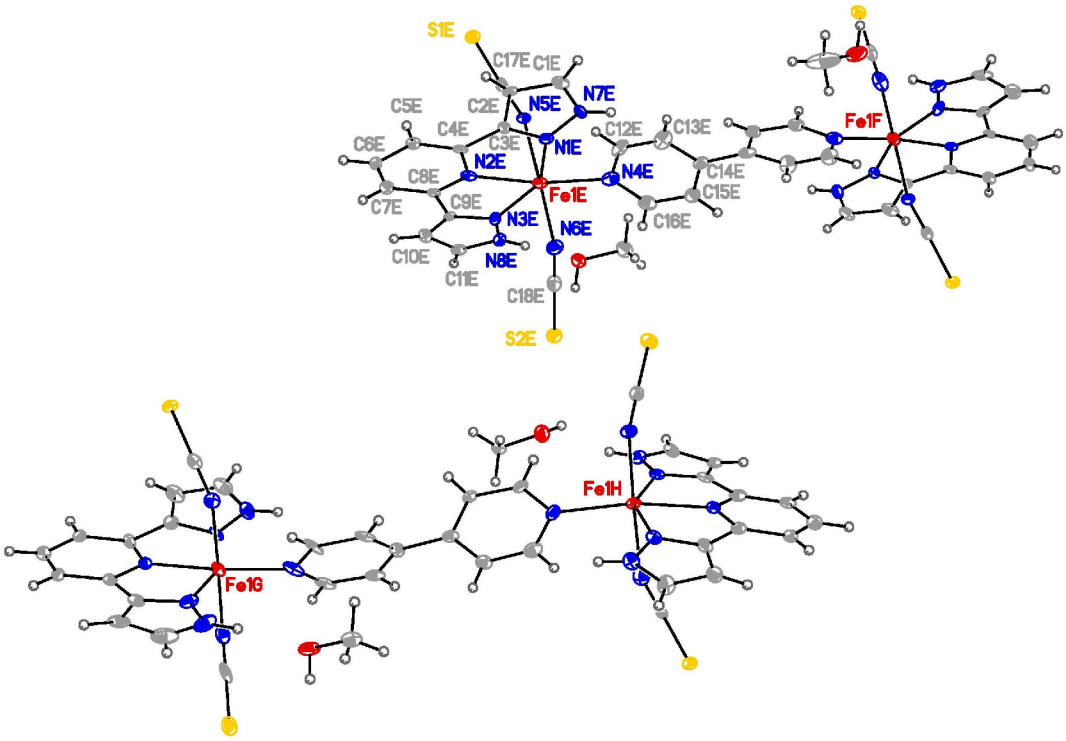

Figure 3.6. Asymmetric unit of the title compound at 30 K in the space group Pī (Phase 3). ADPs are drawn at 50% probability. The numbering scheme is shown for the half molecule containing Fe1e but is consistent throughout the structure, replacing the suffix with that of the associated iron atom

Two of the four unique Fe atoms (Fe1F and Fe1G) have undergone a spin transition as evidenced by the FeN_6 octahedral volumes and Fe – N bond distances, as shown in Table 3.4 and Table 3.5.

Table 3.4. Volume of coordination polyhedron for the four unique iron atoms at 30K

	Octahedral volume (Å^3)
Fe1E	13.02(1)
Fe1F	10.47(1)
Fe1G	10.59(1)
Fe1H	12.98(1)

Table 3.5. Fe – N bond distances (Å) for the structure at 30K

	N1	N2	N3	N4	N5	N6
Fe1E	2.218(4)	2.152(3)	2.198(4)	2.185(3)	2.156(3)	2.106(4)
Fe1F	2.014(4)	1.981(3)	2.040(4)	2.005(4)	2.006(3)	1.974(4)
Fe1G	2.043(4)	1.975(3)	2.047(4)	2.027(3)	2.003(3)	1.972(3)
Fe1H	2.211(4)	2.153(3)	2.207(4)	2.187(3)	2.142(4)	2.101(3)

3.3.5 Structure at 30 K after laser irradiation – Phase 4

After irradiation with a laser (670 nm, 5 mW) for 1 hour, another full data set was collected. The unit cell volume showed a slight increase of 1.8% from the Phase 3 structure, consistent with the excitation of the LS centres to a meta-stable high spin (HS*) state. The structure was largely comparable to that in Phase 3, with the exception that all iron centres were now HS or HS*, as indicated by the FeN_6 octahedral volumes and Fe – N bond distances, as shown in Table 3.6 and Table 3.7 respectively.

Table 3.6. Volume of coordination polyhedron for the four unique iron atoms at 30K after laser irradiation

	Octahedral volume (Å^3)
Fe1I	12.94(2)
Fe1J	12.99(2)
Fe1K	13.04(2)
Fe1L	12.91(2)

Table 3.7. Fe – N bond distances (Å) for the structure at 30K after laser irradiation

	N1	N2	N3	N4	N5	N6
Fe1I	2.224(5)	2.151(4)	2.189(5)	2.172(4)	2.143(4)	2.106(4)
Fe1J	2.204(5)	2.136(4)	2.239(5)	2.149(5)	2.171(5)	2.099(4)
Fe1K	2.215(5)	2.155(4)	2.209(4)	2.187(4)	2.105(5)	2.153(5)
Fe1L	2.196(5)	2.141(4)	2.223(5)	2.153(5)	2.138(5)	2.120(4)

This meta-stable high spin structure is more closely related to the structure of the mixed spin Phase 3 than to either of the other fully HS Phases 1 and 2, revealing a differentiation between the thermally accessed high spin structures and the light induced HS phase.

Table 3.8. Selected crystallographic data for Phases1 to 4

	Phase 1	**Phase 2**	**Phase 3**	**Phase 4**
Temperature /K	290(2)	140(2)	30(2)	30(2)
Crystal system	Monoclinic	Monoclinic	Triclinic	Triclinic
Space group	$P2_1/n$	Cc	Pī	Pī
Spin State	HS	HS	1:1 HS:LS	HS
a/Å	15.6644(14)	30.9879(16)	15.8910(7)	16.0463(14)
b/Å	8.1491(8)	16.1140(8)	17.3839(7)	17.3628(16)
c/Å	18.5720(17)	19.6161(10)	18.3423(8)	18.5495(17)
α/°			72.048(1)	72.178(1)
β/°	110.239(2)	117.524(1)	90.001(1)	89.932(1)
γ/°			62.798(1)	62.558(1)
Volume/Å^3	2224.4(4)	8686.4(8)	4227.3(3)	4306.2(7)
Z′/Z	0.5/2	2/8	2/4	2/4
ρ_{calc} mg/mm^3	1.473	1.509	1.550	1.522
μ/mm^{-1}	0.894	0.916	0.941	0.924
F(000)	1012	4048	2024	2024
Crystal size /mm	0.4 × 0.31 × 0.26	0.4 × 0.31 × 0.26	0.4 × 0.31 × 0.26	0.4 × 0.31 × 0.26
Theta range for data collection	2.10 to 29.10°	1.46 to 30.45°	2.30 to 28.29°	2.40 to 28.07°
Index ranges	-21 ≤ h ≤ 21 -11 ≤ k ≤ 11 -10 ≤ l ≤ 25	-43 ≤ h ≤ 44 -22 ≤ k ≤ 22 -27 ≤ l ≤ 27	-21 ≤ h ≤ 20 -22 ≤ k ≤ 22 -24 ≤ l ≤ 23	-20 ≤ h ≤ 19 -21 ≤ k ≤ 21 -24 ≤ l ≤ 24
Reflections collected	15788	51086	72991	29675
Independent reflections	5873	22236	19179	18027
R_{int}	0.0253	0.0269	0.0374	0.0292
Data/restraints/parameters	5873/15/290	22236/38/1118	19179/48/1125	18027/42/987
Goodness-of-fit on F^2	1.020	1.074	1.036	0.993
Final R indexes [I>2σ (I)]	R1 = 0.0363 wR2 = 0.0892	R_1 = 0.0391 wR_2 = 0.0964	R_1 = 0.0405 wR_2 = 0.0962	R_1 = 0.0480 wR_2 = 0.1370
Final R indexes [all data]	R1 = 0.0617 wR2 = 0.1028	R_1 = 0.0592 wR_2 = 0.1066	R_1 = 0.0473 wR_2 = 0.0995	R_1 = 0.0634 wR_2 = 0.1502
Largest diff. peak/hole /eÅ^{-3}	0.396/-0.326	0.706/-0.342	0.564/-0.563	1.388/-0.615

3.3.6 Structure at 17 kbar and ambient temperature – Phase 5

A preliminary high pressure study of [{Fe(bbp)(NCS)$_2$}$_2$4,4′-bipy]•2MeOH was undertaken to investigate further the interplay between the phase transitions and the magnetic properties, and to establish if a fully LS structure was accessible, as high pressure is known to favour the LS state.[8] Figure 3.7 shows the asymmetric unit of the compound in Phase 5.

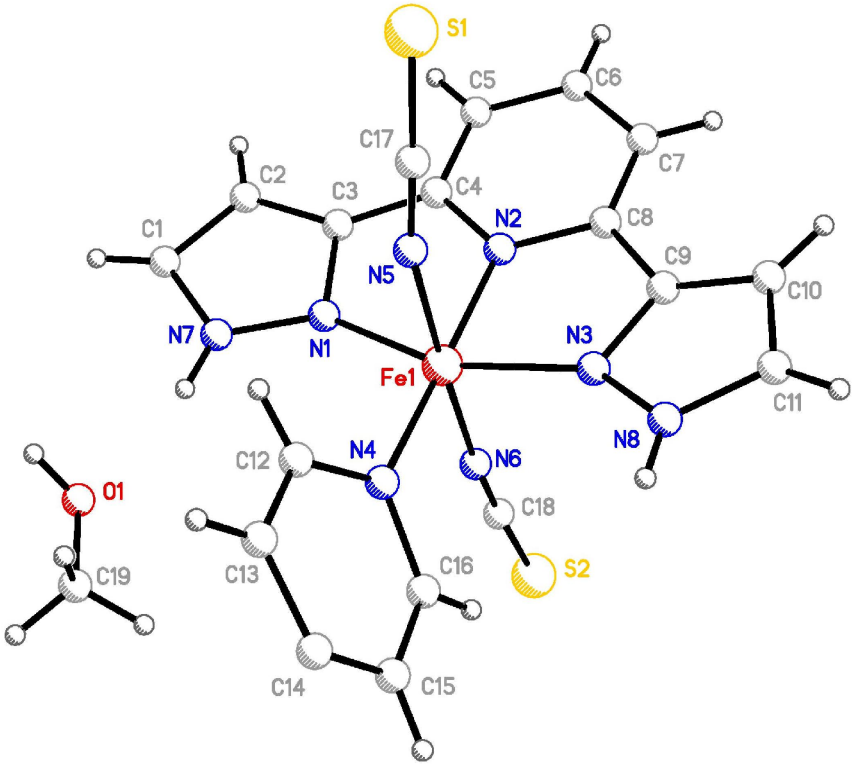

Figure 3.7. Asymmetric unit of [{Fe(bbp)(NCS)$_2$}$_2$4,4′-bipy]•2MeOH at 17 kbar - Phase 5

The structure of the title complex in Phase 5 is isostructural with that observed in Phase 1. The volume of the coordination polyhedron is 9.65(5) Å^3 and the bond lengths range from 1.91(1) Å to 1.98(2) Å. All of these values point strongly towards a LS iron centre and, as all Fe centres are equivalent in this phase, it is clear that both iron centres in the dinuclear molecule have undergone a spin transition. From analysis of the magnetic data, it is apparent that this phase is not thermally accessible, at least down to 4 K. The data would benefit from recollection with a higher intensity X-ray source and possibly using more than one crystal, yielding a greater number of data, thereby increasing both the redundancy and completeness of the dataset. This would

hopefully allow anisotropic refinement of the atoms due to a greater data:parameters ratio. Selected crystallographic information for Phase 5 can be found in Table 3.9.

Table 3.9. Selected crystallographic information for the title compound at 17 kbar

	Phase 5
Pressure /kbar	17(1)
Temperature/K	293(2)
Crystal system	Monoclinic
Space group	$P2_1/n$
a/Å, b/Å, c/Å	14.6472(9), 7.6453(10), 17.9384(14)
α/°, β/°, γ/°	90.00, 112.611(6), 90.00
Volume/Å^3	1854.4(3)
Z	4
ρ_{calc}mg/mm^3	1.767
μ/mm^{-1}	1.073
Crystal size/mm^3	0.09 × 0.26 × 0.28
Theta range for data collection	4.28 to 20.81°
Reflections collected	3981
Independent reflections	1164, R_{int} = 0.1190
Data/restraints/parameters	1164/28/136
Goodness-of-fit on F^2	1.439
Final R indexes [I>2σ (I)]	R_1 = 0.1032, wR_2 = 0.2195
Final R indexes [all data]	R_1 = 0.1650, wR_2 = 0.2534
Largest diff. peak/hole / e Å^{-3}	0.668/-0.654

It would be useful to investigate the nature of any intermediate phases to help elucidate the mechanism of the pressure-induced transition, using both variable pressure experiments at constant temperature and variable temperature experiments at elevated pressure. There are a variety of techniques that could be used to accomplish this, including Raman, Mössbauer, magnetometry and crystallography.

One would expect any supercell reflections similar to those observed in Phase 2 to be rather weak, consequently any crystallographic investigation of intermediate pressures would most likely require synchrotron radiation.

While it is certainly possible that the pressure-induced phase transition does not occur *via* a mixed spin intermediate phase (analogous to Phase 3), observing these differences and the reasons behind them would help to shed light on the interplay between crystallographic phase transitions and spin crossover. For example, does the first phase transition (Phase 1 to Phase 2) occur under pressure to provide non-equivalent iron sites? If not, does this preclude the possibility for a mixed spin intermediate in this system?

It has been shown using DFT studies that the difference in angle between the rings of the 4,4'-bipy molecule is 37.2° in the gas phase and that forcing them to be coplanar increases the interaction between the metal centres.[9] If the first phase transition (that removes the planarity of the bipy rings) does not occur as a result of the application of external pressure, one might expect to observe greater cooperativity between the Fe centres at each end of the molecule. This might result in the spin transition proceeding from HS to LS in one step with 100% conversion.

3.3.7 Molecular Packing

The molecular packing at 290 K is shown in Figure 3.8. There is a network of non-bonding short contacts between [{Fe(bbp)(NCS)$_2$}4,4'-bipy] molecules involving N-H···S and C-H···S interactions. These interactions form infinite sheets in the (101) plane (Figure 3.8i), which stack perpendicular to this plane (Figure 3.8ii). These sheets are connected by an intricate network of short contacts, which extend throughout the lattice. The packing motifs are consistent in all phases but the distances between atoms involved in these interactions vary, as shown in Table 3.10.

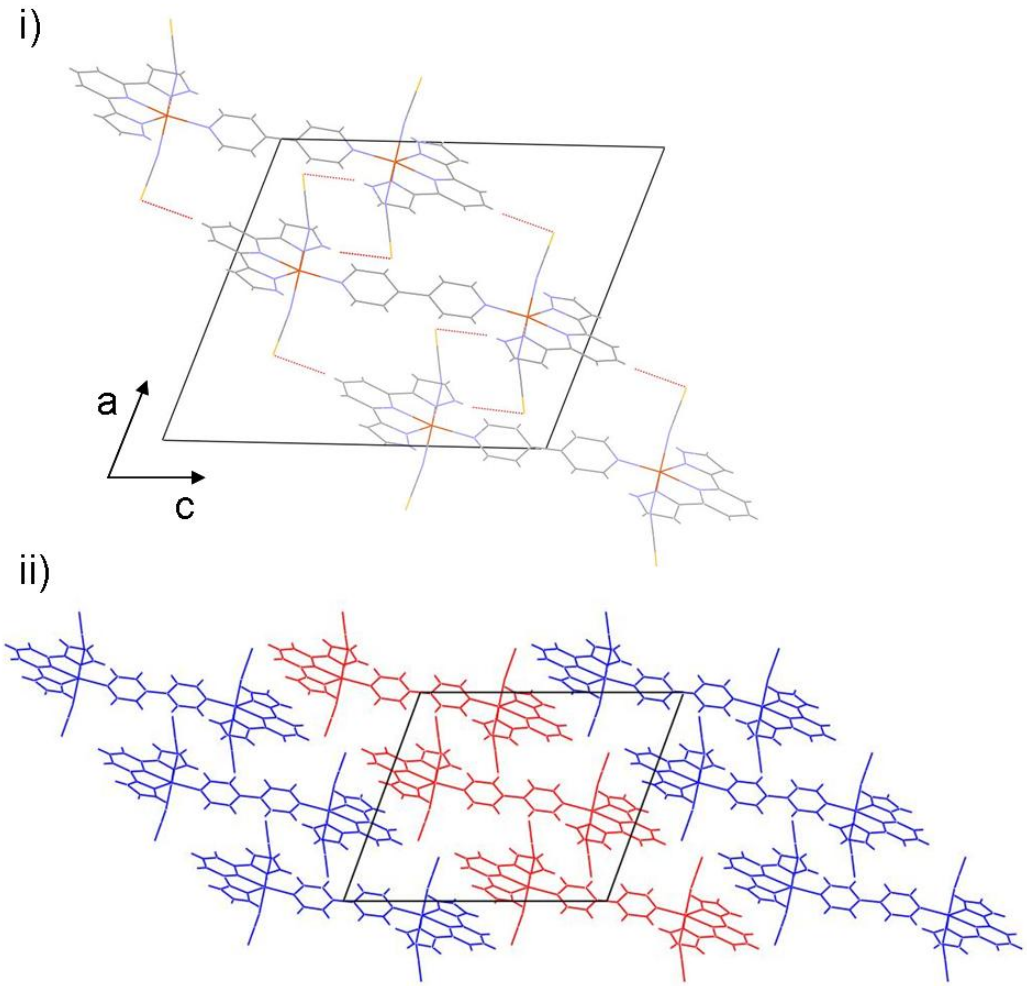

Figure 3.8. Molecular packing of [{Fe(bbp)(NCS)$_2$}$_2$4,4′-bipy] molecules. i) Sheets formed in the 101 plane. Non-bonding short contacts are shown with red dashed lines. ii) Stacking of the sheets in 3 dimensions. Different colours indicate alternate sheets. Solvent molecules have been omitted for clarity

Table 3.10. Distances between non-hydrogen atoms for the interactions through which the molecules form 2-D sheets in the 101 plane. For Phases 2, 3 and 4 where four unique interactions of each type are present the range of distances is given. Estimated standard deviations associated with each value do not exceed 0.003 Å unless otherwise stated

Interaction	Phase 1	Phase 2	Phase 3	Phase 4	Phase 5
N-H···S (Å)	3.422	3.362 - 3.427	3.317 - 3.369	3.377 - 3.437	3.22(1)
C-H···S (Å)	3.732	3.699 - 3.737	3.630 - 3.732	3.665 - 3.769	3.48(2)

It is clear that the contacts between molecules are different in all phases. It is to be expected that molecules would be closer together in Phase 3, where there is a contraction of the unit cell volume as a result of the spin transition. Between Phases 1 and 2 there is a significant decrease in some of the interactions, showing that the symmetry breaking affects not only the twisting of the linking bipyridine unit, but also interactions between the molecules. However, there appears to be little direct correlation between the distance of these interactions in Phase 2 and the centres which have undergone a spin crossover in Phase 3.

In Phase 5, the high pressure phase, the contacts are much smaller than in any other phase. This is a result not only of the spin crossover, but also of the applied pressure, and it would be difficult to separate these two effects without further experiments.

3.3.8 Structural Comparison

The structural behaviour of this sample is complex, while for the most part this has little effect on the assignment of spin state of each iron centre, it is necessary to investigate it fully in order to gain insight into the mechanism of the transitions. A summary of the phases observed on cooling of this sample is given in Figure 3.9, along with transformation matrices relating these Phases. Phases 4 and 5 have been omitted as they are isostructural to Phases 3 and 1 respectively.

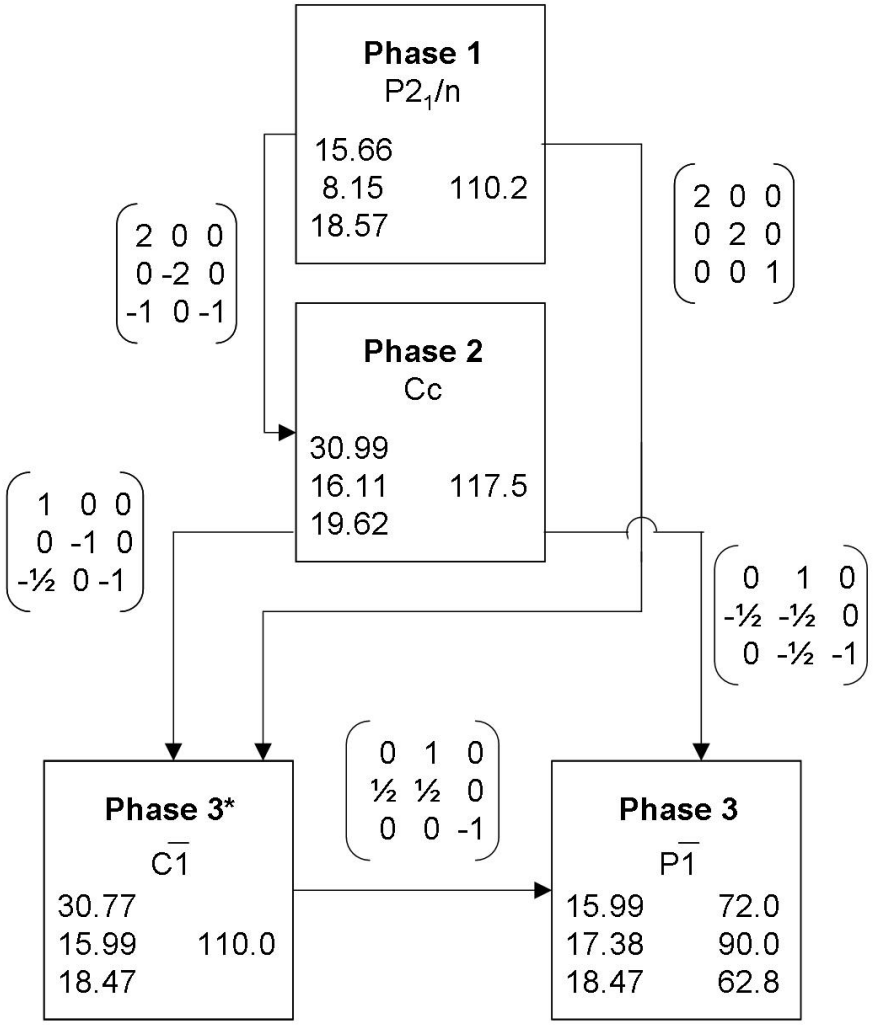

Figure 3.9. Relationship between Phases 1, 2, 3 and 3*. Matrices refer to transformations in the direction of the arrows

The crystal structure in Phase 1 seems to be an accurate and reasonable description of the system at high temperatures and is in agreement with the published structure. On cooling through the first phase transition to Phase 2, it is apparent that the description of the structure becomes more complex.

This situation where the batch scale factor for an inversion twin component refines close to 0.5 might often suggest missed symmetry and hence that the space group assignment is incorrect. The true space group in this situation might be expected to be C2/c, and indeed this is suggested by PLATON[10] as the true space group. In C2/c the asymmetric unit is 2 independent half-dinuclear molecules and 2 methanol molecules.

Refinement indicators are not acceptable and inspection of the structure reveals that this model is not chemically sensible; the intermolecular distances of adjacent molecules become unreasonably short and the structure is obviously incorrect. Attempts were made to solve this structure in C2/c, as well as to transform the refined Cc structure to C2/c (using PLATON and Olex2); all attempts failed to produce a chemically sensible model.

In a further effort to determine if the inversion twin really corresponds to a missed inversion centre, the structure was transformed back to the primitive cell and refined in space groups Pī and P1 including an inversion twin. In Pī the refinement is significantly poorer than in P1, as shown in Table 3.11.

The inversion twin could correspond to domains, each with opposite handedness as opposed to the standard distribution of symmetry centres as seen in space group Pī. A high degree of *pseudo* symmetry in this system is to be expected; if the bipy units are ignored the 4 iron centres show very little difference. This may be quantified by looking at the root mean squared deviation (RMSD) (Equation 1) of pairs of related atoms.

$$\sqrt{\frac{1}{n}\sum_{i=1}^{n}\left(v_{ix}-w_{ix}\right)^2+\left(v_{iy}-w_{iy}\right)^2+\left(v_{iz}-w_{iz}\right)^2}$$

Equation 3.1

The RMSDs of each half-molecule with and without the bipyridine ring was calculated using Olex2. The program takes a rigid superposition of the two half molecules (Figure 3.10), which minimizes the RMSD, and this minimum is returned. The values obtained using this procedure are shown in Table 3.12. In each case hydrogen atoms were removed prior to performing the superposition. During refinement H atoms were treated as riding on the parent carbon or nitrogen, hence including them in the superposition process would increase the relative contribution from the parent atom.

Table 3.11. Crystal data and refinement indicators for the structure after refinement in space groups Pī and P1 with an inversion twin

Space Group	Pī	P1
Empirical formula	$C_{38}H_{32}Fe_2N_{16}O_2S_4$	
Formula weight	985.24	
Temperature	140(2)	
Crystal system	Triclinic	
a/Å, b/Å, c/Å	16.1140(16), 17.5(5), 19.6161(8)	
α/°, β/°, γ/°	65.795(1), 90.000(1), 62.525(1)	
Volume/Å^3	4338(1)	
Z	4	
ρ_{calc}mg/mm^3	1.507	
μ/mm^{-1}	0.916	
Crystal size / mm	0.4 × 0.31 × 0.26	
Theta range for data collection	1.17 to 30.45°	
Reflections collected	52072	
Independent reflections	23672 R_{int} = 0.0271	41906 R_{int} = 0.0191
Data/restraints/parameters	23672/0/1124	41906/3/2250
Goodness-of-fit on F^2	2.929	1.007
Final R indexes [I>2σ (I)]	R_1 = 0.1121 wR_2 = 0.4287	R_1 = 0.0423 wR_2 = 0.0986
Final R indexes [all data]	R_1 = 0.1369 wR_2 = 0.4364	R_1 = 0.0684 wR_2 = 0.1140
Largest diff. peak/hole	0.875/-1.149	0.527/-0.434

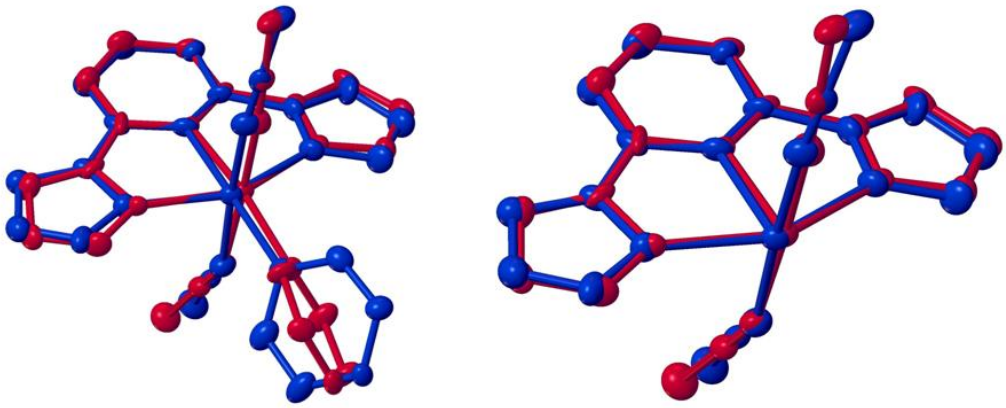

Figure 3.10. Graphical display of rigid superposition of the two half molecules containing Fe1B (red) and Fe1D (blue), which minimizes the RMSD in a. the presence and b. the absence of bipyridine ligand

Table 3.12. RMSD values (Å) for each unique combination of molecules with and without bipyridine rings. AB denotes the RMSD value for molecules containing Fe1A and Fe1B and so on

	AB	AC	AD	BC	BD	CD
With bipy	0.465	0.410	0.205	0.170	0.588	0.551
Without bipy	0.203	0.235	0.120	0.146	0.216	0.292

Smaller values of the RMSD indicate greater structural similarity between the molecules. Comparing the values of the RMSD with and without the influence of the bipyridine ligand reveals a weaker relationship between the bipyridine ligands than the rest of the molecule. The bipyridine unit is much lighter than the rest of the molecule and the X-ray data will be skewed in a manner so as to appear *pseudo*-centrosymmetric.

The structure modelled in the space group Cc and refined with an inversion twin shows good refinement statistics, a chemically sensible model and well defined ADPs. Consequently, it was considered the best way in which to model the structure at this temperature.

Comparison of Phases 2 and 3 reveals some interesting points that should be noted. The asymmetric unit of both phases (2 dinuclear units and 4 methanol molecules) appear to be the same. However, closer inspection reveals that the 2 unique molecules in Phase 2 are in fact symmetry-related in Phase 3 and *vice versa*, as shown in Figure 3.11. During the spin transition one iron atom on each molecule becomes low spin, with the other remaining in the high spin state. The resulting reduction in volume of the Fe octahedron could enable, and perhaps even force, the relative orientation of the bipy rings to change.

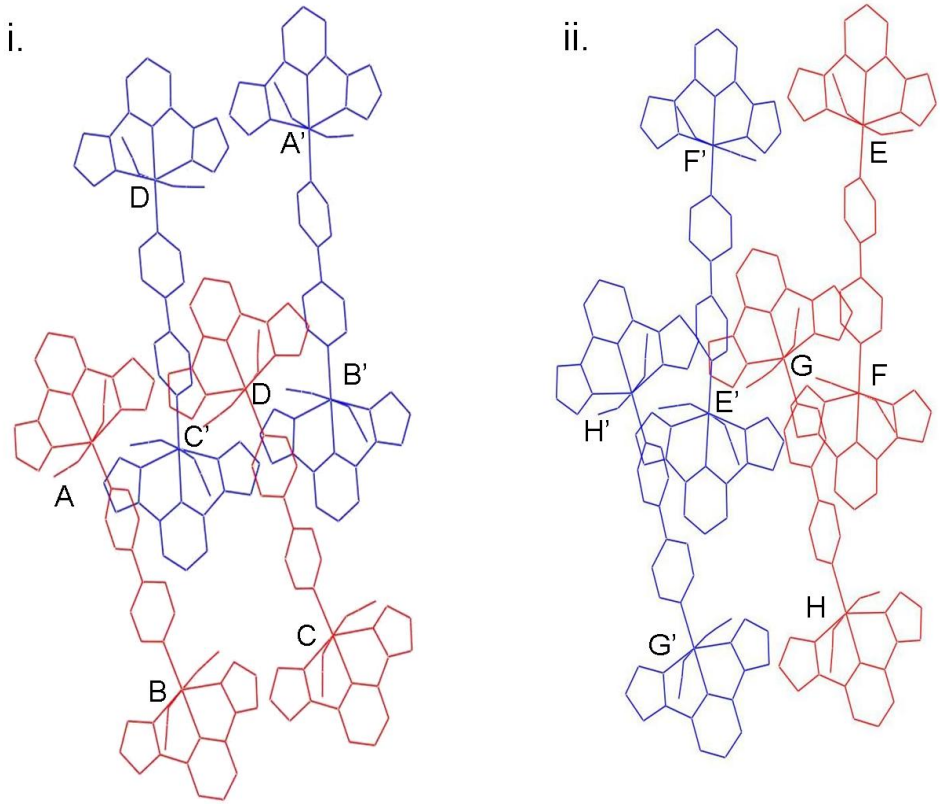

Figure 3.11. i) Asymmetric unit in red for the structure at 140 K in space group Cc and symmetry related molecules in blue. ii) Asymmetric unit in red for the structure at 30 K in space group Pī and symmetry related molecules in blue. Solvent molecules and hydrogen atoms have been omitted for clarity

It is possible to transform the cell setting in Phase 2 to that of the Cī setting of Phase 3*, as shown in Figure 3.9. Further transforming this cell to the reduced cell (Figure 3.9) allows refinement of the Phase 2 structure in the Phase 3 (Pī) setting (and thus the same

asymmetric unit) and hence allows us to assess whether these two phases really do have distinct asymmetric units.

Refinement of Phase 2 data in the Phase 3 setting affords reasonable refinement statistics; however the ADPs of the central bipy rings are greatly distorted, as shown in Figure 3.12. This is a relatively minor component of the structure and inadequate modelling of these rings would not be expected to significantly affect refinement statistics. The refinement in this cell setting is significantly inferior to that in the Cc setting described above.

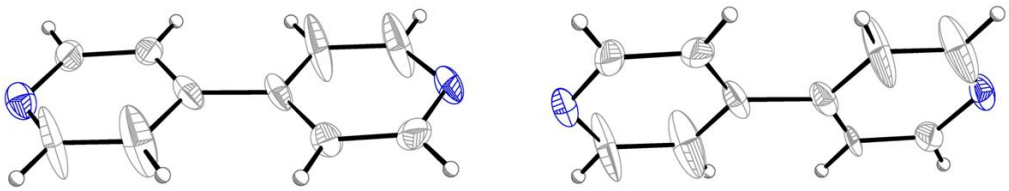

Figure 3.12. Distortion of ADPs in central bipyridine rings for the Phase 2 data modelled with the Phase 3 asymmetric unit

Conversely, an attempt was also made to model the Phase 3 data in the Phase 2 (Cc) setting, also with an inversion twin. This resulted in a much worse structure, as it forces HS and LS iron atoms to be symmetrically equivalent, making the distribution of spin states appear disordered throughout the crystal. This has a serious implication for the analysis of the nature of the spin transition; the quality of the refinement in this setting is however so poor that it should be obvious that the Pī (Cī) model (with an ordered distribution of spin states) is by far superior to describe the structure of Phase 3.

3.3.9 Selenium Analogue

A selenium analogue (where thiocyanate groups of the title compound are replaced by selenocyanate groups) has been synthesised by the same group in Bordeaux. While the as yet unpublished magnetic data are comparable to those of the sulfur compound, with a slight difference in the transition temperature, the structural behaviour is somewhat more complex. The structure at 290 K is isostructural to that of Phase 1 of

the sulfur complex, and is comparable in quality, as shown by the selected crystallographic information given in Table 3.13.

Table 3.13. Selected crystallographic information and refinement indicators for [[Fe(bbp)(NCSe)$_2$}$_2$4,4'-bipy]•2MeOH at 290 K

	Selenium 290 K
Empirical formula	$C_{38}H_{34}$ $Fe_2N_{16}O_2Se_4$
Formula weight	1174.35
Temperature	290(2)
Crystal system	Monoclinic
Space group	$P2_1/n$
a/Å, b/ Å, c/Å	15.890(2), 8.2040(14), 18.744(3)
β/°	109.705(7)
Volume/Å^3	2300.4(6)
Z′/Z	0.5/2
ρ_{calc}mg/mm^3	0.848
μ/mm^{-1}	1.924
Crystal size/mm	0.29 × 0.21 × 0.19
Theta range for data collection	2.31 to 25.03°
Reflections collected	2688
Independent reflections	2528, R_{int} = 0.0248
Data/restrains/parameters	2528/12/290
Goodness-of-fit on F^2	0.923
Final R indexes [I>2σ (I)]	R_1 = 0.0387, wR_2 = 0.0787
Final R indexes [all data]	R_1 = 0.0754, wR_2 = 0.0895
Largest diff. peak/hole	0.244/-0.303

The first (purely structural) phase transition occurs in an analogous manner to the one described for the sulfur system, and Phase 2 of the selenium complex appears isostructural with that of sulfur, although of significantly poorer quality. This is manifested by extremely irregularly shaped ADPs and a suggested weighting scheme that implies poorly fitting high angle data. It is not yet apparent whether this is the result of poorer crystal quality or a real feature of the phase transition in selenium that distinguishes the structural behaviour from the sulfur case. It should however be

noted that the crystal quality at 290 K was of comparable quality to that of the sulfur complex.

At 30 K there are supercell reflections that indicate a structure with 8 times the volume of that observed in Phase 1, i.e. a doubling of the c-axis, in addition to the doubling of the a- and b-axes that is observed in the sulfur complex. These supercell reflections are very weak, and it is not clear whether they represent another thermally accessible phase in addition to Phase 3 or whether this structure with an eight fold increase in volume is the third phase for the selenium analogue. Structure refinement of this 30 K phase is not possible with the current data – the additional reflections are extremely weak and the correlation between refined parameters is extremely high. Additional data collection at 30 K using a higher intensity source may be required to fully understand the structural behaviour of this selenium complex and to explain why this is different from the sulfur analogue.

3.4 Conclusions and Perspectives

Figure 3.13 illustrates the behaviour of [{Fe(bbp)(NCS)$_2$}$_2$4,4′-bipy]•2MeOH as a result of variations in temperature, pressure and as a result of light irradiation.

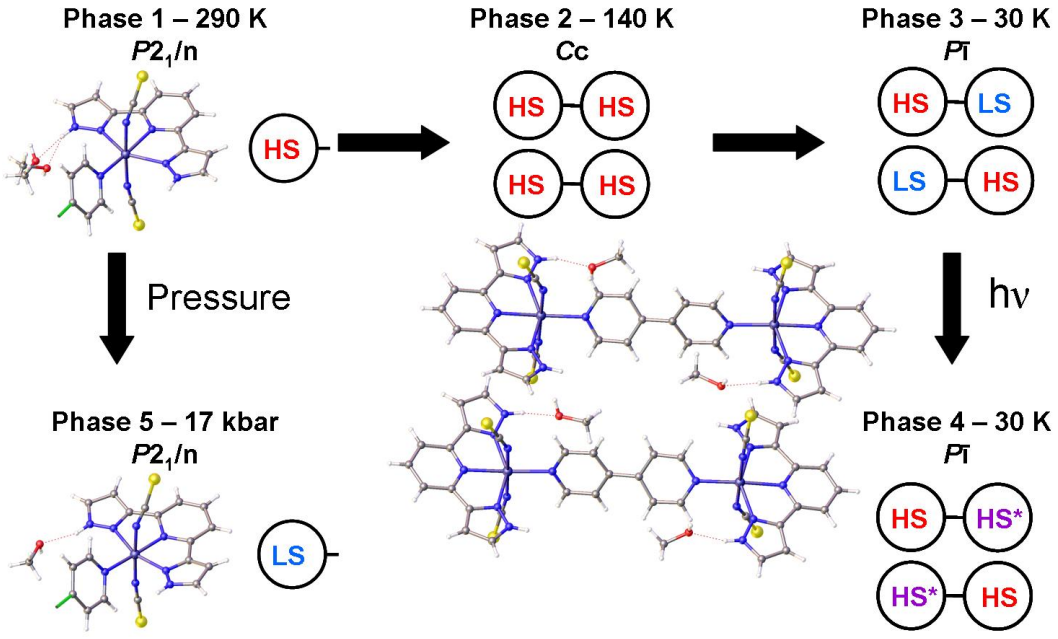

Figure 3.13. Phase diagram of [{Fe(bbp)(NCS)$_2$}$_2$4,4′-bipy]•2MeOH showing the effect of temperature, pressure and light irradiation on the sample

While the structural behaviour is complex, there are clear conclusions that can be drawn about the spin transitions.

The twisting of the bridging 4,4'-bipyridine ligands occurs during a purely structural phase transition, generating four crystallographically distinct iron centres in Phase 2. Two of these four independent centres undergo a subsequent spin transition, resulting in an ordered mixed spin system – Phase 3. These LS centres can be forced back into a meta-stable HS state (Phase 4) using laser irradiation. High pressure generally favours the low spin state and in this case stabilises the 100% LS phase, which is not thermally accessible.

The history of the sample determines the structural features of the high spin phase, i.e. the light-induced fully HS phase is not isostructural with either of the two thermally accessible high spin phases.

Further work in this area should focus on two areas, the selenium analogue of this species and the mechanism of the pressure-induced phase transition.

A more detailed structural investigation of the selenium analogue to the title complex should be carried out using a higher intensity source. The structural behaviour of this Se-containing compound appears to differ significantly from the sulfur compound. While it is not unprecedented for systems that are isostructural at temperatures above the spin transition to undergo very different phase and spin transitions,[11] it is certainly unusual. This may be interpreted as this structure type having many secondary minima in the potential energy surface, which may differ slightly depending on the chemical nature of the complexed ligands as well as the spin state. Understanding the differences between these two related compounds will shed light on the forces driving crystallographic phase transitions and spin crossover events, and how these are influenced by one another.

Elucidation of the mechanism of the pressure-induced phase transition will have implications for other systems that show mixed spin intermediate states. It has been shown that pressure can dramatically affect the nature of the spin transition, not only raising the temperature of the transition (through stabilisation of the LS state), but also by making the transition more gradual.[8] Other unusual features have been observed as a result of increasing applied pressure, including inducing a partial or complete spin

transition in a mononuclear Fe^{II} compound that does not show SCO properties at ambient pressure.[12] There are also reports of pressure suppressing the second step of a two step spin transition,[13] inducing a second step in a system showing half-step (incomplete) thermal SCO[14] and inducing or widening hysteresis[15] in the spin transition curve. These more unusual features occur largely as a result of pressure induced structural changes, and as such provide a fascinating insight into how structure affects spin crossover properties. Initial investigations of this sample would benefit from variable temperature magnetic studies at a range of pressures, which would provide an overview of the behaviour of this complex. Subsequent crystallographic studies should help to explain these properties in terms of structural features which are apparent at different pressures.

---

[1] D. Fedaoui, Y. Bouhadja, A. Kaiba, P. Guionneau, J.-F. Létard, and P. Rosa, *Eur. J. Inorg. Chem.*, 2008, 1022

[2] *SMART-NT, Data Collection Software, version 6.1,* Bruker Analytical X-ray Instruments Inc., Madison, WI, USA, 2000

[3] *SAINT-NT, Data Reduction Software, version 6.1*, Bruker Analytical X-ray Instruments Inc., Madison, WI, USA, 2000

[4] G. M. Sheldrick, *Acta Cryst.*, 2008, **A64**, 112

[5] O. V. Dolomanov, L. J. Bourhis, R. J. Gildea, J. A. K. Howard, H. Puschmann, *J. Appl. Cryst.*, 2009, **42**, 339

[6] J. Cosier and A. M. Glazer, *J.Appl. Cryst.*, 1986, **19**, 105

[7] A. E. Goeta, L. K. Thompson, C. L. Sheppard, S. S. Tandon, C. W. Lehmann, J. Cosier, C. Webster and J. A. K. Howard, *Acta Cryst.*, 1999, **C55**, 1243

[8] V. Ksenofontov, A. B. Gaspar, P. Gütlich, *Top. Curr. Chem.*, 2004 **235**, 23

[9] L. Ould-Moussa, M. Castellá-Ventura, E. Kassab, O. Poizat, D.P. Strommen and J.R. Kincaid, *J. Raman Spectrosc*, 2000, **31**, 377

[10] A. L. Speck, "PLATON, a multipurpose crystallographic tool." Utrecht University, Utrecht, The Netherlands, 2001

[11] M. Hostettler, K. W. Törnroos, D. Chernyshov, B. Vangdaal and H.-B. Bürgi, *Angew. Chem. Int. Ed.*, 2004, **43**, 4589

[12] A. B. Gaspar, M. C. Muñoz, N. Moliner, V. Ksenofontov, G. Levchenko, P. Gütlich and J. A. Real, *Monats. Chem.*, 2003, **134**, 285

[13] S. Bonnet, G. Molnár, J. Sanchez Costa, M. A. Siegler, A. L. Spek, A. Bousseksou, W.-T. Fu, P. Gamez, and J. Reedijk, *Chem. Mater.*, 2009, **21**, 1123

[14] A. Bhattacharjee, V. Ksenofontov, H. A. Goodwin and P. Gütlich, *J. Phys. Condens. Matter*, 2009, **21**, 026011

[15] V. Ksenofontov, H. Spiering, A. Schreiner, G. Levchenko, H. A. Goodwin and P. Gütlich, *J. Phys. Chem. Solids*, 1999, **60**, 393

4 The LIESST Effect in [Fe(bapbpy)(NCS)$_2$]

4.1 Introduction

The complex [Fe(bapbpy)(NCS)$_2$], where bapbpy = N-(6-(6-(pyridin-2-ylamino)pyridin-2-yl)pyridin-2-yl)pyridin-2-amine (Figure 4.1), is known to undergo a two-step thermal spin transition involving an ordered mixed spin intermediate state.[1,2]

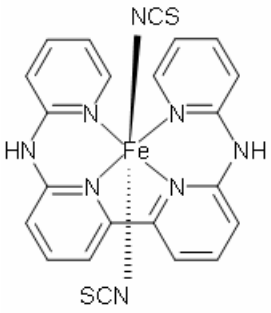

Figure 4.1. [Fe(bapbpy)(NCS)$_2$]

Both steps involved in the spin transition are first order, show hysteresis and are accompanied by a crystallographic phase transition. In the intermediate state one third of the iron sites are in the high spin (HS) state and the remaining sites are low spin (LS). A summary of the magnetic behaviour is given in Figure 4.2.

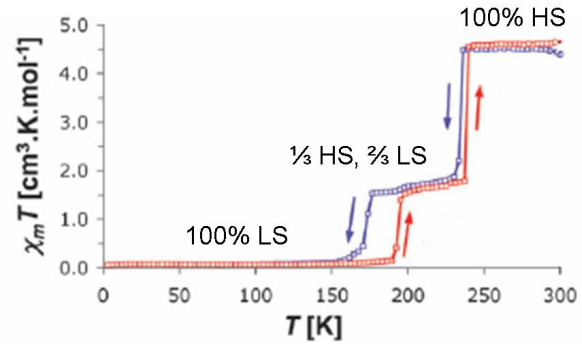

Figure 4.2. Magnetic behaviour of the title compound as a function of temperature.[1*] Blue points indicate cooling mode and red heating

*Adapted from S. Bonnet, M. A. Siegler, J. Sánchez Costa, G. Molnár, A. Bousseksou, A. L. Spek, P. Gamez and J. Reedijk, *Chem. Commun.*, 2008, 5619 Reproduced by permission of The Royal Society of Chemistry

The structure of the molecule at 295 K, 190 K and 110 K has been previously determined by single crystal X-ray diffraction and reported in the literature by S.

Bonnet *et al*.[1] The HS phase is in the space group C2/c; on undergoing the first spin transition the volume of the unit cell increases by a factor of three, increasing the number of molecules in the asymmetric unit from half a HS molecule (Z′ = ½ HS) to half a HS molecule and one LS (Z′ = ½ HS, 1 LS). The space group of this intermediate phase is also C2/c. During the second transition the volume of the unit cell is comparable to that of the HS phase, but the space group changes to Cī (a non standard centred setting of the triclinic space group Pī) and the asymmetric unit contains one LS molecule (Z′ = 1 LS). The final phase includes twinning involving a 2-fold rotation around the b-axis of the C-centred cell (the [110] direction in the primitive Pī setting).[3]

The complex shows LIESST behaviour, which was first observed using Raman spectroscopy, but subsequently studied using SQUID magnetometry by S. Bonnet *et al*.[2] The system does not show full conversion to the HS state, with between 25% and 30% of the iron centres remaining in the LS state. An interesting feature of the LIESST effect in this sample is that the relaxation of the meta-stable high spin (HS*) back to the LS ground state shows a slight step, as shown in Figure 4.3. Raman studies suggested that the meta-stable high spin (HS*) state is likely to be isostructural with the high temperature 100% HS phase rather than the intermediate phase.

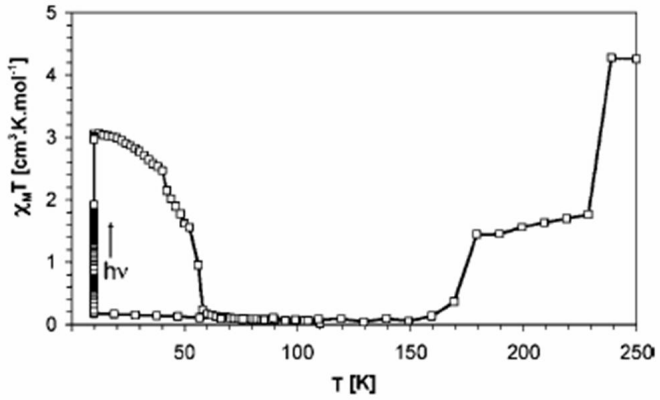

Figure 4.3. Magnetic behaviour of the title compound,[2*] showing LIESST behaviour at low temperatures and a stepped relaxation back to the LS ground state

*Reproduced with permission from S. Bonnet, G. Molnár, J. Sánchez Costa, M. A. Siegler, A. L. Spek, A. Bousseksou, W.-T. Fu, P. Gamez, and J. Reedijk, Chem. Mater., 2009, 21, 1123. Copyright 2009 American Chemical Society

Single crystal X-ray diffraction experiments were undertaken with the intention of structurally characterising the HS* state, and possibly examining the stepped relaxation behaviour.

4.2 Experimental

4.2.1 Crystal

A crystalline sample of [Fe(bapbpy)(NCS)$_2$] was obtained from Sylvesyre Bonnet at Leiden University. A suitable crystal was selected and mounted on a glass fibre using epoxy resin glue. The sample was cooled from room temperature to 250 K. A partial dataset was collected at 250 K to determine the diffraction quality of the crystal. The crystal was subsequently cooled to 200 K, where another partial dataset was acquired. The crystal was then cooled to a base temperature of 30 K. After a full sphere of data had been collected, the sample was irradiated with a red laser (670 nm, 5mW) for 30 minutes and another full sphere of data was collected. A cooling rate of 120 K/hour was used throughout this investigation and was chosen as it is the same as that used in the previous study.[3] It resulted in full conversion of the crystal to each expected phase with no significant deterioration in crystal quality. The temperature of the crystal was controlled using the Oxford Cryosystems Helix[4] throughout.

4.2.2 Diffraction

X-ray data were collected using graphite-monochromated Mo-Kα radiation (λ = 0.71073 Å) on a Bruker SMART-CCD 1 K diffractometer. Both 30 K datasets were collected using a combination of narrow φ- and ω-scans (0.3°) in such a way as to cover a sphere of data to a maximum resolution of 0.85 Å. The crystal to detector distance is usually set at 5.5 cm when using the Helix. However, a large degree of overlap between reflections was observed at lower temperatures and hence this distance was increased to 8 cm for both of the datasets collected at 30 K, resulting in a maximum resolution of 1 Å for the collected data. Due to the low resolution of the data all C, H and N atoms were refined using an isotropic model for their temperature factors.

4.2.3 Twinning

For the 30 K experiment, reflections were harvested from the raw frame data using the Bruker SMART software[5] and contributions from each twin component were distinguished using the reciprocal lattice viewer RLATT. Reflections from each component were indexed separately using SMART. Simultaneous integration of both components was performed using the program SAINT[6] and data were merged using TWINABS to produce both hkl4 and hkl5 format reflection files, as described in

Chapter 2.4.4. The structure was solved by direct methods from the hkl4 format file using SHELXS,[7] and refined by full-matrix least-squares on F^2 using SHELXL-97[7] and the hkl5 reflection file. Olex2[8] was used as an interface to all SHELX programs.

A similar method was used for indexing the dataset collected after laser irradiation. There were three components present in the diffraction pattern, associated with two structurally distinct domains, one of which was a non-merohedral twin. After integration, an hkl4 format reflection file was generated, which comprised only reflections associated with the light induced phase. Reflections which overlapped with those from either of the twin domains present were omitted from the file. Structure solution and refinement were both carried out using the hkl4 file.

4.3 Results

The datasets collected at 250 K and 200 K showed the quality of the crystal to be suitable to merit further study at low temperatures. The structures are known and no significant differences from the published structures were observed. However, as structural behaviour of this sample is reasonably complex, the relationships between phases are presented in Figure 4.4. All of the cell parameters presented are from this study and differ slightly from those in the literature, which is attributable to slight differences in the temperature of the data collections as well as the use of a different diffractometer to collect the data.

The structure derived from data collected after laser irradiation and the process used to determine it are best viewed in light of the structure at 30 K, prior to excitation. Consequently results from the 30 K study are also presented here in detail, despite being structurally similar to the previously reported LS phase collected at 110 K by S. Bonnet and coworkers.[1,3]

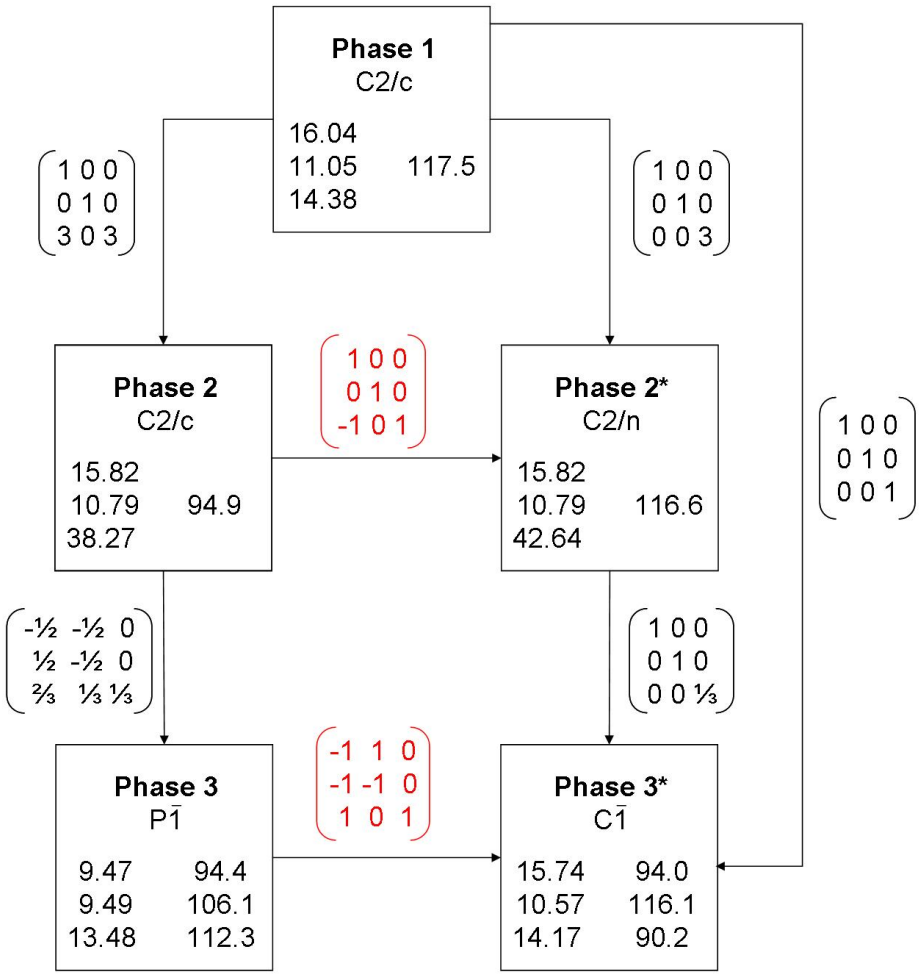

Figure 4.4. Relationship between structural phases observed in [Fe(bapbpy)(NCS)$_2$] on cooling. Phase 1 is the 100% HS at 250 K. Phase 2 is the ordered mixed spin (⅓ HS, ⅔ LS) intermediate phase at 200 K, Phase 3 is the 100% LS phase at 30 K. * indicates an unconventional cell setting used in the literature[1] to allow direct comparison between phases. Matrices shown in red are given in the literature.[3] Transformation matrices refer to the cell setting and not to the absolute value of the cell parameters, which are subject to changes imposed by the differences in temperature and spin state between phases

4.3.1 Structure at 30 K – LS Phase

As reported in the previous study,[3] the LS phase was non-merohedrally twinned about the [110] direction in the primitive cell, equivalent to a 180° rotation about the b-axis of the C-centred cell. A visual representation of the relationship between reflections from each twin component is shown in Figure 4.5, produced using RLATT.

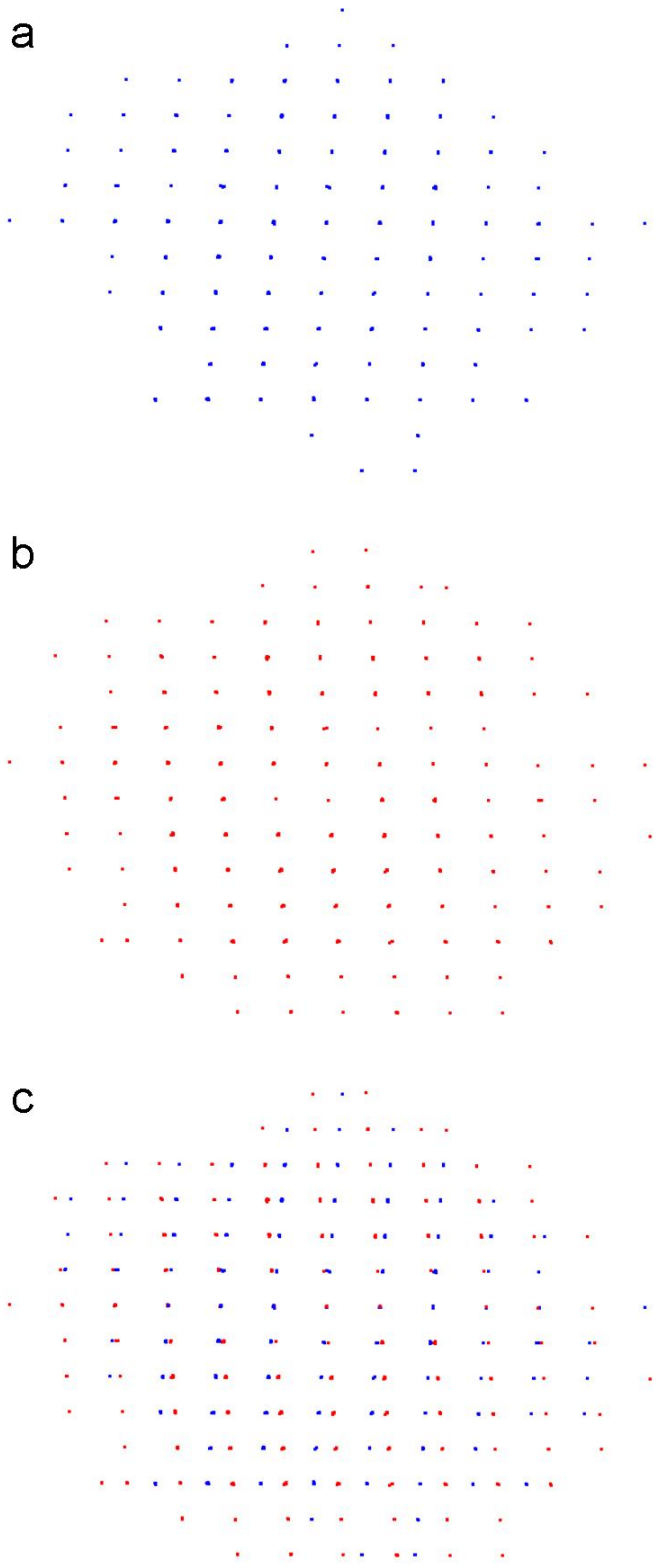

Figure 4.5. Diffraction pattern from two twin components, each shown separately in blue (a) and red (b). The total observed lattice is also shown (c)

The twin law is a symmetry element belonging to the higher symmetry previous phase. As discussed in Chapter 2, phase transitions that lower the symmetry of the system often result in *pseudo*-merohedral twinning, in which reflections from each domain overlap. However, in this case the metric symmetry of the cell also changes from monoclinic to triclinic, with α and γ significantly deviating to values of 94.04(1)° and 90.18(1)°, respectively, at 30 K. The result is a diffraction pattern in which the reflections do not perfectly overlap.

The molecular structure of [Fe(bapbpy) (NCS)$_2$] is shown in Figure 4.6. The volume of the iron coordination octahedron is 9.95(1) Å^3, typical of Fe^{II} in the low spin state, as are the Fe – N bond lengths, given in Table 4.1. Selected crystallographic data for the structure in this phase are presented in Table 4.2.

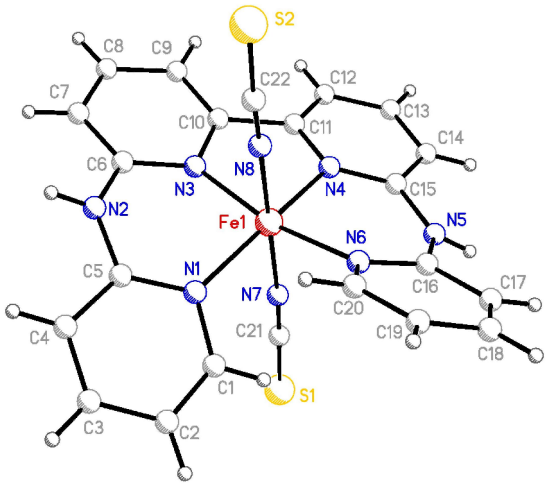

Figure 4.6. Molecular structure of [Fe(bapbpy)(NCS)$_2$] at 30 K

Table 4.1. Iron - Nitrogen bond distances for [Fe(bapbpy)(NCS)$_2$] at 30 K

Bond	Distance (Å)
Fe – N1	2.001(3)
Fe – N3	1.939(4)
Fe – N4	1.948(3)
Fe – N6	1.991(3)
Fe – N7	1.943(6)
Fe – N8	1.966(6)

Table 4.2. Selected crystallographic data for for [Fe(bapbpy)(NCS)$_2$] at 30 K

[Fe(bapbpy)(NCS)$_2$] 30K	
Empirical formula	$C_{22}H_{16}N_8FeS_2$
Formula weight	512.40
Temperature/K	30(2)
Crystal system	Triclinic
Space group	Pī
a/Å	9.466(3)
b/Å	9.494(3)
c/Å	13.476(5)
α/°	94.370(5)
β/°	106.053(7)
γ/°	112.249(7)
Volume/Å^3	1054.6(6)
Z	2
Crystal size/mm^3	0.09 × 0.14 × 0.17
Theta range for data collection	1.61 to 20.28°
Reflections collected	7295
Independent reflections	5306
Data/restraints/parameters	5306/0/100
Goodness-of-fit on F^2	1.111
Final R indexes	R_1 = 0.0658
[I>2σ (I)]	wR_2 = 0.2078
Final R indexes	R_1 = 0.0947
[all data]	wR_2 = 0.2322
Largest diff. peak/hole / e Å^{-3}	0.691/-0.628

4.3.2 Structure at 30 K after laser irradiation – HS* Phase 4

After irradiation of the sample, diffraction from an additional component was observed in the diffraction pattern as shown in Figure 4.7. In accordance with the magnetic measurements, full conversion to the HS* state could not be achieved using these conditions, evidenced by reflections from the new component and the LS twinned phase in the same diffraction pattern.

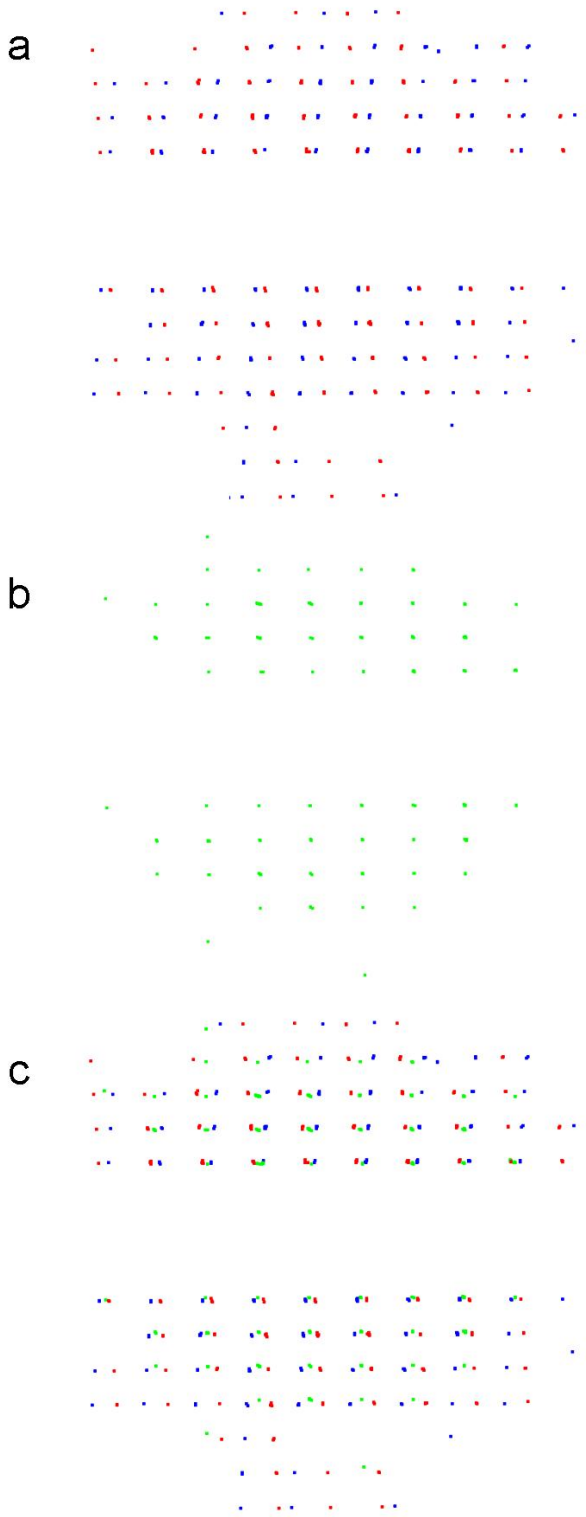

Figure 4.7. Reciprocal lattice of the two twin components of the LS state (a), each component is shown separately in blue and red. Reciprocal lattice of the light-induced meta stable state (b) The total observed lattice is also shown (c)

Reflections from this additional phase were separated from those associated with the twin component using RLATT and indexed using SMART. The cell was comparable to that of the thermal 100% HS phase. The structure was solved in the space group C2/c. Data that overlapped with reflections from the residual LS fraction were omitted, resulting in an incomplete data set, reflected in the relatively poor refinement statistics, as presented in Table 4.3. The poor statistics may also be a result of crystal damage during laser irradiation and the partial phase transition that results.

Table 4.3. Crystal data for at 30 K for [Fe(bapbpy)(NCS)$_2$] after irradiation – Phase 4

[Fe(bapbpy)(NCS)$_2$] 30K + laser irradiation	
Empirical formula	$C_{22}H_{16}N_8FeS_2$
Formula weight	512.40
Temperature/K	30.0
Crystal system	Monoclinic
Space group	C2/c
a/Å	15.905(3)
b/Å	10.819(3)
c/Å	14.130(3)
α/°	90.00
β/°	117.136(13)
γ/°	90.00
Volume/Å^3	2163.7(9)
Z	4
Crystal size/mm^3	0.09 × 0.14 × 0.17
Theta range for data collection	2.37 to 20.47°
Reflections collected	1700
Independent reflections	962
Data/restraints/parameters	962/10/38
Goodness-of-fit on F^2	1.430
Final R indexes [I>2σ (I)]	R_1 = 0.1121 wR_2 = 0.2618
Final R indexes [all data]	R_1 = 0.1608 wR_2 = 0.2742
Largest diff. peak/hole / e Å^{-3}	1.007/-0.905

Refinement was also performed in the spacegroups Cc, C2 and in the primitive triclinic cell setting with the spacegroup Pī. These refinements resulted in significantly worse values of R_1 and wR_2, a high degree of correlation between thermal parameters of related atoms and chemically insensible models. Consequently, the C2/c description of the spacegroup seems the most suitable.

The molecular structure is shown in Figure 4.8. The volume of the iron coordination octahedron is 12.25(4) Å^3, which is slightly lower than the typical value of ~ 13 Å^3 for Fe^{II} compounds in the high spin state.[9] The value for the previously published[10] room temperature HS phase is 12.46 Å^3, indicating that even when in the fully high spin phase, this molecule has a relatively small octahedral volume. The 30 K value after irradiation is much closer to a high spin value, showing that this component of the crystal is in the HS* phase. The Fe-N bond lengths for this phase are given in Table 4.4, along with those for the published high temperature HS phase.

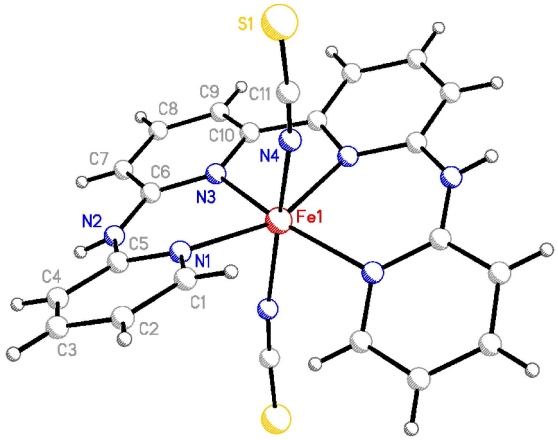

Figure 4.8. Molecular structure of the title compund in the HS* state after partial light induced excitation at 30 K. Only unique atoms are labelled

Table 4.4. Iron - nitrogen bond distances for the HS* Phase of [Fe(bapbpy)(NCS)$_2$] at 30 K after laser irradiation (30 K +i) and the HS phase collected at 295 K[3]

	Distance (Å)	
Bond	**30 K +i**	**295 K**
Fe – N1	2.133(2)	2.146
Fe – N3	2.132(7)	2.135
Fe – N4	2.13(2)	2.148

4.4 Conclusions and Perspectives

This compound shows LIESST behaviour at low temperatures. Full conversion of the LS state to the HS* state was not achieved after irradiation of the single crystal sample for 30 mins, which is in agreement with findings from the published magnetic investigation. The incomplete nature of this excitation leads to a diffraction pattern that is not trivial to interpret. It may be worth investigating whether full conversion to the HS* state is possible by irradiating the crystal for a longer period and/or with a more powerful laser or a laser of different wavelength. It should however be noted that irradiation of a polycrystalline sample of the complex for 2 hours with a 10 mW Ar^+ laser resulted in reaching the photostationary limit of the magnetisation without full conversion.[2]

If full conversion could be achieved, the data quality used for structural determination and refinement should be improved by removing overlapping reflections originating from the residual LS component. This would allow a full structural investigation of the stepped relaxation of the HS* state observed by magnetic measurements.

It is not uncommon for the LIESST effect to result in only partial conversion of the crystal to the meta-stable high spin state.[11,12,13] Previous reports have attributed the incomplete nature of the photo-excitation to an efficient tunnelling relaxation process from the HS* to the LS state, even at low temperatures.[13]

If the fully HS* state in [Fe(bapbpy)(NCS)$_2$] is not accessible via the LIESST effect it would be interesting to investigate the reasons why. Kinetic studies of the relaxation process from the HS* to LS state would help to establish how efficient the tunnelling process in this system is.

It would appear from this investigation that the excitation to the HS* state occurs in domains rather than via an intermediate phase such as that observed in the thermal transition. Another possible explanation for the incomplete photo-conversion to the HS* state could be that the laser light cannot penetrate sufficiently into the sample and so only molecules near the surface are exposed to the surface and undergo the LIESST effect. If this were the case one could envisage single crystal diffraction experiments involving crystals with a range of ratios of volume to surface area. Assuming the proportion of the crystal converted to the HS* state could be determined from

diffraction data then the effect of crystal shape on conversion efficiency may well be of significant interest. However, extreme caution should be exercised before relying upon this assumption; relative intensities of 'equivalent' reflections from each fraction could not be directly compared as the HS* fraction and residual LS fraction are not structurally identical. Additionally, the crystallinity of the HS* component may be significantly different from that of the residual LS component after exposure to laser irradiation and the resulting phase transition. Intensity of Bragg reflections may be thus reduced without revealing any significant information as to the relative proportion of each component. While a study to investigate the ratio of the two components could be undertaken using diffraction methods, it seems unlikely that errors in any values obtained could be reliably estimated and hence the validity of such a study should be carefully examined in advance.

Finally, this study has confirmed the suggestion made in the previous report[2] that the HS* phase is likely to be isostructural with the themal HS Phase 1, and not the mixed spin Phase 2.

---

[1] S. Bonnet, M. A. Siegler, J. Sánchez Costa, G. Molnár, A. Bousseksou, A. L. Spek, P. Gamez and J. Reedijk, *Chem. Commun.*, 2008, 5619

[2] S. Bonnet, G. Molnár, J. Sánchez Costa, M. A. Siegler, A. L. Spek, A. Bousseksou, W.-T. Fu, P. Gamez, and J. Reedijk, *Chem. Mater.*, 2009, **21**, 1123

[3] S. Bonnet, M. A. Siegler, J. Sánchez Costa, G. Molnár, A. Bousseksou, A. L. Spek, P. Gamez and J. Reedijk, *Chem. Commun.*, 2008, 5619 – Electronic Supplementary Material

[4] A. E. Goeta, L. K. Thompson, C. L. Sheppard, S. S. Tandon, C. W. Lehmann, J. Cosier, C. Webster and J. A. K. Howard, *Acta Cryst., Sect. C*, 1999, **55**, 1243

[5] *SMART-NT, Data Collection Software, version 6.1,* Bruker Analytical X-ray Instruments Inc., Madison, WI, USA, 2000

[6] *SAINT-NT, Data Reduction Software, version 6.1*, Bruker Analytical X-ray Instruments Inc., Madison, WI, USA, 2000

[7] G. M. Sheldrick, *Acta Cryst.*, 2008, **A64**, 112

[8] O. V. Dolomanov, L. J. Bourhis, R. J. Gildea, J. A. K. Howard, H. Puschmann, *J. Appl. Cryst.*, 2009, **42**, 339

[9] P. Guionneau, M. Marchivie, G. Bravic, J.-F. Létard and D. Chasseau, *Top. Curr. Chem.*, 2004, **234**, 97

[10] Value for Octahedral volume of the published structure calculated from the cif found in the electronic supplementary material, using Olex2

[11] J.-F. Létard, P. Guionneau, L. Rebardel, J. A. K. Howard, A. E. Goeta, D. Chasseau and O. Kahn, *Inorg. Chem.*, 1998, **37**, 4432

[12] J. Jeftić, M. Matsarski, A. Hauser, A. Goujon, E. Codjovi, J. Linarès and F. Varret, *Polyhedron*, 2001, **20**, 1599

[13] V. Mishra, H. Mishra, R. Mukherjee, E. Codjovi, J. Linarés, J.-F. Létard, C. Desplanches, C. Baldé, C. Enachescu and F. Varret, *Dalton Trans.*, 2009, 7462

5 Stepped Spin Crossover in $[Fe^{III}(L1)]ClO_4$

5.1 Spin Crossover in Fe^{III} systems

Fe^{III} compounds have long been known to show spin crossover (SCO) properties; indeed it was in these systems that the temperature dependence of magnetic properties was first observed.[1] While the process is broadly similar to that observed for Fe^{II}, there are a number of marked differences including the coordination environments that can induce SCO, available spin states and the potential for cooperativity.

5.1.1 Coordination Environment

Fe^{III} systems that undergo thermally-induced spin transitions show a much broader variety of coordination environments than Fe^{II} SCO systems.[2] Unlike for Fe^{II} complexes, both 5- and 6-coordinate Fe^{III} systems can show spin crossover properties. A multitude of ligand systems, including those with chalcogen donor atoms have been shown to induce Spin Crossover in Fe^{III}, the most common having FeS_6, $FeSe_6$, FeS_3O_3 and FeS_3Se_3 coordination spheres, although several others are also known. Another widely studied ligand system is that of multidentate Schiff bases, where the coordination environment is usually provided by four nitrogen and two oxygen donor atoms.[3,4,5,6]

Many Schiff base ligands are known to induce spin crossover in Fe^{III} complexes, most of which have a N_4O_2 coordination environment.[2] There are several examples containing tridentate (N_2O – donating) Schiff bases, the vast majority of which have the general formula $[Fe^{III}(Ligand^{-})_2](anion^{-})\bullet solvent$. The choice of both anion[7] and solvent[8] can have a significant impact on the spin crossover process in these species.[2] Examples of tetra, penta and hexadentate Schiff base ligands in Fe^{III} SCO complexes are also known, although these are somewhat less common than tridentate species.[1,2]

Structural studies of these Fe^{III} Schiff base materials with N_4O_2 coordination environments have shown that the variation in the bond length depends on the ligating atom. Fe – N_{amine} bonds show the largest differences between the HS and LS states, followed by Fe – N_{imine} bonds. Fe – O bonds show the smallest change on SCO, typically showing a difference of only 0.002 – 0.004 Å between the HS and LS states.[1,2]

Hexadentate Schiff bases have been classified in terms of the number of carbon atoms (k, m, n, Figure 5.1) between nitrogen atoms of a linear tetramine.[1,3] Variation of this chain length alters the size of the chelate ring formed through the nitrogen donor atoms to the iron, which has been shown to affect the spin state of the complex.[9] Schiff bases with (3,3,3), (3,2,3), (2,3,2), (2,2,2) [2] and (2,3,2)[3] have been investigated as possible ligands to induce SCO in Fe^{III} systems.

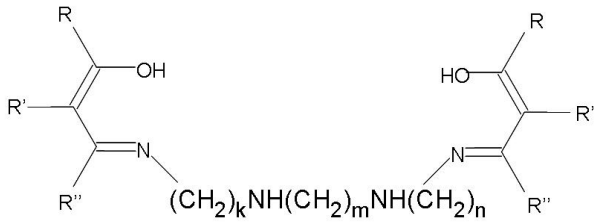

Figure 5.1. Hexadentate Schiff base, where R indicates alkyl groups and k, m and n are numbers used to classify the ligand

The L – Fe – L bond angles in Fe^{III} Schiff base materials lie within the range 75° – 105° when in the HS state, and 84° – 95° when in the LS state. The geometry is much closer to octahedral in the low spin state than in the high spin state, both in terms of bond angle and bond length.[2]

5.1.2 Spin States

Unlike in Fe^{II} systems where only HS and LS states are known, Fe^{III} complexes have been characterised in the high spin (S = 5/2) state, the low spin (S = 1/2) state and an intermediate (S = 3/2) state.[1,2] The S = 5/2 ↔ S = 1/2 spin transition is commonly observed in 6-coordinate molecules in an analogous manner to Fe^{II} systems. Fe^{III} complexes however can also show S = 3/2 ↔ S = 1/2 transitions, which is most common in 5-coordinate species,[10] although this type of transition has once been observed in a 6-coordinate Fe^{III} system.[11]

5.1.3 Cooperativity

Another difference between Fe^{II} and Fe^{III} complexes is that the difference in iron - ligand bond distances ($\Delta(Fe\text{-}L)_{HL}$) between the high spin and low spin states (average ~ 0.18 Å and ~ 0.12 Å respectively).[1,2] There is a significant difference between the behaviour of these systems, resulting from the decreased activation energy (ΔW_{HL})

required to convert between the HS and LS spin states when $\Delta(Fe\text{-}L)_{HL}$ is smaller. This is shown schematically in Figure 5.2.

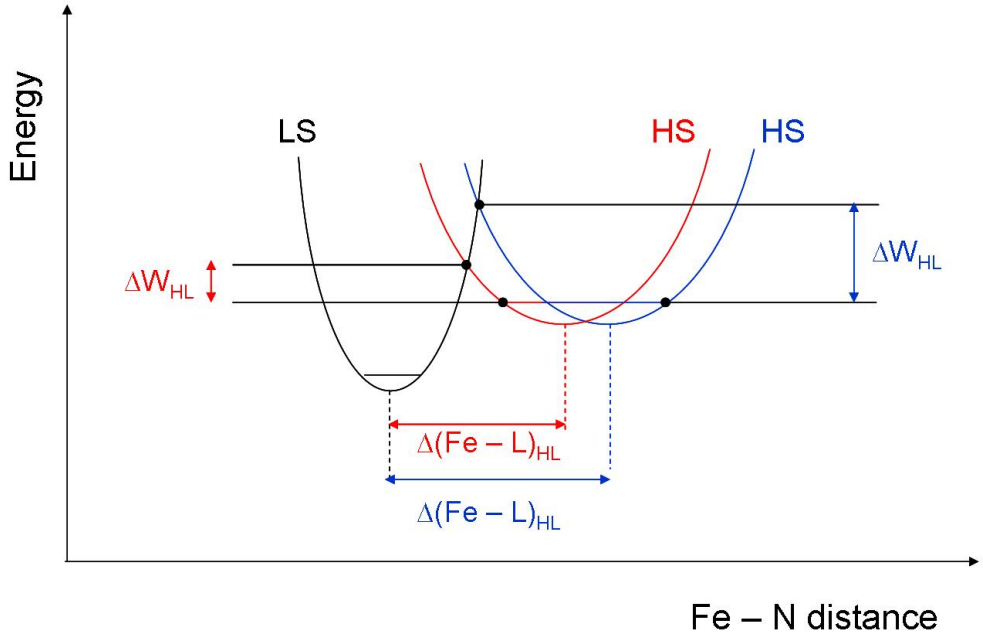

Figure 5.2. The effect of the difference in bond length between the HS and LS states ($\Delta(Fe\text{-}L)_{HL}$) on the activation energy for conversion between HS and LS states (ΔW_{HL}). A larger $\Delta(Fe\text{-}L)_{HL}$ value is shown in blue while a smaller value is shown in red

Interconversion between spin states is easier in ferric systems, often resulting in more gradual transitions than those observed in analogous ferrous complexes. For the same reason, LIESST and strongly cooperative effects are markedly less common in these species.[12] This interconversion can often occur at a rate comparable to or in excess of the Mössbauer timescale (10^{-7} s) leading to broadened signals in the spectrum, and the inability to assign distinct spin states. This potential for rapid interconversion and reduced cooperativity means Fe^{II} systems are often preferred as targets for possible applications which require abrupt transitions and hysteretic behaviour.

Cooperative effects that are observed in the solid state for Fe^{III} SCO systems have been attributed to strong π-π stacking[8] or hydrogen bonding[13] interactions. This has led to a number of Fe^{III} systems that display sharp first order transitions, with ligand systems including thiosemicarbazones[13] and some Schiff base complexes.[14,15] Few examples of stepped SCO are known Fe^{III} complexes.[16]

Two Schiff base complexes of Fe^{III} which do show stepped spin crossover properties are $\{[Fe(mph)_2](ClO_4)(MeOH)_{0.5}(H_2O)_{0.5}\}_2$[17] and $[Fe(salpm)_2]ClO_4 \bullet 0.5EtOH$.[18] Both of these systems have two mixed-donor tridentate Schiff base ligands, which coordinate to the iron centre in an approximately perpendicular fashion. These complexes and their magnetic behaviour as a function of temperature are shown in Figure 5.3. $\{[Fe(mph)_2](ClO_4)(MeOH)_{0.5}(H_2O)_{0.5}\}_2$ shows significantly more abrupt transitions than $[Fe(salpm)_2]ClO_4 \bullet 0.5EtOH$, attributed to the increased degree of cooperativity, which results from the strong hydrogen bonding network observed throughout the lattice of the former. Indeed this Schiff base ligand was specifically designed to include both hydrogen bond donors and acceptors with the aim of increasing cooperative effects.

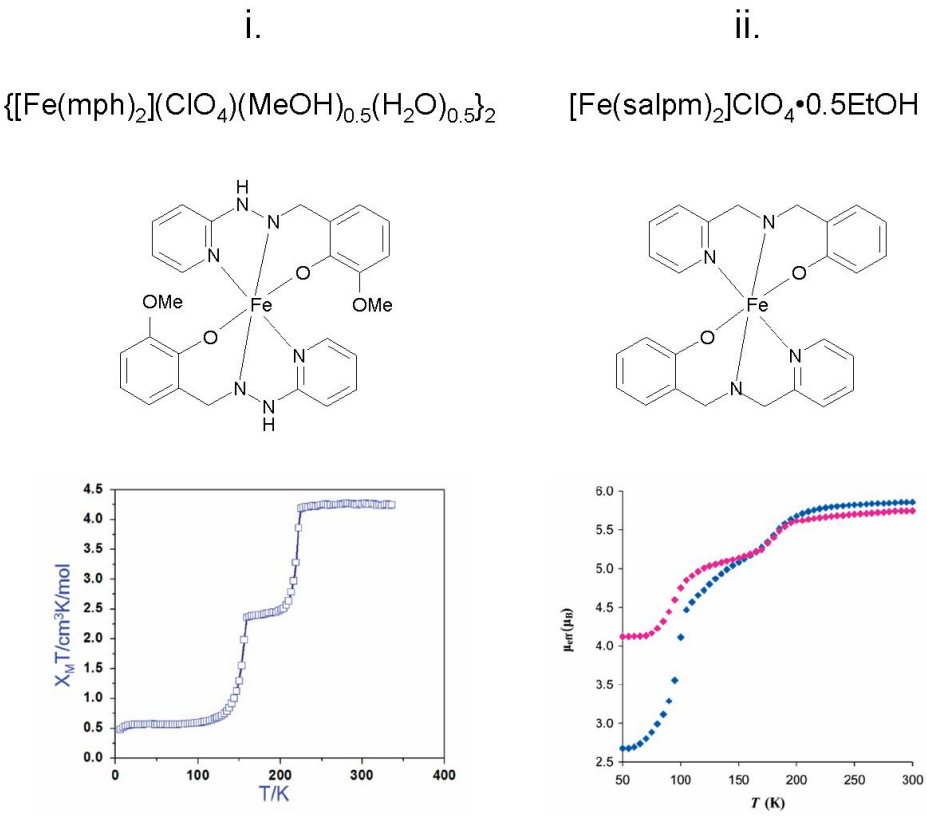

Figure 5.3. Complex cations and magnetic behaviour of i. $\{[Fe(mph)_2](ClO_4)(MeOH)_{0.5}(H_2O)_{0.5}\}_2$, and ii. $[Fe(salpm)_2]ClO_4 \bullet 0.5EtOH$. Magnetism graphs for i.* and ii. have been taken directly from the literature.[17,18] In ii. the pink points are from a powdered sample and the blue points are from single crystal measurements**

*** Adapted with permission from Inorg. Chem., 2009, 48, 5, 2128. J. Tang, J. Sánchez Costa, S. Smulders, G. Molnár, A. Bousseksou, S. J. Teat, Y. Li, G. A. van Albada, P. Gamez and J. Reedijk.. Copyright 2007 American Chemical Society **Adapted with permission from Inorg. Chem., 2007, 46, 23, 9558. M. S. Shongwe, B. A. Al-Rashdi, H. Adams, M. J. Morris, M. Mikuriya, and G. R. Hearne. Copyright 2007 American Chemical Society**

In the case of $[Fe(salpm)_2]ClO_4 \bullet 0.5EtOH$ there are two crystallographically inequivalent Fe^{III} sites even in the 100% HS state, above the temperature of the spin transitions. One of the sites undergoes a complete spin transition (between 200 K and 150 K), followed by the other site (between 100 K and 65 K). The presence of an intermediate phase in which HS and LS sites are clearly ordered was confirmed using crystallographic techniques at 100 K and may be attributed to differences in the intermolecular interactions and energy of these independent sites. By contrast, $\{[Fe(mph)_2](ClO_4)(MeOH)_{0.5}(H_2O)_{0.5}\}_2$ was shown by Mössbauer spectroscopy to have an intermediate phase consisting of HS and LS sites distributed randomly throughout the lattice, despite there being two crystallographically independent Fe^{III} sites within the asymmetric unit at a temperature expected to be within the plateau region of the spin transition. Variable temperature diffraction studies were not possible in this case and hence this unusual behaviour could not be fully structurally characterised. The stepped behaviour of the spin transition for this species was attributed to the presence of the perchlorate anion, as studies of the complex cation with other counterions (namely PF_6 and BPh_4) showed very different (non-stepped) SCO properties.

An additional feature of the investigation into the $[Fe(salpm)_2]ClO_4 \bullet 0.5EtOH$ sample is the difference in magnetic behaviour observed between powdered and single crystal samples. It has been previously noted[19] that powdered samples have a higher residual high spin component at low temperatures than single crystal samples; however this case shows the largest difference between the two.

5.2 $[Fe^{III}(L1)]ClO_4$

Crystalline samples of $[Fe^{III}(L1)]ClO_4$ (where L1 is the hexadentate Schiff base N,N'-bis(2-(3,5-Dimethoxysalicylideneamino)ethyl)-1,3-diaminopropane), shown in Figure 5.4, were prepared by the group of Dr. Grace Morgan at University College Dublin. $[Fe^{III}(L1)]ClO_4$ is chemically similar to a series of 2,3,2 Schiff base complexes investigated by Hayami *et. al.*[3], which vary in the type and position of alkyl and methoxy substituents on the phenyl ring and methylidyne carbon atoms. None of the 2,3,2 complexes previously investigated has been found to show spin crossover properties. Previous crystallographic studies have been performed by Dr. Helge Mueller-Bunz at University College Dublin, forming the basis for this investigation.

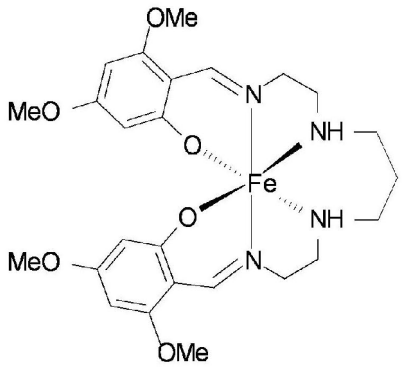

Figure 5.4. $[Fe^{III}(L1)]ClO_4$ (where L1 = N,N'-bis(2-(3,5-Dimethoxysalicylideneamino)ethyl)-1,3-diaminopropane)

Magnetic studies were performed at the Institut de Chimie de la Matière Condensèe de Bordeaux (ICMCB), by Jean-François Létard and co-workers, and revealed a 2 step thermally induced spin transition, as shown in Figure 5.5. The first step occurs at ~187 K and corresponds to a transition from all iron centres being in the HS state above this temperature, to a mixed spin state in which one third of the iron sites have become low spin. The second step occurs at ~92 K, corresponding to a further third of the iron sites becoming LS below this temperature. The final third of the molecules remain in the LS state down to 20 K, after which zero-field splitting effects occur. There is a slight hysteresis observed in this second step, with the temperature of the transition on warming being ~107 K.

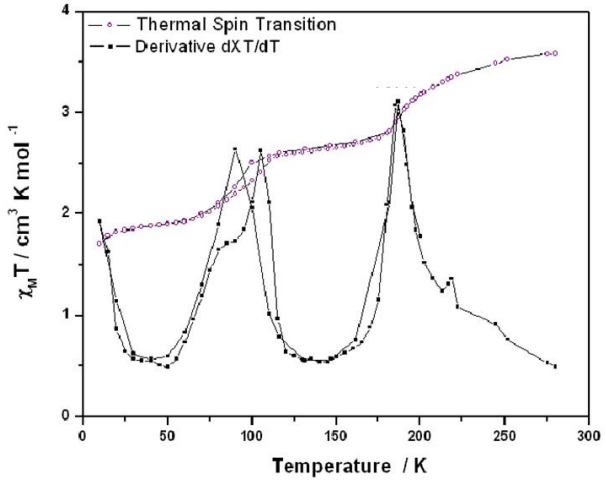

Figure 5.5. Magnetic behaviour of $[Fe^{III}(L1)]ClO_4$ as a function of temperature[20]

As discussed in section 5.1.3, it is rare for Fe^{III} systems to display strong cooperative effects; both the stepped nature of the spin transition and hysteretic behaviour appeared unusual in this respect and hence a full structural investigation of this system was undertaken. Single crystal and powder X-ray diffraction techniques were used to investigate the nature of the phase transition. The investigation aimed to determine whether the two mixed spin state phases were structurally ordered and shed light on the origin of the cooperative effects observed.

5.3 Experimental

Single crystal X-ray diffraction experiments were carried out on a SMART 3-circle diffractometer with a 1 K CCD area detector, using graphite-monochromated Mo-Kα rariation (λ = 0.71073 Å) and a Cryostream (Oxford Cryosystems) open-flow N_2 gas cryostat. A series of narrow ω-scans (0.3°) was performed at several φ-settings in such a way as to cover a sphere of data to a maximum resolution of 0.75 Å. Cell parameters were determined and refined using SMART software[21], and raw frame data were integrated with the SAINT program.[22] The structures were solved by direct methods using SHELXS,[23] and refined by full-matrix least-squares on F^2 using SHELXL-97[23] and the graphical user interface Olex2.[24] The temperature was controlled using an Oxford Cryosystems Helix.[25]

Full data collections were performed at 200 K and 160 K. Unit cell parameters were collected at regular intervals between 275 K and 130 K. Several attempts were made to collect single crystal data down to 30 K, but the crystal disintegrated during further cooling from 115 K, to such an extent that the pattern could not be indexed.

Variable temperature powder X-ray diffraction data were collected using a Bruker AXS D8 Advance diffractometer and temperature was controlled with an Oxford Cryosystems PheniX helium cryostat. The sample was cooled at a rate of 12 K per hour from 290 K to 20 K while collecting data in the 2θ range 5° - 35° in 0.05° steps, using a counting time of 0.3 s per step. A further series of 3 data collections were performed at 20 K, between 5° and 80° in 2θ and summed.

5.4 Results

5.4.1 Structure at 200 K – Phase 1

The molecular structure of the [Fe^{III}(L1)]ClO$_4$ at 200 K is shown in Figure 5.6. The space group is C2/c and the asymmetric unit consists of half a complex cation and half a perchlorate anion. Fe1 and C1 reside on a 2-fold rotation axis, as does the chlorine atom of the perchlorate (Cl1). The iron – ligand bond distances and angles are given in Table 5.1, along with average values for the analogous 2,3,2 Fe^{III} Schiff base complexes published previously. It is clear from inspection of bond lengths and the range of bond angles that the title compound is in the HS state at 200 K, which in agreement with the magnetic data. Selected crystallographic data for Phase 1 one is shown in Table 5.3.

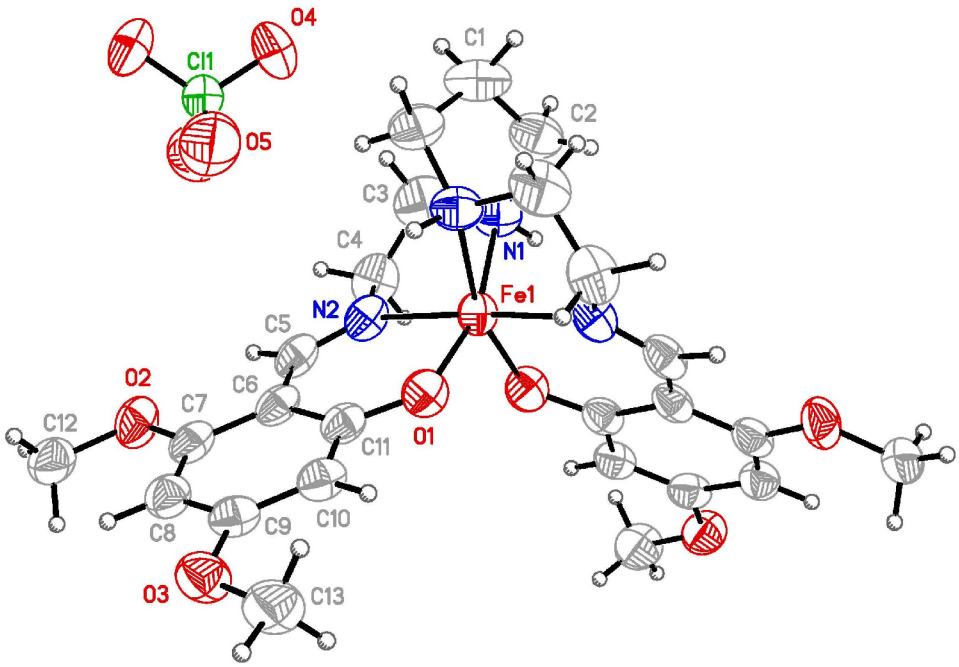

Figure 5.6. Molecular structure of the title compound at 200 K showing the numbering scheme of the crystallographically-unique atoms. Atomic displacement parameters are drawn at 50% probability

Table 5.1. Iron - ligand bond distances for $[Fe^{III}(L1)]ClO_4$ in Phase 1 and average values from the literature[2, 3] for similar Fe^{III} 2,3,2 Schiff base complexes in the HS and LS states

Bond Lengths (Å)	$[Fe^{III}(L1)]ClO_4$	Average HS	Average LS
Fe – N_{amine}	2.144(3)	2.188(29)	2.014(6)
Fe – N_{imine}	2.045(3)	2.126(7)	1.945(21)
Fe – O	1.906(2)	1.906(22)	1.881(13)
Range of Bond Angles (°)	79.2(1) – 103.5(1)	75 – 105	84 – 95

There is no evidence of either H-bonding or π-π stacking interactions in the structure at 200 K. An intricate network of short contacts (less than the sum of the Van der Waals radii) is present throughout the structure. The complex cations pack in chains along the [10-1] direction, with alternate molecules rotated by 180° as shown in Figure 5.7. These chains build up into a three dimensional network through further non-covalent interactions, as shown in Figure 5.8.

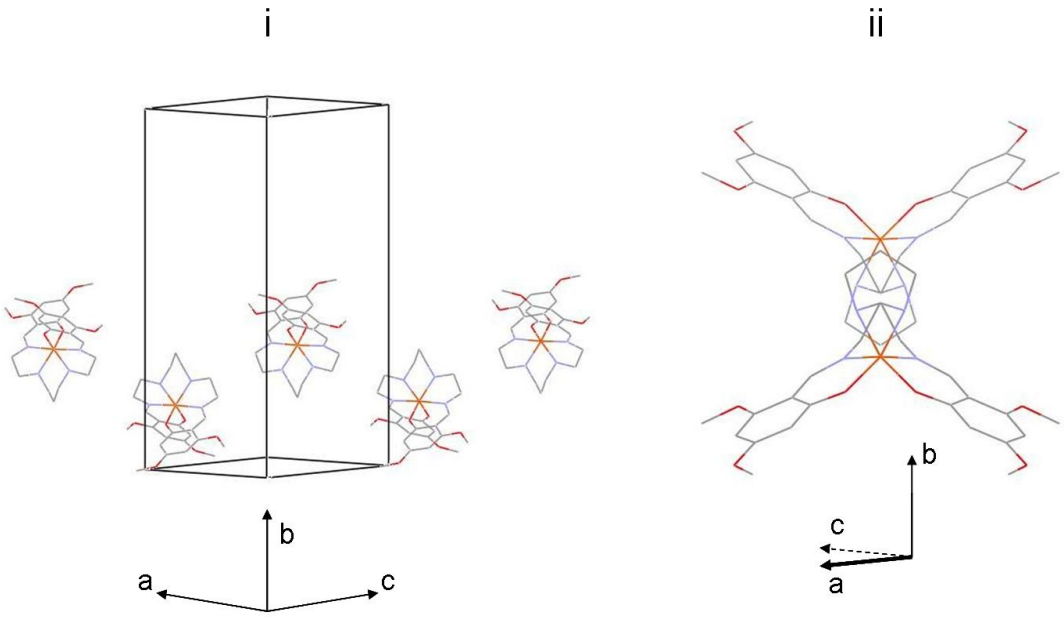

Figure 5.7. View of the chains formed in the title compound viewed i) perpendicular to the (101) plane and ii) down the [10-1] direction

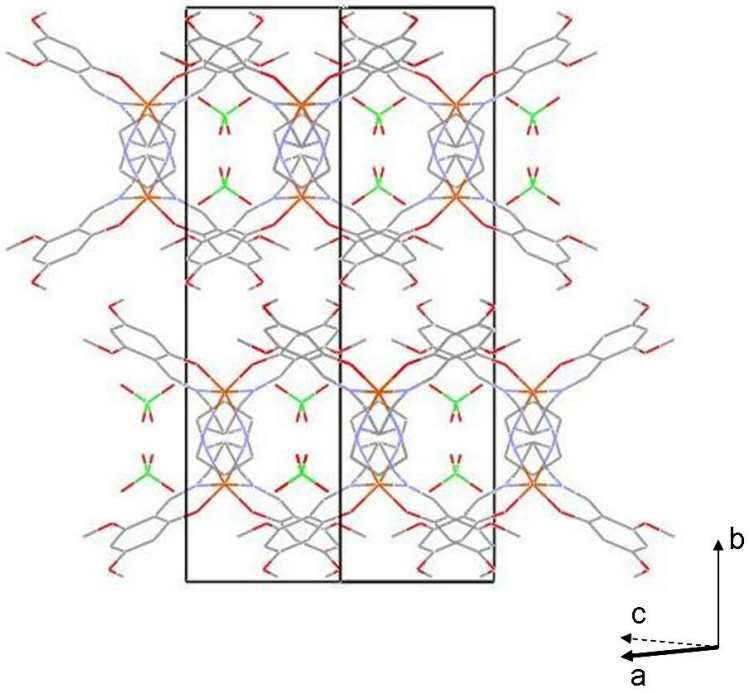

Figure 5.8. Molecular packing in [Fe(L1)]ClO4, viewed down the [10-1] direction

5.4.2 Structure at 160 K – Phase 2

Upon cooling through the temperature associated with the first spin transition, a crystallographic phase transition occurs. The space group of this second phase is still C2/c, but the cell volume increases by a factor of 3 (ignoring thermal contraction and reduction in cell volume resulting from the changes associated with the Fe centre on SCO). The orientation of the cell changes with respect to the original Phase 1 lattice, as shown mathematically in Matrix 5.1.

$$\begin{pmatrix} 1 & 0 & 2 \\ 0 & -1 & 0 \\ 1 & 0 & -1 \end{pmatrix}$$

Matrix 5.1. Transformation matrix relating the unit cell in Phase 1 to that in Phase 2

The asymmetric unit increases to one and a half complex cations and one and a half perchlorate anions; the structure is shown in Figure 5.9. Selected crystallographic data for Phase 2 are shown in Table 5.3, along with those of Phase 1.

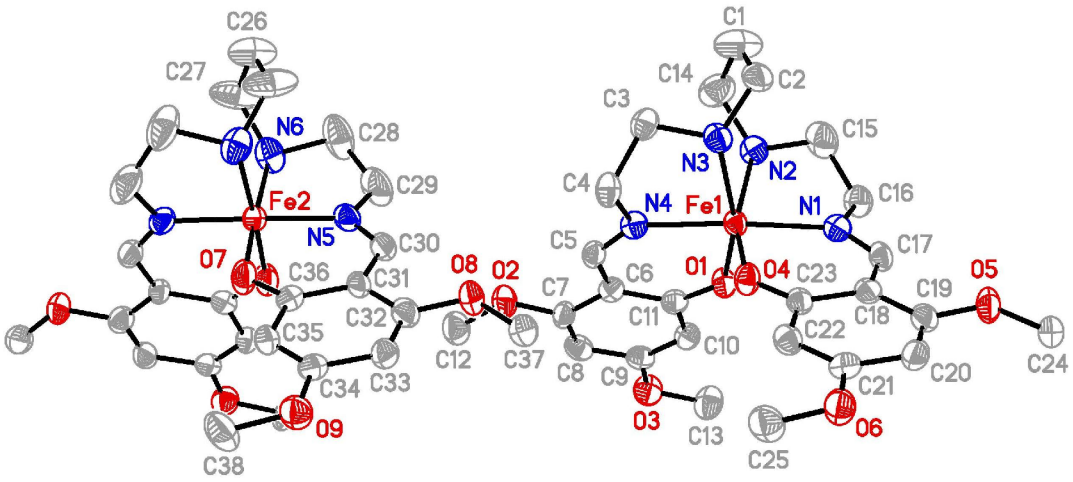

Figure 5.9. Structure of the title compound at 160 K - Phase 2. Atomic displacement parameters are shown at 50% probability. Hydrogen atoms and perchlorate counter ions have been removed for clarity. Only crystallographically-unique atoms are labelled

Inspection of the bond lengths and angles displayed in Table 5.2 reveals that Fe1 (100% occupancy) is in the HS state, and Fe2 (50% occupancy) is in the LS state, resulting in a ratio of 2:1 HS:LS. This is in agreement with the expected ratio from the magnetic data.

Table 5.2. Iron - ligand bond distances for $[Fe^{III}(L1)]ClO_4$ in Phase 1 and average values from the literature[2, 3] for similar Fe^{III} 2,3,2 Schiff base complexes in the HS and LS states

Bond Lengths (Å)	Fe1	Fe2	Average HS	Average LS
Fe – N_{amine}	2.185(4) 2.192(4)	2.002(4)	2.188(29)	2.014(6)
Fe – N_{imine}	2.077(4) 2.088(4)	1.924(4)	2.126(7)	1.945(21)
Fe – O	1.915(3) 1.918(3)	1.871(3)	1.906(22)	1.881(13)
Range of Bond Angles (°)	78.0(1) – 104.6(1)	83.8(1) – 96.8(1)	75 – 105	84 – 95

Moreover, the spin states are localised on specific iron centres that are no longer equivalent, as a result of the crystallographic phase transition, revealing a mixed spin intermediate phase that displays long range order of HS-HS-LS units. The [10-1] direction in Phase 1 is equivalent to the direction of the c-axis in Phase 2 as a result of

the change in cell definition that occurs during the phase transition. The extended structure viewed down the c-axis (Figure 5.10) shows the chains that were previously described as extending infinitely in this direction. One third of these chains now consist entirely of low spin molecules, as shown schematically in Figure 5.11.

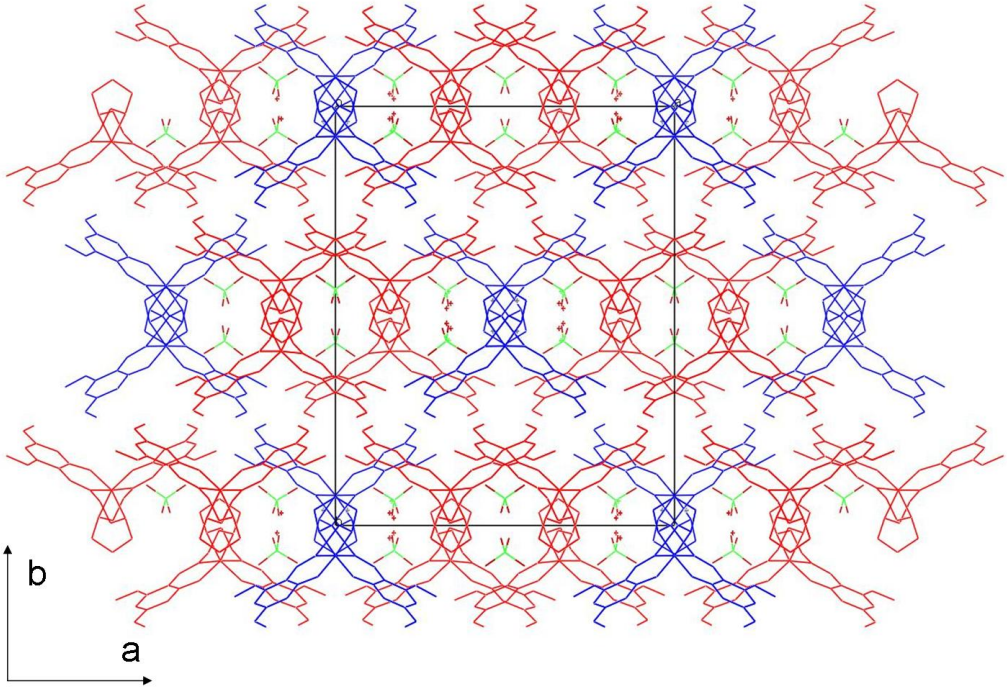

Figure 5.10. Ordering of HS and LS states in the mixed spin Phase 2, viewed down the c axis. Red indicates high spin molecules and blue indicates low spin molecules

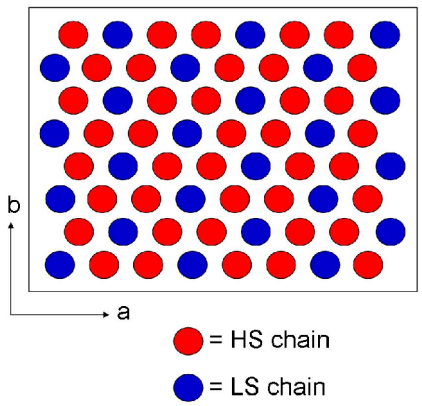

Figure 5.11. Schematic representation of the distribution of HS and LS chains, which extend infinitely along the c-axis

Table 5.3. Selected crystallographic parameters for $[Fe^{III}(L1)]ClO_4$ in Phases 1 and 2

	Phase 1	**Phase 2**
Empirical Formula	$C_{25}H_{36}N_4FeClO_{10}$	
Temperature/K	200	160
Crystal system	Monoclinic	
Space group	C2/c	
a/Å	9.9677(4)	23.1785(6)
b/Å	24.8597(11)	24.7163(9)
c/Å	11.6330(6)	16.9116(6)
β/°	103.109(1)	120.487(2)
Volume/$Å^3$	2807.5(2)	8348.9(5)
Z′/Z	½ / 4	1½ / 6
ρ_{calc}mg/mm^3	1.519	1.532
μ/mm^{-1}	0.695	0.702
Crystal size/mm^3	0.21 × 0.2 × 0.16	0.21 × 0.2 × 0.16
Theta range for data collection	2.25 to 25.07°	1.31 to 25.03°
Reflections collected	12658	52322
Independent reflections	2483 R_{int} = 0.0591	7382 R_{int} = 0.0994
Data/restraints/parameters	2483/0/189	7382/29/572
Goodness-of-fit on F^2	1.020	1.313
Final R indexes [I>2σ (I)]	R_1 = 0.0458 wR_2 = 0.1119	R_1 = 0.0569 wR_2 = 0.1433
Final R indexes [all data]	R_1 = 0.0700 wR_2 = 0.1277	R_1 = 0.1125 wR_2 = 0.1722
Largest diff. peak/hole / e $Å^{-3}$	0.451/-0.451	0.909/-1.213

This ordering of a mixed spin (MS) phase is similar to that observed for another mononuclear stepped spin crossover species, $[Fe(bapbpy)(NCS)_2]$, studied by S. Bonnet and co-workers[26, 27] and described in Chapter 4. This compound shows a 2-step spin transition, from 100% HS → MS phase (⅓ HS, ⅔ LS) → 100 % LS. In this system an analogous phase transition to that observed in $[Fe^{III}(L1)]ClO_4$ occurs from C2/c (Z′ = 0.5 HS) to a cell with three times the volume, also in C2/c (Z′ = 1 LS + 0.5 HS). The third phase is also structurally characterised for $[Fe(bapbpy)(NCS)_2]$, with the space group Pī (Z′ = 1 LS), although it was reported in the unconventional Cī setting to allow

direct comparison with the previous phases. This is an example of a system showing a stepped transition with an ordered MS intermediate phase, in which both spin transitions correspond to a crystallographic phase transition.

A few other examples of MS state intermediate phases have been observed for mononuclear compounds, although for the most part these either do not show crystallographic ordering of the spin states,[28, 29] or display multiple crystallographically independent sites above the transition temperature.[30] An exception is $[Fe(2\text{-}pic)_3]Cl_2 \bullet EtOH$ which shows a HS → ½ HS + ½ LS → LS transition with an ordered MS intermediate phase.[31] In this case, as in that of $[Fe(bapbpy)(NCS)_2]$, each partial spin transition is accompanied by a crystallographic phase transition. In contrast to the $[Fe(bapbpy)(NCS)_2]$ case, the fully HS and fully LS phases of $[Fe(2\text{-}pic)_3]Cl_2 \cdot EtOH$ are isostructural, with the MS phase having a cell with twice the volume.

5.4.3 Variable Temperature Powder Diffraction – Phase 3

Due to disintegration of the single crystal during the second transition, variable temperature powder diffraction experiments were undertaken to investigate the evolution of structural features *in situ* and to elucidate the structure of the system at temperatures below the second transition (Phase 3). Figure 5.12 shows representative scans of the diffraction pattern recorded for each phase.

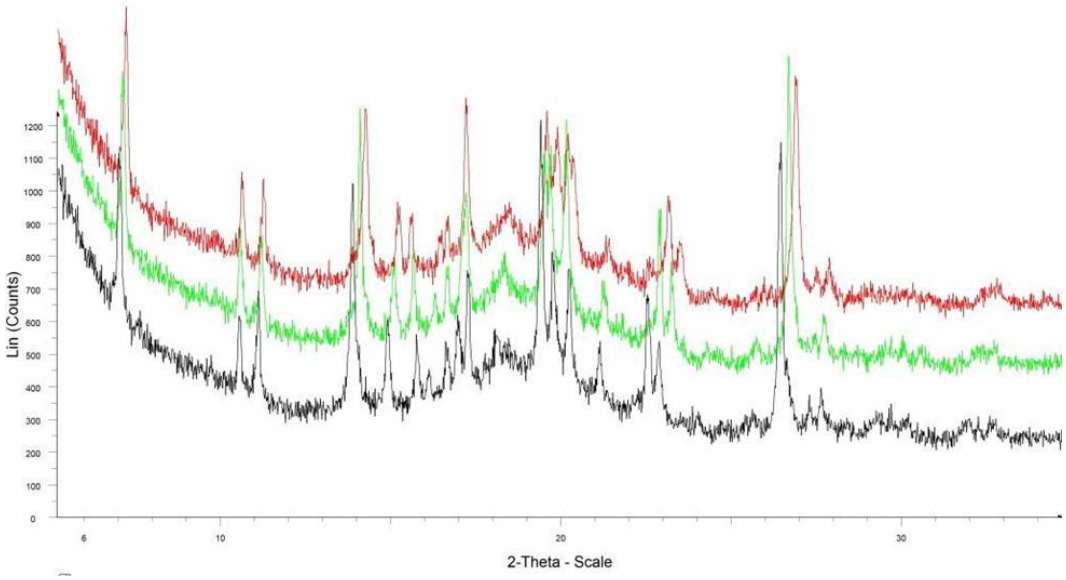

Figure 5.12. Representative scans of the diffraction patterns observed for each phase. Phase 1 (290 K) is shown in black, Phase 2 (140 K) is shown in green, and Phase 3 (20 K) is shown in red

Close examination reveals differences between the patterns that are greater than pure thermal contraction. This becomes more obvious on inspection of the thermodiffractogram shown in Figure 5.13. This close-up of the diffraction patterns between 19° and 24.5° in 2θ reveals two obvious discontinuities in the variation of the position of the Bragg peaks with temperature.

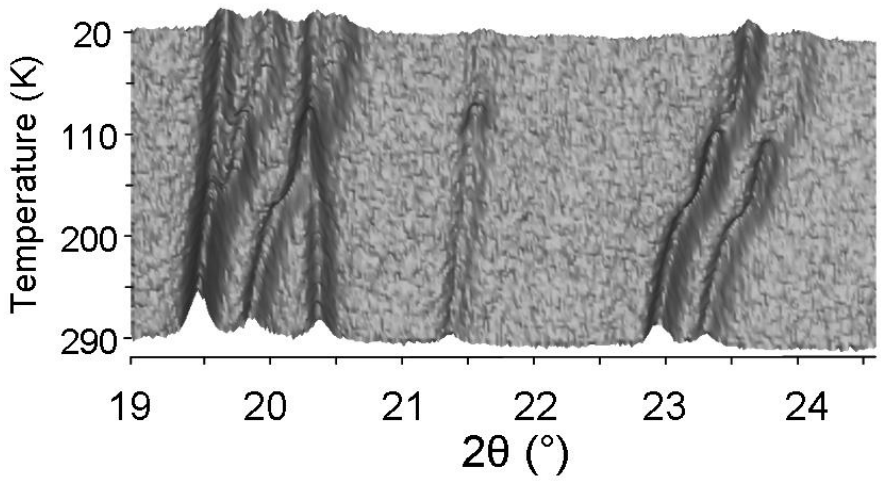

Figure 5.13. Thermodiffractogram between 19° and 24.5° in 2θ recorded while ramping in temperature between 290 and 20 K

The disintegration of the crystal and the second discontinuity in both the magnetic data and the diffraction pattern indicate a structural rearrangement of a similar or greater magnitude to the first. As no single crystal data could be collected, a further powder diffraction pattern was collected with the aim of solving and refining the structure at temperatures below the second transition, *i.e.* in 'Phase 3'. Three scans were collected and summed in an attempt to maximise the signal to noise ratio. The result of the summation is shown in Figure 5.14.

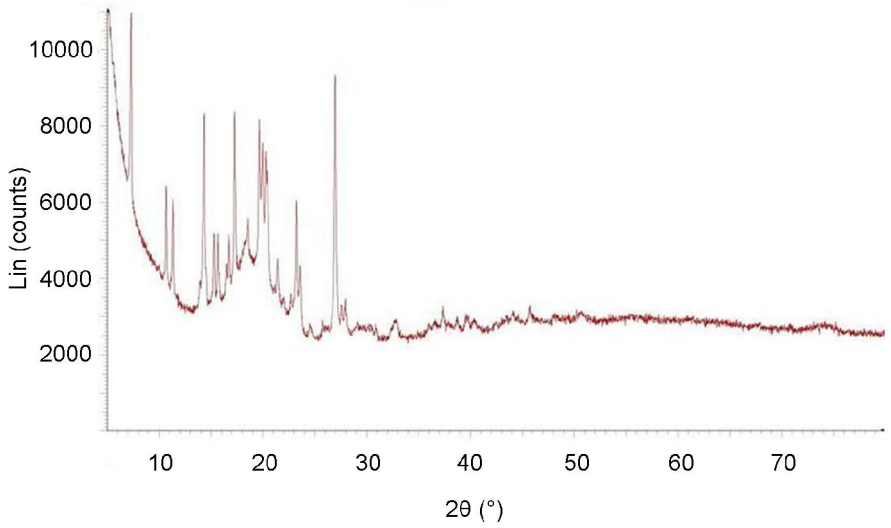

Figure 5.14. Powder diffraction pattern for the title compound at 20 K

These powder data were not of suitable quality for indexing, nor for a full structure refinement using the models obtained from single crystal diffraction studies of Phases 1 and 2.

With the help of Dr. Ivana Evans at Durham University, the models obtained from single crystal data *were* used to fit the observed powder patterns in an attempt to refine the unit cell parameters at each temperature. This was then used to determine the relative change in the volume of the unit cell upon cooling – a value which is intrinsically linked to the structural changes observed upon SCO. The starting structural model obtained from single crystal data of Phase 1 was replaced by that of Phase 2 for data collected at 180 K and below. The only structural parameters refined were the cell parameters and an overall isotropic temperature factor. The other parameters refined were sample displacement, eighteen background terms and five

peak shape function terms. Figure 5.15 shows the evolution of the unit cell volume as a function of temperature derived from powder diffraction data, as well as that from single crystal data within the accessible temperature range for comparison. The volume was normalised relative to the cell in Phase 1 so as to allow direct comparison between phases.

There appears to be a slight disparity between the powder and single crystal measurements for the volume of the unit cell in Phase 2. The volume is higher for the powder sample than single crystal, which may be interpreted as a higher proportion of high spin molecules after the first spin transition. Grinding of samples has been previously shown to affect the temperature-dependent properties of structure and magnetism of other SCO systems[18,19] and results in a higher residual HS fraction below the spin transition temperature. It should be noted that the magnetic data were collected on powdered (ground single crystal) samples. As such, powder data are more likely to reflect the magnetic behaviour displayed in Figure 5.5 than the single crystal data.

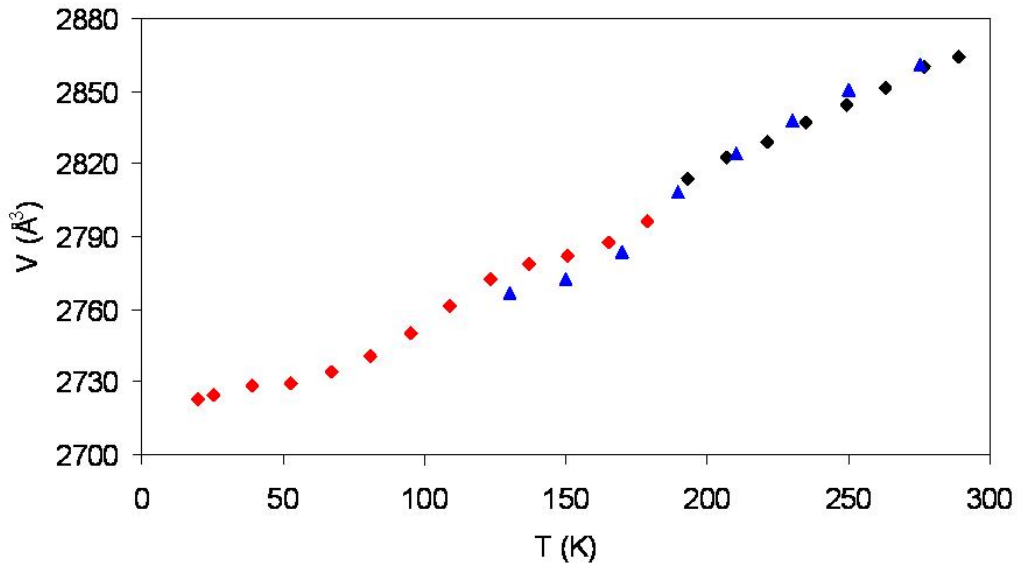

Figure 5.15. Unit cell volume as a function of temperature. Black indicates values obtained from powder data where single crystal data from Phase 1 were used as a starting point. Red indicates values obtained from powder data where single crystal data from Phase 2 were used as a starting point. Blue points are values from single crystal data. All values are normalised relative to the Phase 1 cell and errors are contained within the points

It is clear that the second discontinuity in the position of the Bragg reflections is matched by a concomitant discontinuity in the volume of the unit cell as a function of temperature. Such a reduction in cell volume reflects the change in the volume of the coordination sphere at the iron centre on SCO, and confirms the presence of a second partial spin transition at this temperature.

5.5 Conclusions and Perspectives

The first step of a two-step spin transition in $[Fe^{III}(L1)]ClO_4$ has been structurally characterised both above and below the transition temperature. The transition, which corresponds to one third of the Fe^{III} centres becoming low spin, is accompanied by a structural phase transition, increasing the number of unique molecules by a factor of 3. The intermediate phase (Phase 2) has an ordered distribution of HS and LS states throughout the lattice, which represents one of only a few known systems to show this behaviour and is a first for an Fe^{III} complex.

The third phase – below the second transition – could not be structurally characterised, although the volume change upon the spin transition was comparable to that of the first. There are several different situations one can envisage for the structural evolution of the final phase including, but not limited to the following:

i) A crystallographic phase transition to a lower symmetry space group with an ordered distribution of high spin sites in a predominantly low spin lattice, resembling the infinite LS chains in the predominantly HS lattice observed in Phase 2.

ii) The structure has the same space group and unit cell as Phase 2, but with HS sites located on the two-fold axes. Two out of every three chains along the c-axis would be low spin in this case, effectively the origin of the cell would shift relative to that of Phase 2.

iii) A structure in which no further crystallographic phase transition has taken place from Phase 2, with the additional LS molecules distributed randomly throughout the existing HS sites. This would result in an averaging of the bond lengths and angles for the fully occupied iron centre to values which lie between the expected values for HS and LS molecules.

It may be possible to distinguish between these three different situations using a variety of techniques, including Mössbauer spectroscopy, Raman spectroscopy and X-ray absorption spectroscopy, and there is significant further work to be done with this sample to uncover the nature of the third transition. The presence of a slight hysteresis (as observed in the second partial SCO) is often indicative of a crystallographic phase transition and lends weight to the first two scenarios presented above.

Perhaps more important than discovering the nature of this final phase is determining why and how this ordered intermediate state forms. It has been noted in the case of $[Fe(2\text{-pic})_3]Cl_2 \bullet EtOH$[31] that the ordered intermediate state (characterised by additional Bragg reflections) is the result of competitive effects between local antiferromagnetic-like interactions between dimers and long-range elastic interactions.[32] Long-range elastic interactions depend upon strong intermolecular contacts to communicate the spin transition to all Fe^{II} centres in the lattice.[33] Ferric cations such as $[Fe^{III}(L1)]$ generally show poor cooperativity unless very strong intermolecular interactions are present in the lattice. In this sample, where no strong intermolecular interactions are apparent, the long-range elastic interactions may be sufficiently weak for the antiferromagnetic-like short range interactions to compete, resulting in the stepped transition.

For $[Fe(bapbpy)(NCS)_2]$, a possible explanation was suggested to account for the intermediate phase containing an ordered array of HS and LS centres in the unusual ratio of 1:2. This theory was based on the significant structural differences that occur as a result of the symmetry-breaking crystallographic phase transitions apparent in the sample. The authors proposed that 100% conversion from HS to LS states in one step may be energetically unfavourable as the structural changes that would be required would be too large. This suggests that the origin of the stepped SCO in that species could be structural rather than as a result of magnetic interactions.[27]

In $[Fe^{III}(L1)]ClO_4$, the structural modification during the first phase transition is identical on a molecular level to that observed in $[Fe(bapbpy)(NCS)_2]$. The number of molecules in the asymmetric unit increases from ½ to 1½, creating a supercell with three times the volume of the high temperature phase. In both cases the molecules in the HS phase all have C2 symmetry and in the intermediate phase one of the two crystallographically independent molecules no longer has this symmetry.

Unfortunately the final phase of $[Fe^{III}(L1)]ClO_4$ could not be fully structurally characterised, but the destruction of the crystal and the decrease in volume of the unit cell in Phase 3 (as evidenced by the powder diffraction study) point towards a significant structural phase transition like that observed in $[Fe(bapbpy)(NCS)_2]$. Consequently, it is possible that the stepped nature of the spin transition in this Fe^{III} may also be attributable to the structural rearrangement, rather than as a direct result of the magnetic interactions within the species.

In order to fully explore the interplay between the structural and spin transitions in $[Fe^{III}(L1)]ClO_4$, many more experiments could be envisaged. High resolution X-ray studies may reveal diffuse scattering, which can shed light on the correlations present in SCO systems. Analysis of the electron-phonon coupling using Raman investigations and computational methods may also lead to a clearer understanding of how and why this ordered intermediate state is formed. Variable temperature magnetism, diffraction, Raman and Mössbauer spectroscopic studies of the system under applied pressure may help to decouple the structural and spin transition, and hence lead to insights as to how the structure affects the spin state in these stepped spin crossover systems.

---

[1] M. Nihei, T. Shiga, Y. Maedab and H. Oshio, *Coordination Chemistry Reviews*, 2007, **251,** 2606 and references therein

[2] P. J. van Koningsbruggen, Y. Maeda, H. Oshio, P. Gütlich and H. A. Goodwin, *Top. Curr. Chem.*, 2004, **233**, 259 and references therein

[3] S. Hayami, T. Matoba, S. Nomiyama, T. Kojima, S. Osaki and Y. Maeda, *Bull. Chem. Soc. Jpn.*, 1997, **70**, 12, 3001

[4] R. Hernández-Molina, A. Mederos, S. Dominguez, P. Gili, C. Ruiz-Pérez, A. Castiñeiras, X. Solans, F. Lloret, and J. A. Real, *Inorg. Chem.*, 1998**, 37**, 5102

[5] M. D. Timken, C. E. Strouse, S. M. Soltis, S. A. Daverio, D. N. Hendrickson, A. M. Abdel-Mawgaud and S. R. Wilson, *J. Am. Chem. Soc.*, 1986, **108**, 3

[6] K. J. Haller, P. L. Johnson, R. D. Feltham and J. H. Enemark, ***Inorganica Chimica Acta,*** 1979, **33**, 119

[7] B. J. Kennedy, A. C. McGrath, K. S. Murray, B. W. Skelton, and A. H. White, *Inorg. Chem.*, 1987, **26**, 483

[8] S. Hayami, Z.-Z. Gu, H. Yoshiki, A. Fujishima, and O. Sato, *J. Am. Chem. Soc.*, 2001, **123**, 11644

[9] T. Ito, M. Sugimoto, H. Ito, K. Toriumi, H. Nakayama, W. Mori, and M. Sekizaki, *Chem. Lett.*, 1983, 121

[10] R. Boča, Y. Fukuda, M. Gembický, R. Herchel, R. Jaroščiak, W. Linert, F. Renz and J. Yuzurihara, *Chem. Phys. Lett.*, 2000, **325**, 411

[11] W. O. Koch, V. Schünemann, M. Gerdan, A. X. Trautwein, and H.-J. Krüger, *Chem. Eur. J.*, 1998, **4**, 686

[12] S. Hayami, Z.-Z. Gu, M. Shiro, Y. Einaga, A. Fujishima, and O. Sato, *J. Am. Chem. Soc.*, 2000**,** **122**, 7126

[13] M. D. Timken, S. R. Wilson, and D. N. Hendrickson, *Inorg. Chem.*, 1985, **24**, 3450

[14] M. S. Haddad, M. W. Lynch, W. D. Federer, and D. N. Herndrickon, *Inorg. Chem.*, 1981, **20**, 1, 123

[15] S. Hayami, S. Miyazaki, M. Yamamoto, K. Hiki, N. Motokawa, A. Shuto, K. Inoue, T. Shinmyozu, and Y. Maeda, *Bull. Chem. Soc. Jpn.*, 2006, **79**, 3, 442

[16] S. Floquet, A. J. Simaan, E. Rivière, M. Nierlich, P. Thuéry, J. Ensling, P. Gütlich, J.-J. Girerd and M.-L. Boillot, *Dalton Trans.*, 2005, 1734

[17] J. Tang, J. Sánchez Costa, S. Smulders, G. Molnár, A. Bousseksou, S. J. Teat, Y. Li, G. A. van Albada, P. Gamez and J. Reedijk. *Inorg. Chem.*, 2009, **48**, 5, 2128

[18] M. S. Shongwe, B. A. Al-Rashdi, H. Adams, M. J. Morris, M. Mikuriya, and G. R. Hearne, *Inorg. Chem.*, 2007, **46**, 23, 9558

[19] M. S. Haddad, W. D. Federer, M. W. Lynch, and D. N. Hendrickson, *Inorg. Chem.*, 1981, **20**, 1, 131

[20] G. Morgan, H. Müeler-Bunz, Private Communication, 2008

[21] *SMART-NT, Data Collection Software, version 6.1,* Bruker Analytical X-ray Instruments Inc., Madison, WI, USA, 2000

[22] *SAINT-NT, Data Reduction Software, version 6.1*, Bruker Analytical X-ray Instruments Inc., Madison, WI, USA, 2000

[23] G. M. Sheldrick, *Acta Cryst.*, 2008, **A64**, 112

[24] O. V. Dolomanov, L. J. Bourhis, R. J. Gildea, J. A. K. Howard and H. Puschmann, *J. Appl. Cryst.*, 2009, **42**, 339

[25] A. E. Goeta, L. K. Thompson, C. L. Sheppard, S. S. Tandon, C. W. Lehmann, J. Cosier, C. Webster and J. A. K. Howard, *Acta Cryst.*,1999, **C55**, 1243

[26] S. Bonnet, M. A. Siegler, J. Sánchez Costa, G. Molnár, A. Bousseksou, A. L. Spek, P. Gameza and J. Reedijk, *Chem. Commun.*, 2008, 5619

[27] S. Bonnet, G. Molnár, J. Sánchez Costa, M. A. Siegler, A. L. Spek, A. Bousseksou, W.-T. Fu, P. Gamez, and J. Reedijk, *Chem. Mater.*, 2009, **21**, 1123

[28] D. Boinnard, A. Bousseksou, A. Dworkin, J.-M. Savariault, F. Varret, and J.-P. Tuchagues, *Inorg. Chem.*, 1994, 271

[29] D. L. Reger, C. A. Little, V. G. Young, Jr. and M. Pink, *Inorg. Chem.*, 2001, **40**, 2870

[30] Y. Garcia, O. Kahn, L. Rabardel, B. Chansou, L. Salmon, and J. P. Tuchagues, *Inorg. Chem.*, 1999, **38**, 4663

[31] D. Chernyshov, M. Hostettler, K. W. Törnroos, and H.-B. Bürgi, *Angew. Chem. Int. Ed.*, 2003, **42**, 3825

[32] H. Spiering, T. Kohlhaas, H. Romstedt, A. Hauser, C. Bruns-Yilmaz and J. Kusz, P. Gütlich, *Coord. Chem. Rev.*, 1999, **190–192**, 629

[33] J. A. Real, A. B. Gaspar, V. Niel and M. C. Muñoz, *Coord. Chem. Rev.*, 2003, **236**, 121

6 Thermally Induced Excited Spin State Trapping in [Fe(picen)(NCS)$_2$]

6.1 Introduction

6.1.1 Thermally Induced Excited Spin State Trapping

There are several reports in the literature of Fe^{II} systems in which it is possible to trap the meta-stable high spin state of a spin crossover material at low temperatures not as a result of light-irradation as with the LIESST effect, but through fast cooling or flash freezing of the sample.[1,2,3,4,5] Dubbed thermally induced excited spin state trapping or TIESST, the majority of studies used Mössbauer and magnetic measurements to investigate the relaxation processes involved. T_{TIESST} may be defined by analogy to T_{LIESST} as the minimum of the $d\chi_M T/dT$ vs. T curve on warming after flash freezing to low temperature and is characteristic of each sample.[6] In all cases so far studied, the values of T_{LIESST} and T_{TIESST} are the approximately equivalent for a given compound. Relatively few examples of the thermally induced meta stable HS state have been characterised using crystallographic techniques.[7,8,9]

The complex [Fe(PM-BiA)$_2$(NCS)$_2$] (Figure 1.13a) shows thermal trapping of the HS state when the sample is flash cooled to temperatures below T_{LIESST}, which is 78 K for this sample.[7] The study by M. Marchive *et al.* revealed that flash cooling to 80 K also results in trapping of the HS state, but after a few minutes the structure relaxes back to the LS state. Above this temperature TIESST is not possible and below this temperature the trapped HS state is stable for a period of hours. During this investigation, [Fe(phen)$_2$(NCS)$_2$] was also tested for TIESST behaviour, but was found not to show this phenomenon. It was suggested by the authors that the reason for the absence of TIESST behaviour was possibly the relatively small difference in average bond length between HS and LS states for [Fe(phen)$_2$(NCS)$_2$] (0.173 Å) compared to that observed in [Fe(PM-BiA)$_2$(NCS)$_2$] (0.235 Å).

Another Fe^{II} species that shows interesting TIESST behaviour is [FeL$_2$](BF$_4$)$_2$, where L = 2,6-bis(3-methylpyrazol-1-yl)-pyridine, the cation of which is shown in Figure 6.1. The study by V. Money *et al.*[8] revealed that when cooled from room temperature to 10 K at

a rate of 60 K/hour a partial spin transition occurs in two steps, with a final $\chi_M T$ value of 1.6 cm^3 K mol^{-1}, equating to a ~ 46% residual HS component at 10 K. However, when the sample is cooled from room temperature to 100 K and left at this temperature for a period of 2 – 3 hours, the spin transition goes to completion with no residual high spin component at low temperatures. The study showed that kinetic effects dominate in this sample at temperatures between 100 K and 120 K, while above 130 K these effects are negligible.

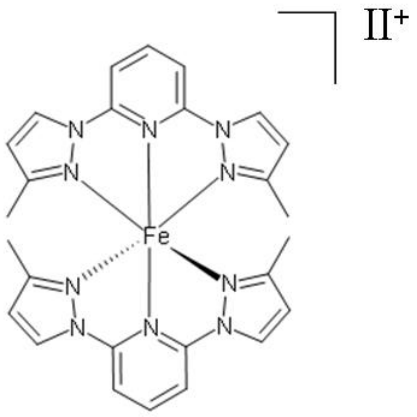

Figure 6.1. The dication in [FeL$_2$](BF$_4$)$_2$, where L = 2,6-bis(3-methylpyrazol-1-yl)-pyridine

Flash freezing of [FeL$_2$](BF$_4$)$_2$ results in a TIESST effect, with a residual HS component of ~ 70% at 10 K. T_{LIESST} and T_{TIESST} for this sample are 86 K and 88 K respectively and the relaxation from both the thermal and light-induced HS states is very similar. The authors attributed this behaviour to these two HS states being structurally very similar, although this could not be confirmed by crystallographic techniques as the crystals collapse at low temperatures.

6.1.2 [Fe(picen)(NCS)$_2$]

[Fe(picen)(NCS)$_2$], (picen = N,N′-bis-(2-pyridylmethyl)ethylenediamine), (Figure 6.2), has been shown using magnetic data to undergo a thermally induced spin transition, with $T_{1/2}$ = 64 K.

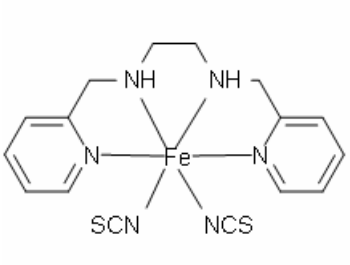

Figure 6.2. [Fe(picen)(NCS)$_2$]

Magnetic studies also show that the degree of conversion to the LS state for [Fe(picen)(NCS)$_2$] varies depending on the rate of cooling, with slower cooling rates resulting in an increased percentage of conversion to the low spin state, as shown in Figure 6.3. A fast cooling rate of 420 K/hour results in a residual HS fraction of approximately 60%, while a slow cooling rate of just 3.6 K/hour leads to a residual HS component of ~ 15%. On warming from base temperature there is a thermal hysteresis in the magnetic behaviour. For the faster cooling rates there is a distinct decrease in $\chi_M T$ at approximately 58 K before an increase corresponding to the thermal LS → HS spin transition.

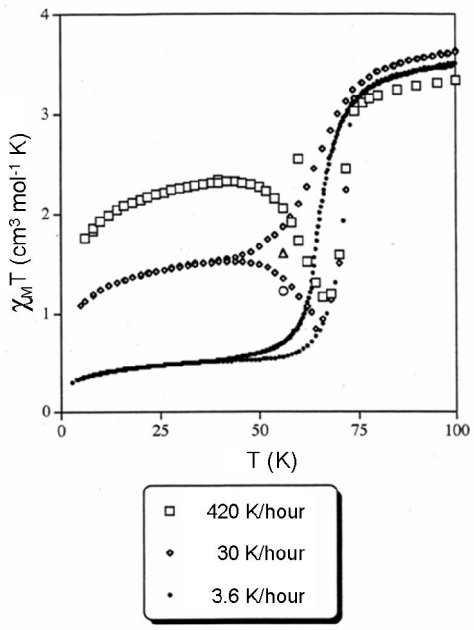

Figure 6.3 . Magnetic behaviour of [Fe(picen)(NCS)$_2$] as a function of temperature[10]

A series of single crystal X-ray diffraction experiments were performed with the intention of examining the structural behaviour of this species and to determine

whether this had an influence on its unusual magnetic properties. The aim was to investigate the structure in the HS state above the transition and at low temperature after various cooling rates in an analogous manner to the magnetism experiment. The effect of laser irradiation on the structure at low temperature was also investigated.

6.2 Experimental

Single-crystal structure determinations were carried out from X-ray data collected at 120 K and 30 K using graphite-monochromated Mo-Kα radiation (λ = 0.71073 Å) on a Bruker SMART-CCD 1 K diffractometer. A series of narrow ω-scans (0.3°) was performed at several φ-settings in such a way as to cover a sphere of data to a maximum resolution of 0.75 Å. Cell parameters were determined and refined using SMART software,[11] and raw frame data were integrated with the SAINT program.[12] The structures were solved by direct methods using SHELXS,[13] and refined by full-matrix least-squares on F^2 using SHELXL-97[13] and the graphical user interface Olex2.[14]

The experiments performed were as follows:

1) Structure determination at 120 K after cooling at 2 K/min – denoted **120 K**.

2) Structure at 30 K after flash freezing from room temperature – denoted **Flash**.

3) Structure at 30 K after cooling from 120 K at a rate of 360 K/hour – denoted **Fast**.

4) Structure at 30 K after cooling from 120 K at a rate of 30 K/hour – denoted **Medium**.

5) Structure at 30 K after cooling from 120 K at a rate of 3 K/hour – denoted **Slow**.

6) Structure at 30 K after cooling from 120 K at a rate of 3 K/hour, followed by irradiation with a laser (670 nm, 5mW) for 10 mins – denoted **Slow + hv**.

The temperature was controlled using an Oxford Cryosystems Cryostream[15] for the 120 K dataset and an Oxford Cryosystems Helix[16] for the 30 K datasets. The same crystal was used for the **HS**, **Flash**, **Fast**, **Med** and **Slow** diffraction experiments; the **Slow + hv** experiment was performed on a different crystal of similar size and quality.

6.3 Results

6.3.1 High Spin Structure at 120 K

The molecular structure of this compound at **120 K** is shown in Figure 6.4. At this temperature all Fe – N bond distances are well within the usual range for HS Fe^{II}, as expected from analysis of the magnetic data.

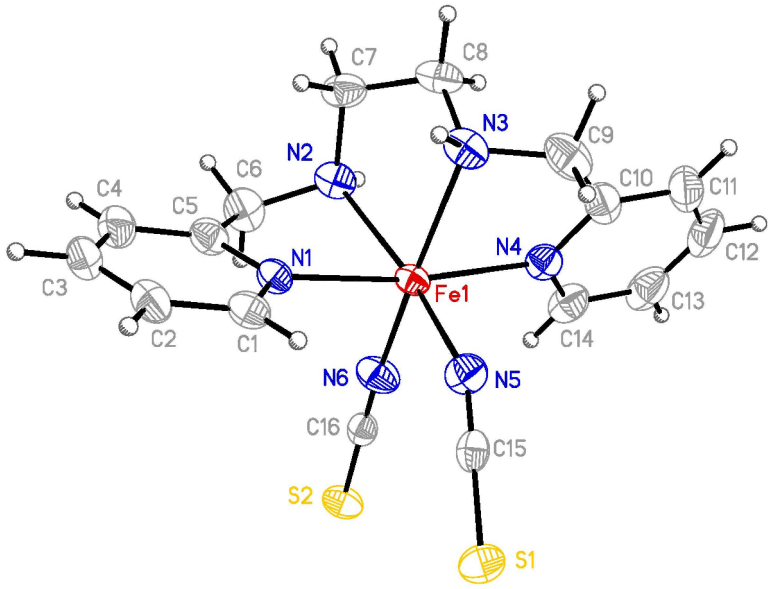

Figure 6.4. Molecular structure of [Fe(picen)(NCS)$_2$] at 120 K, showing labelling scheme. ADPs are shown at 50% probability

6.3.2 Structure as a Function of Variable Cooling Rate

In all cases the space group is P2$_1$/n, and the unit cell is unchanged except for effects of thermal contraction and the usual difference in volume attributable to a percentage of the molecules having undergone a spin transition, i.e. no phase transition occurs as a result of cooling under any of the investigated regimes, or as a result of laser irradiation. Unit cell parameters and selected crystallographic data may be found in Table 6.1.

There is a complex network of short intermolecular contacts throughout the crystal. The packing of these molecules may be considered as a series of sheets, formed through C-H…C interactions, in the ac-plane. Intrasheet contacts are through N-H…S and C-H…S interactions, propagating the sheets along the b-axis. A packing diagram

is shown in Figure 6.5. The structure of the molecule from all six experiments shows the same packing motif, the only differences being in the distances of the short contacts, resulting from the decrease in temperature as well as the spin transition.

Table 6.1 Selected crystallographic data for the title compound after various cooling regimes, as defined in the text

Phase	HS	Flash	Fast	Med	Slow	Slow + hv
T /K	120	30	30	30	30	30
Cooling /K/hr		instant	360	30	3	3
Space Group			$P2_1/n$			
a /Å	9.256(2)	9.189(4)	9.155(1)	9.146(1)	9.107(1)	9.167(2)
b /Å	13.759(1)	13.712(4)	13.696(2)	13.723(2)	13.742(2)	13.691(3)
c /Å	14.627(2)	14.521(5)	14.461(2)	14.379(2)	14.318(2)	14.559(3)
β /°	92.32(1)	92.399(5)	92.279(2)	91.972(2)	91.949(2)	92.621(3)
V /Å^3	1861.2(5)	1828.2(9)	1811.8(4)	1803.8(4)	1790.8(4)	1825.4(7)
Density	1.479	1.505	1.519	1.526	1.537	1.508
Ind. Refs.	3269	3731	4105	4071	3716	3228
R_{int}	0.0414	0.0558	0.0513	0.0428	0.0484	0.080
R_1 [I > 2 σ (I)]	0.039	0.037	0.0351	0.039	0.038	0.044
R_1 [all data]	0.061	0.051	0.0506	0.049	0.057	0.077
wR_2 [I > 2 σ (I)]	0.0959	0.0888	0.0901	0.0802	0.0867	0.086
wR_2 [all data]	0.0996	0.0944	0.0963	0.0853	0.0947	0.096

There is no phase transition observed, and there is also no splitting of the Bragg reflections observed for this sample, indicating that during the spin transition the LS sites are distributed randomly throughout the lattice. In such a case, the bond lengths associated with the FeN_6 coordination sphere are expected to be a weighted average between HS and LS states. The values of these distances for all structures are summarised in Table 6.2, along with calculated values for the fraction of residual HS centres at 30 K.

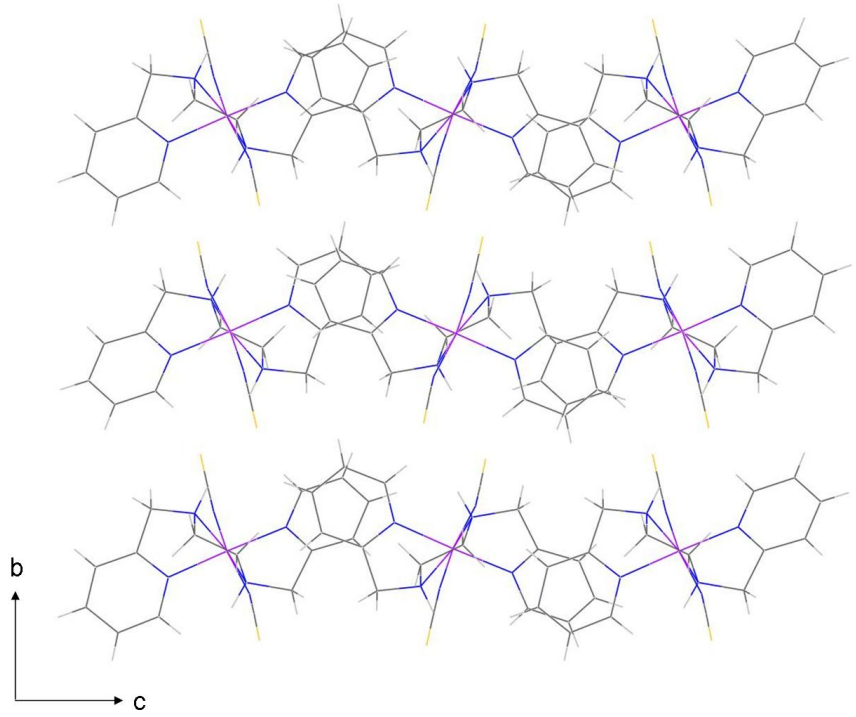

Figure 6.5. View of the crystal packing of [Fe(picen)(NCS)$_2$] along the a-axis showing the formation of sheets in the ac-plane

Table 6.2. Iron - Nitrogen bond lengths for all structures. V_{coord} indicates volume of coordination octahedron. Residual HS fraction is calculated from V_{coord}, assuming V_{coord}(HS) = 13.1(1) and V_{coord}(LS) = 10.0(1) Å^3.[17,18]

	HS	Flash	Fast	Medium	Slow	Slow + hv
T / K	120	30	30	30	30	30
Fe – N1 / Å	2.198(1)	2.171(2)	2.121(2)	2.081(2)	2.032(2)	2.188(3)
Fe – N2 / Å	2.237(2)	2.214(2)	2.155(2)	2.121(2)	2.067(2)	2.212(3)
Fe – N3 / Å	2.219(2)	2.197(2)	2.146(2)	2.108(2)	2.060(2)	2.231(3)
Fe – N4 / Å	2.189(1)	2.165(2)	2.118(2)	2.079(2)	2.036(2)	2.186(3)
Fe – N5 / Å	2.109(3)	2.097(2)	2.052(2)	2.031(2)	1.997(2)	2.115(3)
Fe – N6 / Å	2.087(3)	2.075(2)	2.035(2)	2.010(2)	1.985(2)	2.099(3)
V_{coord} / Å^3	13.12(1)	12.82(1)	12.06(1)	11.55(1)	10.94(1)	13.12(1)
% residual HS	100	90	66	50	30	100
% LS	0	10	34	50	70	0

As expected, the largest difference in bond lengths is observed between the structures from the **HS** and **Slow** experiments. After the **Slow** experiment 70% of the Fe centres have undergone a spin transition, the effect of this on the structure is shown in the overlay of the **HS** and **Slow** structures in Figure 6.6. Results from other experiments with faster cooling rates resulted in structures with intermediate bond lengths as would be expected for systems with a higher residual HS component than the **Slow** structure.

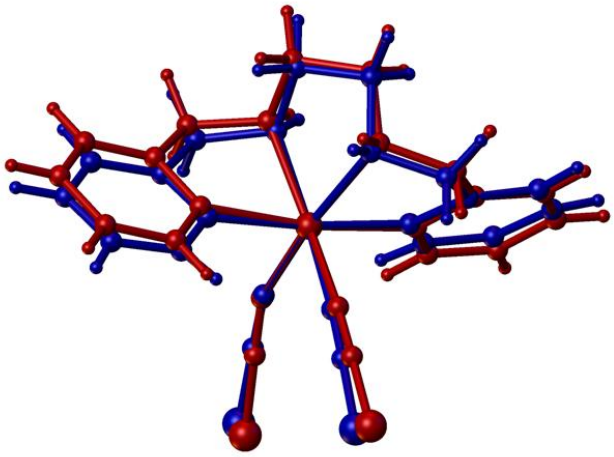

Figure 6.6. Overlay of HS structure (red) and structure after Slow cooling (blue) of [Fe(picen)(NCS)$_2$]

6.3.3 LIESST Experiment

A sample was cooled to 30 K from 120 K at a rate of 3 K/hour and irradiated with a laser (670 nm, 5mW) for 10 minutes while rotating the crystal to ensure even illumination) in order to determine the nature of the light induced metastable (HS*) state. A data collection was performed at 30 K, the structure again showing no evidence of a phase transition. Structural features of this phase are presented in Table 6.2 and reveal 100% photo-induced conversion to the HS state is possible at this temperature.

Data were subsequently collected on warming at 3 K/hour from 30 K (after irradiation) to determine the dependence of the unit cell parameters on temperature. The variation of the unit cell volume is shown in Figure 6.7, where relaxation from the HS* state (between 45 K and 60 K) and the thermal spin transition from LS to HS (between 70 K

and 80 K) are both clearly visible. Each data point represents a range of no more than 2 Kelvin.

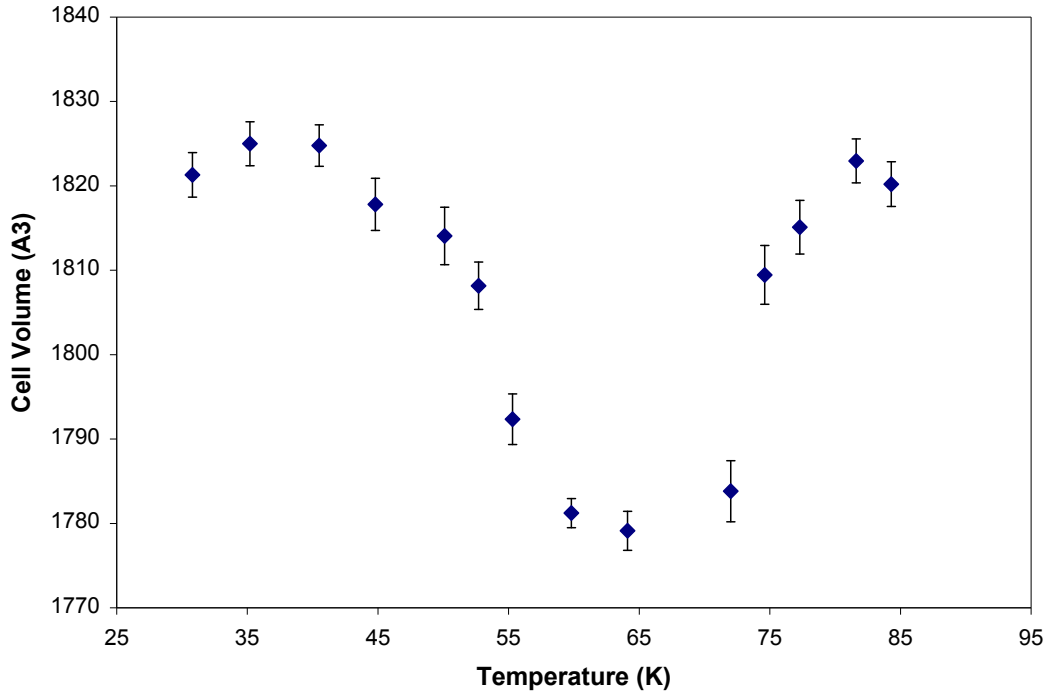

Figure 6.7. Graph showing the evolution of the unit cell volume as a function of temperature for [Fe(picen)(NCS)$_2$] on warming following irradiation at 30 K

It is proposed that the close proximity of $T_{½}$ and T_{LIESST} and the lack of any crystallographic phase transition provide a means for the TIESST behaviour in [Fe(picen)(NCS)$_2$].

6.3.4 Structural observations

The atomic displacements parameters (ADPs) can provide important information about the structural changes observed on the spin transition and as such are worth examining. Their size and shape is dependent on several factors, two of the most important being temperature and disorder (assuming data quality and resolution is sufficient). From a crystallographic point of view, a random distribution of structurally different HS and LS sites throughout the lattice manifests itself as one crystallographically unique iron site with a large variation in Fe – N bond distances and angles at that iron centre. This disorder of the spin states results in enlarged ADPs

for the whole structure. The ADPs might be expected to be largest when the ratio of HS:LS sites is approximately equal. As mentioned previously, the structural features which undergo the most pronounced change during spin crossover are those directly associated with the FeN_6 coordination sphere, hence it is the size of the ADPs of the nitrogen atoms that will yield the most information regarding the HS:LS ratio for structures collected at the same temperature. Figure 6.8 shows ADPs for all of the determined structures, along with average U_{iso} values for the N atoms in each structure. U_{iso} values were used as a convenient single figure with which to quantify the size of the atomic displacement. ADPs are defined by a greater number of values and have distinct orientations, making direct numerical comparison difficult. In order to calculate the average U_{iso} value, the nitrogen atoms were refined using an isotropic model, while all other atoms were refined using the usual anisotropic model; the mean nitrogen U_{iso} value was then calculated for each structure.

Examination of the structures after **Flash**, **Fast**, **Med** and **Slow** cooling modes reveals larger ADPs than would normally be expected at 30 K, reflecting the random distribution of spin states throughout the crystal that is observed for the system under these conditions. The structure after irradiation (**Slow +hv**) shows significantly smaller ADPs than any of the other structures acquired at 30 K, consistent with a full photo-induced conversion to one single (HS) state. The ADPs for this structure are also much smaller than those seen in the only other fully HS structure, which was collected at 120 K, and are a direct result of the difference in temperature between these two measurements.

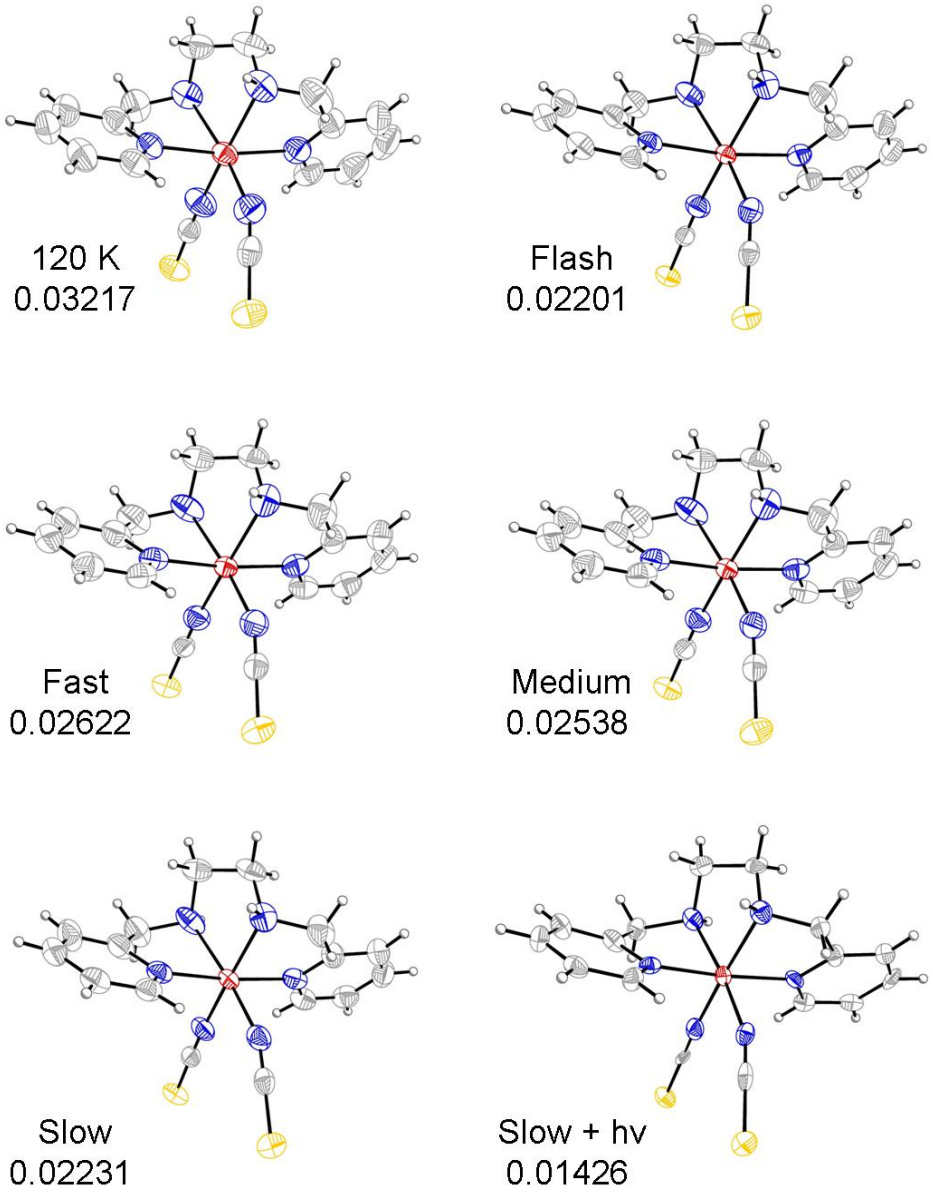

Figure 6.8. Molecular structure of [Fe(picen)(NCS)$_2$] and average U_{iso} values for the nitrogen atoms at 120 K and 30 K after various cooling and light irradiation regimes – see text for definition. Atomic displacement parameters are drawn at 80% probability

Figure 6.9 shows the variation of this average U_{iso} value as a function of the percentage of HS molecules in the sample. This graph was plotted using only data collected at 30 K so as to remove the effect of temperature on the U_{iso} values. As predicted, the U_{iso} values are considerably higher when there is a mixed spin state, with the highest values occurring in the two structures with the similar proportions of HS and LS states.

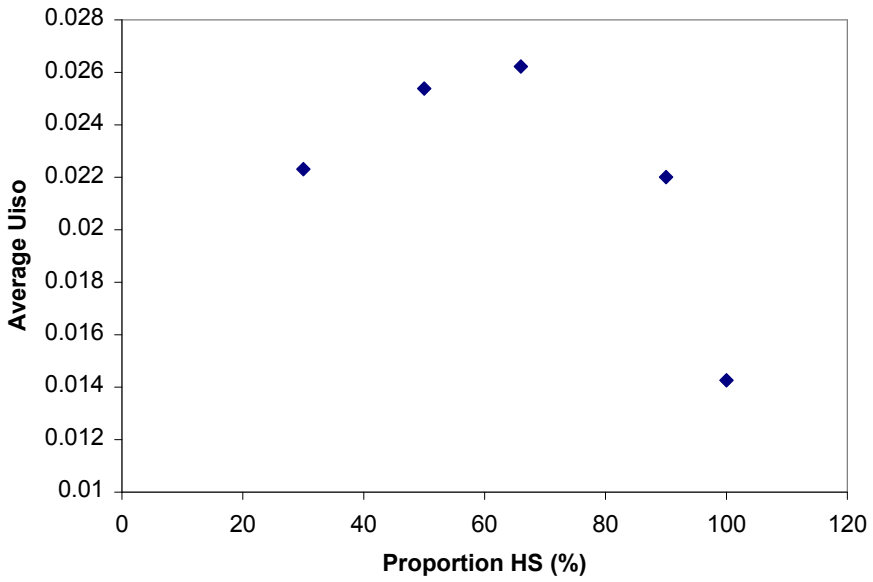

Figure 6.9. Graph showing average U_{iso} of the 6 N atoms as a function of the Proportion of HS molecules at 30 K

6.4 Conclusions

The spin transition of [Fe(picen)(NCS)$_2$] has been investigated using X-ray diffraction methods and the mechanism has been deduced.

The mechanism involves a random distribution of HS and LS sites throughout the crystal. The relative proportion of HS and LS has been quantified using information contained within structural details; bond distances, the volume of the coordination polyhedron and atomic displacement parameters can all be used as a means of gaining insight into the properties of the material.

It is possible to induce a full conversion to the meta-stable high spin state in the crystal using laser irradiation. The percentage conversion from HS to LS states in this system is dependent on the rate of cooling of the sample through the transition. The proximity of the temperature of the thermal spin transition ($T_{½}$) and the temperature at which the HS* state is stable at low temperatures (T_{LIESST}) allows for the thermal trapping of the high spin state.

The relaxation of the HS* state on warming after LIESST was monitored by plotting the volume of the unit cell as a function of temperature. The relaxation curve obtained

mirrors that observed on warming after thermal trapping of the HS state, as determined by magnetometry. V. Money *et al.*[8] attributed this relationship in relaxation behaviour in another Fe^{II} species to a strong similarity between the structure between the HS species attained by laser irradiation and after thermal trapping but this could not be investigated crystallographically. For [Fe(picen)(NCS)$_2$], a 100% HS thermally trapped species could not be achieved, as even flash freezing of the sample results in a partial spin transition to the LS state of 10% of the crystal. However, it is clear that the thermally trapped HS species and the light induced HS* species are isostructural, supporting the suggestion made in the previous study.

---

[1] G. Ritter, E. König, W. Irler, and H. A. Goodwin, *Inorganic Chemistry*, 1978, **17**, 2, 224

[2] T. Buchen, P. Gütlich, K. H. Sugiyarto, and H. A. Goodwin, *Chem. Eur. J.*, 1996, **9**, 2, 1134

[3] A. F. Stassen, O. Roubeau, I. Ferrero Gramage, J. Linarès, F. Varret, I. Mutikainen, U. Turpeinen, J. G. Haasnoot, J. Reedijk, *Polyhedron*, 2001, **20**, 1699

[4] O. Roubeau, M. deVos, A.F. Stassen, R. Burriel, J.G. Haasnoota, J. Reedijk, *Journal of Physics and Chemistry of Solids*, 2003, **64,** 1003

[5] S. M. Neville, B. A. Leita, G. J. Halder, C. J. Kepert, B. Moubaraki, J.-F. Létard, and K. S. Murray, *Chem. Eur. J.*, 2008, **14**, 10123

[6] J.-F. Létard, *J. Mater. Chem.*, 2006, **16**, 2550

[7] M. Marchivie, P. Guionneau, J.F. Létard, D. Chasseau, J.A.K. Howard, *Journal of Physics and Chemistry of Solids*, 2004, **65**, 17

[8] V. A. Money, C. Carbonera, J. Elhaïk, M. A. Halcrow, J. A. K. Howard, and J.-F. Létard, *Chem. Eur. J.*, 2007, **13**, 5503

[9] C.-F. Sheu, S. Pillet, Y.-C. Lin, S.-M. Chen, I-J. Hsu, C. Lecomte, and Y. Wang, *Inorganic Chemistry*, 2008, **47**, 23, 10866

[10] P. Guionneau et al. unpublished work

[11] *SMART-NT, Data Collection Software, version 6.1,* Bruker Analytical X-ray Instruments Inc., Madison, WI, USA, 2000

[12] *SAINT-NT, Data Reduction Software, version 6.1*, Bruker Analytical X-ray Instruments Inc., Madison, WI, USA, 2000

[13] G. M. Sheldrick, *Acta Cryst.*, **A64**, 2008, 112

[14] O. V. Dolomanov, L. J. Bourhis, R. J. Gildea, J. A. K. Howard, and H. Puschmann, *J. Appl. Cryst.*, 2009, **42**, 339

[15] J. Cosier and A. M. Glazer, *J. Appl. Cryst.*, 1986, **19**, 105

[16] A. E. Goeta, L. K. Thompson, C. L. Sheppard, S. S. Tandon, C. W. Lehmann, J. Cosier, C. Webster and J. A. K. Howard, *Acta Cryst.*, 1999, **C55**, 1243

[17] P. Guionneau, F. Le Gac, A. Kaiba, J. Sanchez Costa, D.l Chasseau and J.-F. Letard *Chem. Commun.*, 2007, 3723

[18] P. Guionneau, M. Marchivie, G. Bravic, J. F. Létard and D. Chasseau, *Top. Curr. Chem.*, 2004, **234**, 97

7 Gradual Spin Transition in [Fe(L2)]2ClO4

7.1 Introduction

The crystal structure of [Fe(L2)]2ClO4 (where L2 = 1,4,7-tris(2-aminophenyl)-1,4,7-triazacyclononane) – shown in Figure 7.1 – was published by I. A. Fallis *et. al.* in 2000.[1] The interest of the authors in synthesising this complex was in coordination chemistry of the novel ligand type, and although magnetic measurements were performed at that time, there was no indication in the paper that the species possessed any spin crossover properties. The crystal structure they report was collected at room temperature and the bond lengths appeared to be intermediate between those expected for Fe^{II} – N bonds in the HS and LS states. These distances ranged from 2.092(3) to 2.113(3) Å; expected values for these bond types in the high spin state are approximately 2.2 Å, while in the low spin state these values would be closer to 2 Å.[2] According to the authors, the spin state cannot be determined using their crystallographic data alone. It was decided that further investigation of this sample was merited in an attempt to explain the unusual behaviour of the species.

A crystalline sample of this species was obtained from the original authors and a variable temperature X-ray diffraction study was carried out to determine the reason for these unusual bond lengths; subsequently variable temperature magnetic measurements were also performed using a SQUID magnetometer.

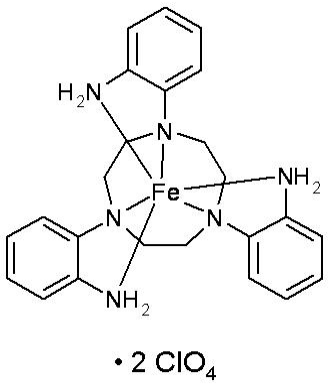

Figure 7.1. [Fe(L2)]2ClO4

7.2 Experimental

Single crystal X-ray diffraction experiments were performed between 120 and 430 K, above which temperature the crystal melts. The crystal was mounted on a glass fibre in epoxy resin glue, and the same crystal was used for all diffraction experiments. During the diffraction experiment, the temperature was controlled using a Cryostream N_2 open flow cooling device,[3] which can attain a maximum temperature of 500 K. A similar device with a maximum temperature of 400 K was used to control the temperature while taking photographs of the crystal colour. The temperature was ramped at a rate of 80 K/hour between the temperatures at which data were collected.

Single-crystal structure determinations were carried out from X-ray data collected between 120 K and 430 K using graphite-monochromated Mo-Kα radiation (λ = 0.71073 Å) on a Bruker SMART-CCD 1 K diffractometer. A series of narrow ω-scans (0.3°) were performed at several φ-settings in such a way as to cover a sphere of data to a maximum resolution of 0.75 Å. Cell parameters were determined and refined using SMART software,[4] and raw frame data were integrated with the SAINT program.[5] The structures were solved by direct methods using SHELXS,[6] and refined by full-matrix least-squares on F^2 using SHELXL-97[6] and the graphical user interface Olex2.[7]

There is an increasing degree of disorder of the perchlorate groups and, to a lesser extent, the phenyl groups of the ligand as temperature increases. The disorder in the ligand is likely to be a combination of the random distribution of HS and LS sites throughout the lattice at the intermediate temperatures and dynamic disorder. In the case of the perchlorate the disorder is most likely dynamic in nature as it increases with increasing temperature.

7.3 Results

7.3.1 X-Ray Diffraction

The molecular structure at 120 K is presented in Figure 7.2, showing the numbering scheme used for the structure at all temperatures. Selected crystallographic data for the structure at all temperatures are given in Table 7.1.

Table 7.1. Selected crystallographic data for the title compound at each temperature

Temperature /K	120	165	210	250	295	335	350	370	390	410	430
Empirical formula	$C_{24}H_{30}N_6FeCl_2O_8$										
Crystal system	Orthorhombic										
Space group	Pbca										
a/Å b/Å c/Å	13.5972(9) 14.1584(9) 27.9217(18)	13.6149(7) 14.1870(8) 27.9584(15)	13.6440(6) 14.2136(6) 27.9942(12)	13.7049(7) 14.2697(8) 28.1170(15)	13.798(2) 14.333(2), 28.300(4)	13.8038(6) 14.3186(6) 28.3175(6)	13.8401(10) 14.3475(10) 28.3831(9)	13.8716(13) 14.3686(12) 28.430(3)	13.8955(16) 14.3843(15) 28.470(3)	13.9084(11) 14.4008(11) 28.500(2)	13.9289(8) 14.4048(8) 28.5379(15)
Volume/Å^3	5375.3(6)	5400.3(5)	5428.9(4)	5498.7(5)	5596.6(15)	5597.0(4)	5636.1(6)	5666.5(9)	5690.6(11)	5708.4(8)	5725.9(5)
Z	8										
ρ_{calc}mg/mm^3	1.624	1.617	1.608	1.588	1.560	1.560	1.549	1.541	1.534	1.530	1.525
μ/mm^{-1}	0.821	0.817	0.813	0.803	0.793	0.789	0.783	0.779	0.776	0.773	0.771
Crystal size	0.28 × 0.21 × 0.19	0.28 × 0.21 × 0.19	0.28 × 0.21 × 0.18	0.28 × 0.21 × 0.19	0.28 × 0.21 × 0.19	0.28 × 0.21 × 0.19	0.28 × 0.21 × 0.19	0.28 × 0.21 × 0.19	0.28 × 0.21 × 0.19	0.28 × 0.21 × 0.19	0.28 × 0.21 × 0.19
Theta range	2.09 to 25.03°	1.46 to 25.02°	1.45 to 25.03°	1.45 to 25.03°	2.06 to 25.02°	1.44 to 25.02°	2.06 to 25.03°	2.05 to 25.02°	2.05 to 23.98°	2.05 to 24.13°	2.04 to 24.09°
Reflections collected	40288	23685	44670	18477	22075	53676	41540	12081	9262	18251	36908
Independent reflections	4751 Rint = 0.0473	4652 Rint = 0.0463	4805 Rint = 0.0514	4743 Rint = 0.0476	4818 Rint = 0.0580	4822 Rint = 0.0680	4869 Rint = 0.0559	4825 Rint = 0.0469	3952 Rint = 0.0441	4098 Rint = 0.0485	4113 Rint = 0.0561
Data/restraints/parameters	4751/53/398	4652/53/398	4805/53/398	4743/53/398	4818/59/398	4822/59/398	4869/59/398	4825/59/398	3952/59/398	4098/131/438	4113/131/438
Goodness-of-fit on F^2	1.061	1.032	1.019	1.025	1.023	1.025	1.031	1.034	1.031	1.026	1.037
Final R indexes [I>2σ (I)]	R_1 = 0.0309 wR_2 = 0.0761	R_1 = 0.0379 wR_2 = 0.0895	R_1 = 0.0412 wR_2 = 0.1005	R_1 = 0.0484 wR_2 = 0.1152	R_1 = 0.0454 wR_2 = 0.1055	R_1 = 0.0480 wR_2 = 0.1149	R_1 = 0.0488 wR_2 = 0.1203	R_1 = 0.0557 wR_2 = 0.1344	R_1 = 0.0537 wR_2 = 0.1295	R_1 = 0.0491 wR_2 = 0.1202	R_1 = 0.0469 wR_2 = 0.1156
Final R indexes [all data]	R_1 = 0.0368 wR_2 = 0.0787	R_1 = 0.0486 wR_2 = 0.0950	R_1 = 0.0500 wR_2 = 0.1057	R_1 = 0.0698 wR_2 = 0.1270	R_1 = 0.0653 wR_2 = 0.1166	R_1 = 0.0730 wR_2 = 0.1292	R_1 = 0.0722 wR_2 = 0.1316	R_1 = 0.0981 wR_2 = 0.1532	R_1 = 0.0907 wR_2 = 0.1485	R_1 = 0.0751 wR_2 = 0.1319	R_1 = 0.0711 wR_2 = 0.1272
Largest diff. peak/hole /e.-Å^{-3}	0.502/-0.354	0.845/-0.361	0.999/-0.539	0.776/-0.498	0.441/-0.344	0.496/-0.378	0.468/-0.327	0.450/-0.274	0.402/-0.250	0.335/-0.220	0.313/-0.249

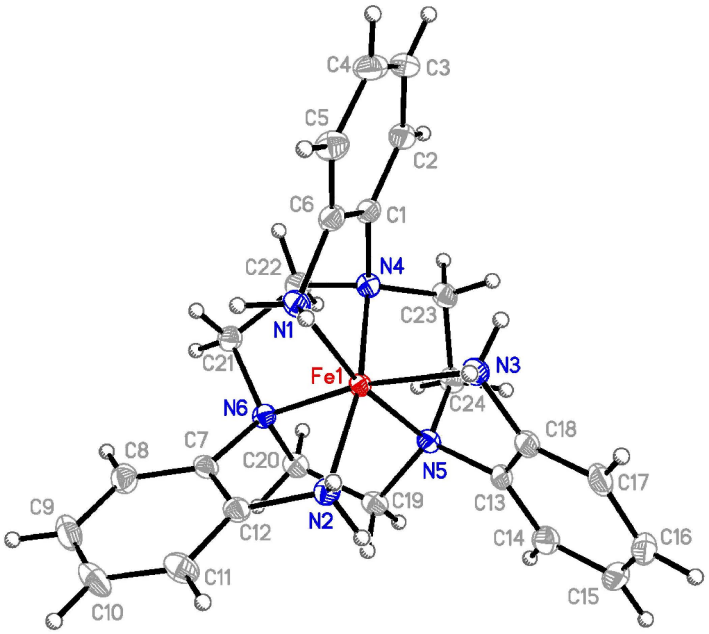

Figure 7.2. Molecular structure of [Fe(L2)]2ClO4 at 120 K. Atomic displacement parameters are drawn at 50% probability; counterions have been omitted for clarity

At 120 K it is clear from analysis of the bond lengths and other geometrical features that the iron centre is in the low spin state. These bond lengths, together with those from all other temperatures are shown in Table 7.2, and are plotted as a function of temperature in Figure 7.3.

The degree deviation from a perfect octahedron is more pronounced for iron systems in the high spin rather than the low spin state. This has been quantified in the literature using the structural parameter Σ, which is the sum of the deviation from 90° of each of the 12 cis angles that would be defined as right angled in an ideal octahedron (where Σ = 0).[2] The value of Σ for the structure at each temperature is also given in Table 7.2, and is plotted as a function of temperature in Figure 7.4.

The volume of the iron coordination octahedron (V_{coord}) is a structural parameter that has been used to quantify the proportion of each component in a mixed spin system.[2] The values of V_{coord} for the iron centre at each temperature are also given in Table 7.2.

Table 7.2. Selected geometrical parameters for the title compound across the studied temperature range

Temp. (K)		120	165	210	250	295	335	350	370	390	410	430
Bond Distances (Å)												
Fe1	N1	2.095(2)	2.094(2)	2.096(3)	2.115(3)	2.154(3)	2.168(4)	2.179(3)	2.187(4)	2.189(4)	2.200(4)	2.195(4)
Fe1	N2	2.021(2)	2.016(2)	2.018(3)	2.035(3)	2.084(3)	2.104(4)	2.118(3)	2.133(4)	2.137(4)	2.140(4)	2.141(4)
Fe1	N3	2.010(2)	2.005(2)	2.009(2)	2.025(3)	2.083(3)	2.104(3)	2.120(3)	2.128(4)	2.135(4)	2.136(4)	2.138(4)
Fe1	N4	1.958(2)	1.960(2)	1.968(2)	2.004(3)	2.067(3)	2.106(3)	2.122(3)	2.132(3)	2.140(4)	2.149(3)	2.149(3)
Fe1	N5	2.047(2)	2.048(2)	2.058(2)	2.089(3)	2.150(3)	2.180(3)	2.195(3)	2.207(4)	2.215(4)	2.217(4)	2.217(3)
Fe1	N6	1.991(2)	1.994(2)	2.003(2)	2.035(3)	2.108(3)	2.141(3)	2.161(3)	2.170(4)	2.178(4)	2.189(3)	2.186(3)
Σ (°)		56(1)	57(1)	60(1)	69(1)	89(1)	103(1)	108(1)	112(1)	114(1)	115(1)	116(1)
V_{coord} (Å^3)		10.83(1)	10.81(1)	10.90(1)	11.26(1)	12.11(1)	12.47(1)	12.69(1)	12.84(1)	12.93(1)	13.03(1)	13.01(1)

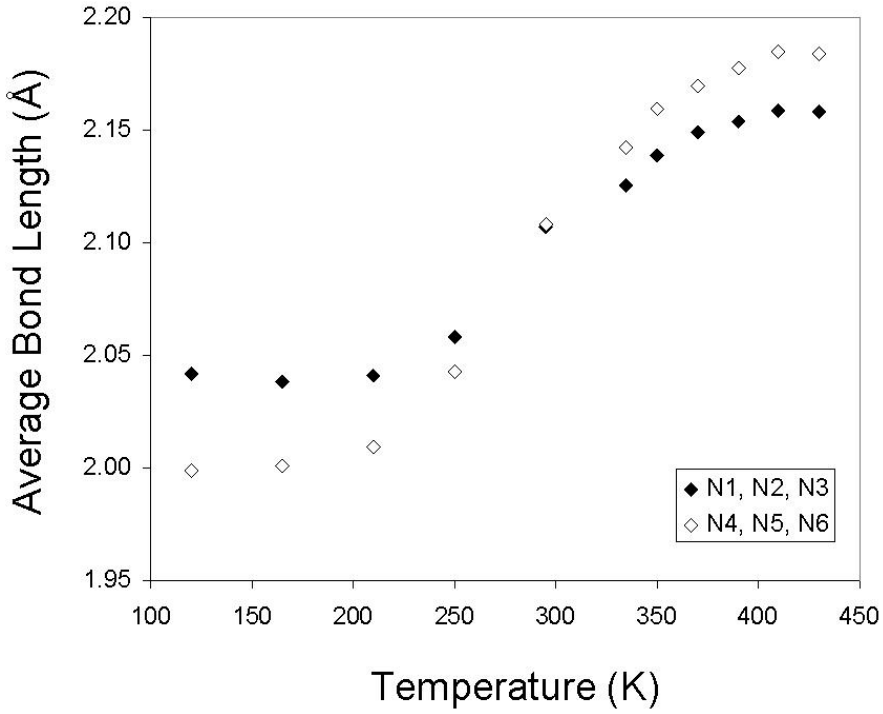

Figure 7.3. Average iron - nitrogen distances for the primary amine (N1, N2, N3) and tertiary amine (N4, N5, N6) bonds as a function of temperature. The standard deviation on all points is less than 0.05 Å

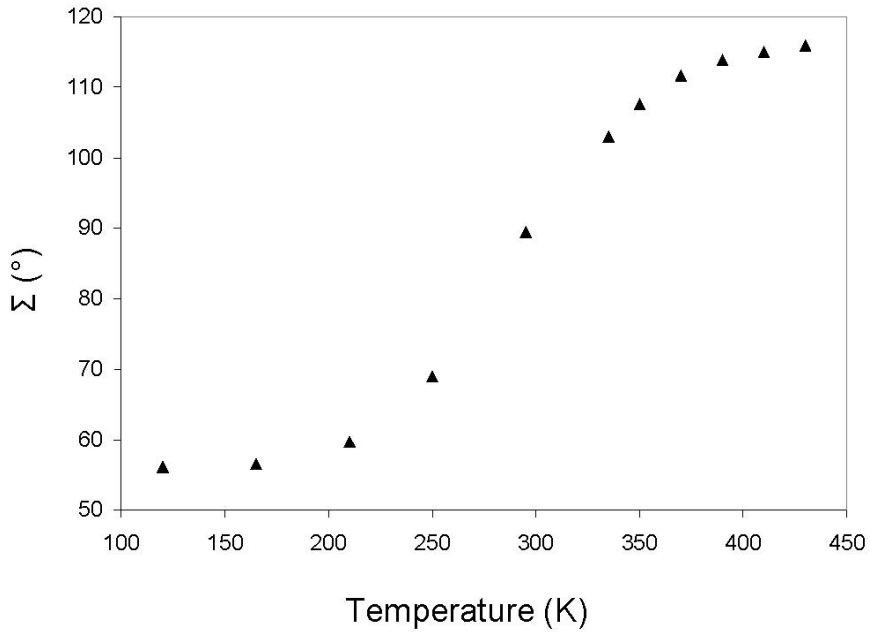

Figure 7.4. Variation of sigma (as defined in the text) as a function of temperature. Errors on all values are contained within the plotted points

The bond lengths and Σ values gradually increase with increasing temperature across the studied temperature range. The values of Σ have been used to construct a spin transition curve, shown in Figure 7.5. Molar fraction of the high spin component was calculated according to Equation 7.1.

$$\gamma_{HS} = \left(\frac{\delta\Sigma_{HL}}{\Sigma_T - \Sigma_{LS}} \right)^{-1}$$

Equation 7.1. Molar fraction of high spin molecules (γ_{HS}) at temperature T. $\delta\Sigma_{HL}$ is the difference in Σ between 430 K and 120K (assumed to be 100% HS and LS respectively).

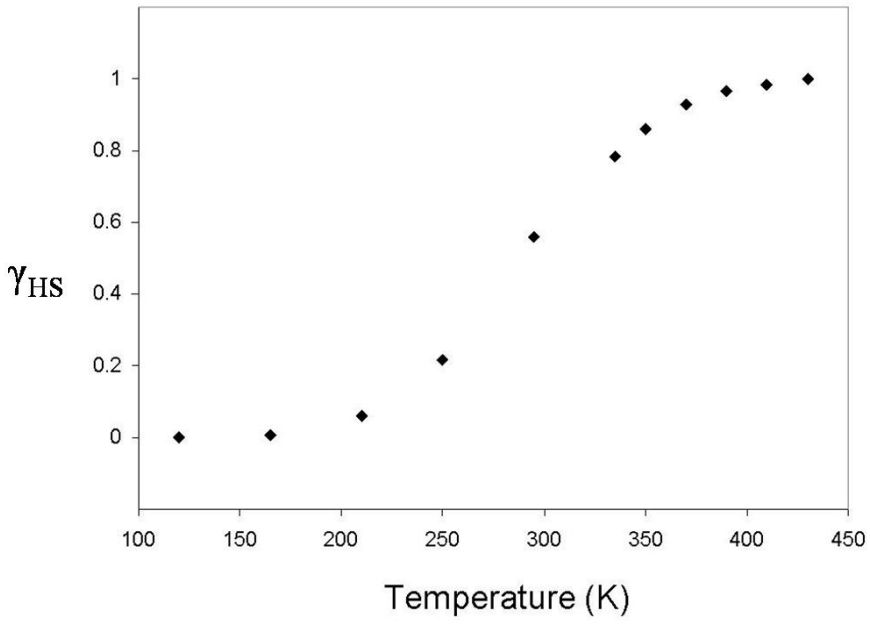

Figure 7.5. A spin transition curve – molar fraction of high spin component (γ_{HS}) versus temperature - calculated from values of Σ, as defined in the text

From the graph, $T_{1/2}$ was calculated to be 287 K. This is very close to the temperature at which the initial structure determination was carried out,[1] and explains why the reported bond lengths appeared to be half way between those characteristic of HS and LS states. The transition is very gradual, occurring over a temperature range of approximately 310 K. This type of gradual transition (Figure 1.7a) is most commonly observed in systems with little or no cooperativity between metal sites.

7.3.2 Cooperativity

In order to explain the gradual nature of the spin transition in this system the molecular packing was examined to get a qualitative understanding of the cooperativity apparent within the lattice. Cooperativity has previously been explained in terms of the degree of 'communication' between SCO centres throughout the crystal. This communication can occur through covalent bonding (for example in multinuclear systems and coordination polymers), hydrogen bonding networks, π-stacking interactions or through short intermolecular contacts (where interatomic distances are less than the sum of the Van der Waals radii).[8]

The crystal packing of this system across the whole temperature range is dominated by CH…O short contacts and NH…O hydrogen bonding interactions between the ligand and the perchlorate counterions. Indeed these are the only type of interaction between atoms at a distance which is less than the sum of the Van der Waals (VdW) radii within the structure; Figure 7.6 shows the iron-containing complex and all molecules that lie within this distance. There are no direct contacts between adjacent $[Fe(L2)]^{2+}$ ions and, as a consequence, short range cooperative interactions between metal centres are expected to be weak.

The disorder in the perchlorate counterions suggests that the interactions between these groups and the complex are not strong enough to fix them into a single orientation. Consequently any internal pressure caused by a change in spin state can be accommodated by a reorientation of the neighbouring perchlorate groups and will not be transmitted to adjacent cations in the lattice.

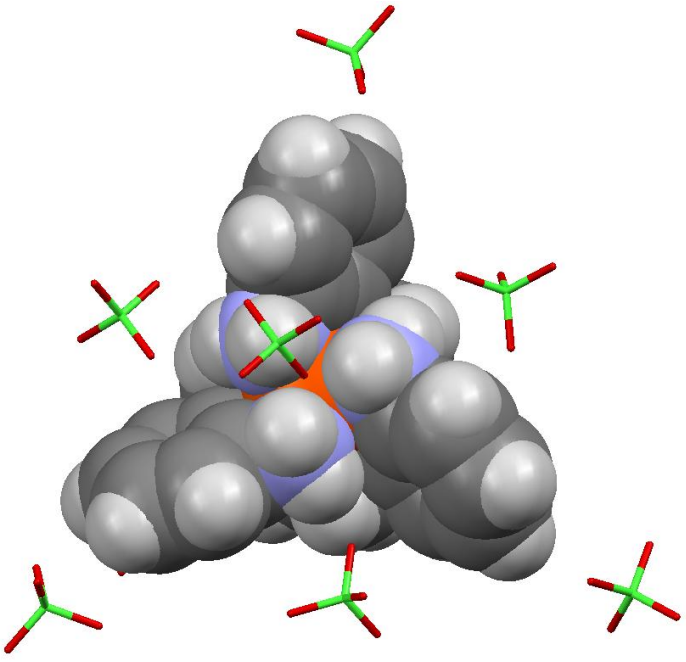

Figure 7.6. A view of the [Fe(1,4,7-tris(2-aminophenyl)-1,4,7-triazacyclononane)]$^{2+}$ cation (space filling model), also showing all molecules at a distance less than the sum of the VdW radii from it

7.3.3 Colour

Iron^{II} systems are typically yellow in the high spin state and red in the low spin state. Crystals of the title compound are blue in colour, a feature which was attributed in the 2000 paper to trace impurities of Fe^{III} resulting from partial oxidation of the corresponding Fe^{II} species, or as a result of trace impurities of Fe^{III} in the original Fe^{II} starting material. There was a broadening of the NMR spectra for this compound that was attributed to paramagnetism associated with the Fe^{III} impurities, although paramagnetism may also be observed if there is Fe^{II} in the HS state within the sample, which has been shown to be the case in this study. Often in Fe^{II} SCO species, a colour change is observed on undergoing the spin transition from the lighter yellow high temperature HS species to the darker red low temperature LS species. This light-to-dark colour change was also observed in this sample, although it remained blue throughout. Photographs of the crystal at varying temperatures may be seen in Figure 7.7. It would be useful to quantify this colour change using UV-Vis spectroscopy or diffuse reflectance measurements, which should form part of any future studies on this sample.

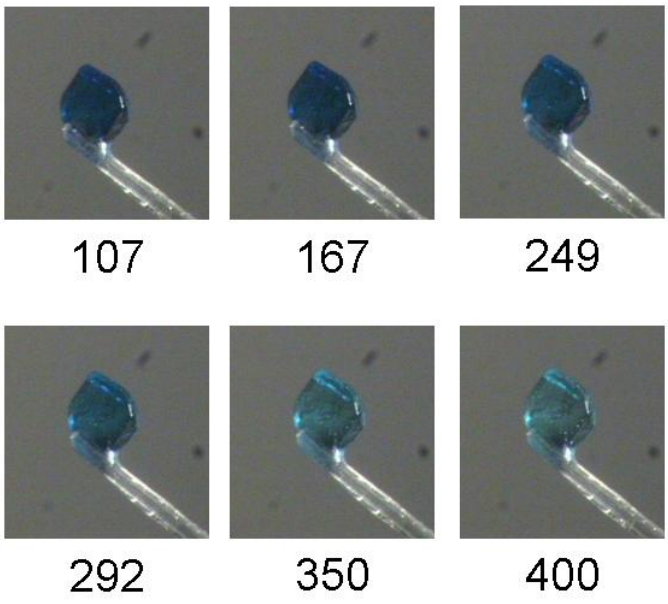

Figure 7.7. Variation in crystal colour as a function of temperature. Numbers indicate the temperature in Kelvin at which the photograph was taken

7.3.4 Magnetism

Variable temperature dc magnetic susceptibilities were measured on a Quantum Design MPMS-5 SQUID magnetometer, at the ICMCB (Bordeaux) under a field of 10 kOe, over a temperature range of 10-350 K. Crystals of the sample (1.52 mg) were sealed in a 30 µm thick low density polyethylene (PELD) plastic bag (11.026 mg). Weights were accurately measured with a Mettler-Toledo MX5 microbalance. The full SQUID temperature range was not available due to the melting point of the PELD film at ~ 385 K, the measurement was thus limited to a maximum of 350 K. The measured magnetic moment was corrected for the contribution of the plastic bag, given by an independent fit of a massive PELD sample which shows a diamagnetic contribution with a small paramagnetic tail.

The obtained curves for molar susceptibility χ_M and its product with temperature are shown in Figure 7.8 as a function of temperature. The $\chi_M T$ value at 350 K of 2.71 cm^3 K mol^{-1} is below the usual values expected for high spin Fe^{II}; the spin crossover is not complete at that temperature. The observed spin crossover is very gradual, with $T_{1/2}$ being between 275 K and 290 K, and the low temperature plateau not being reached until 150 K. The $\chi_M T$ value at 10 K of 0.014 cm^3 K mol^{-1} indicates that the remaining high spin fraction at low temperatures should be very small. The χ_M susceptibility curve shows indeed a very small paramagnetic tail below 75 K. If it is assumed that the spin crossover to LS Fe^{II} is complete, this tail would be accounted for with as little as 0.3% Fe^{III} impurities (with a Curie constant of 4.38 cm^3 K mol^{-1} for a HS Fe^{III} complex). It is impossible through magnetic measurements alone to differentiate between residual HS Fe^{II} and impurities of Fe^{III}. Mössbauer spectroscopy could be used to unambiguously differentiate between these two ions in the sample.

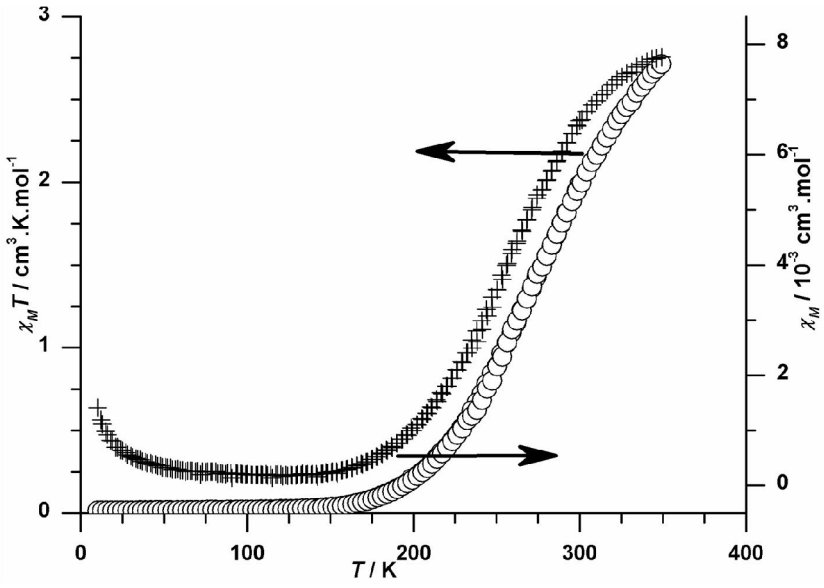

Figure 7.8. Graph showing magnetic behaviour as a function of temperature. $\chi_M T$ vs. T. is plotted as circles, χ_M vs. T. is plotted as crosses

7.4 Conclusions and Perspectives

The structure of [Fe(L2)]2ClO4 has been determined at eleven temperatures across a temperature range of 120 K to 430 K. The study revealed the presence of a previously unidentified spin transition, which was subsequently confirmed using magnetometry. A spin transition curve was constructed using geometrical parameters derived from diffraction data, revealing a very gradual transition. The gradual nature of the transition has been attributed to poor cooperativity between metal centres, evidenced by the lack of intramolecular interactions of any kind between $Fe(L2)^{2+}$ ions. There is no change in crystallographic symmetry of the material across the investigated temperature range, reinforcing the second order nature of the transition.

The spin transition is located around room temperature; $T_{1/2}$ is calculated to be 287 K from diffraction data and between 275 K and 290 K from magnetic measurements. Given that room temperature operation is a desirable property for SCO complexes to possess for potential applications including molecular electronics and data storage,[9] and that the ligand field induced by L2 is such that room temperature SCO is possible, this compound may be of interest for further investigation. If cooperative interactions between metal centres could be increased, the spin transition may become more abrupt

and include hysteretic behaviour, which would make its properties more conducive to such applications.

Future work on this species should focus on increasing the cooperative interactions present within the crystal. This could be achieved through exchanging the perchlorate counterions for dianionic species, reducing the ratio of anions to complex cations and hence increasing the likelihood of non-bonding short contacts between the cations. It should be noted that changing the non-coordinated anion has previously been shown to affect the SCO properties in a manner which is not always predictable, and while the ligand field is in the main conferred by the coordinating environment, there is also a contribution from the out-of-sphere anions, making a rational approach somewhat more difficult.[10,11]

Modifying the ligand to include a greater number of iron SCO centres may also help to increase the cooperativity of the system, although this would also change the ligand field in an unpredictable manner. Increasing the dimensionality of the species into multinuclear clusters or 1, 2 and 3-D coordination polymers has been shown to help the cooperativity of spin crossover systems,[12] and as such merits further investigation.

---

[1] I. A. Fallis, R. D. Farley, K. M. A. Malik, D. M. Murphy and H. J. *Smith J. Chem. Soc., Dalton Trans*., 2000, 3632

[2] P. Guionneau, M. Marchivie, G. Bravic, J. F. Létard and D. Chasseau, *Top. Curr. Chem*., 2004, 234, 97

[3] J. Cosier and A. M. Glazer, J. *Appl. Crystallogr.,* 1986, **19**, 105

[4] *SMART-NT, Data Collection Software, version 6.1,* Bruker Analytical X-ray Instruments Inc., Madison, WI, USA, 2000

[5] *SAINT-NT, Data Reduction Software, version 6.1*, Bruker Analytical X-ray Instruments Inc., Madison, WI, USA, 2000

[6] G. M. Sheldrick, *Acta Cryst*., 2008, **A64**, 112

[7] O. V. Dolomanov, L. J. Bourhis, R. J. Gildea, J. A. K. Howard, H. Puschmann, *J. Appl. Cryst.*, 2009, **42**, 339

[8] J. A. Real, A. B. Gaspar, V. Niel, M. C. Muñoz. *Coord. Chem. Rev.*, 2003, **236**, 121

[9] J.-F. Létard, P. Guionneau and L. Goux-Capes, *Top. Curr. Chem.*, 2004, **235**, 221

[10] M. Yamada, H. Hagiwara, H. Torigoe, N. Matsumoto, M. Kojima, F. Dahan, J.-P. Tuchagues, N. Re, and S. Iijima *Chem. Eur. J.*, 2006, 12, 4536

[11] G. Lemercier, N. Bréfuel, S. Shova, J. A. Wolny, F. Dahan, M. Verelst, H. Paulsen, A. X. Trautwein, and J.-P. Tuchagues, *Chem. Eur. J.*, 2006, **12**, 7421

[12] K. S. Murray and C. J. Kepert, *Top. Curr. Chem.*, 2004, **233**, 195

8 Additional Studies of Spin Crossover Complexes

8.1 [Fe(bbp)$_2$]2(NCSe)•4,4'-bipy

A crystalline sample of [Fe(bbp)$_2$]2(NCSe)•4,4'-bipy (where bbp = 2,6-bis(parazol-3-yl)pyridine) (**1**), shown in Figure 8.1, was obtained from Dr Patrick Rosa of the ICMCB. A previous crystallographic study by Dr. Rosa[1] has shown that this complex undergoes a partial spin transition from 100% HS at to a mixed spin state with one third of the iron centres in the LS state and two thirds in the HS state. This transition occurs between 150 K and 100 K. This partial spin transition is accompanied by a crystallographic phase transition which increases the unit cell volume by a factor of three, resulting in three independent iron sites and an ordered mixed spin state.

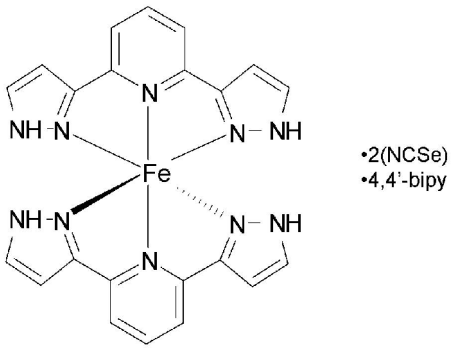

Figure 8.1. [Fe(bbp)$_2$]2(NCSe)•4,4'-bipy

The purpose of the investigation of this sample in Durham was to determine if the mixed spin phase was an intermediate plateau in a stepped SCO system, with further steps occurring below the accessible temperature range for the diffraction equipment in Bordeaux and to ascertain if the system showed LIESST behaviour. In the absence of magnetic data, a crystallographic study was performed at 30 K using the Oxford Cryosystems Helix[2] after cooling at 60 K/hour from room temperature.

At 30 K the structure of **1** was comparable to that previously found at 100 K, revealing that there is no further spin transition or crystallographic phase transition down to this temperature. After irradiation with a green laser (532 nm, 10 mW) for 2 hours a short data collection revealed a structure with no significant differences to those found at 30

K. Without magnetic data to confirm whether or not this sample shows LIESST behaviour, no further low temperature investigations were performed.

This sample was further studied under high pressure using the diamond anvil cell. A single crystal was loaded into the cell in the manner previously described. Upon pressurisation the crystal changed in colour from yellow (observed at ambient pressure) to red at elevated pressure and finally to black, as shown in Figure 8.2.

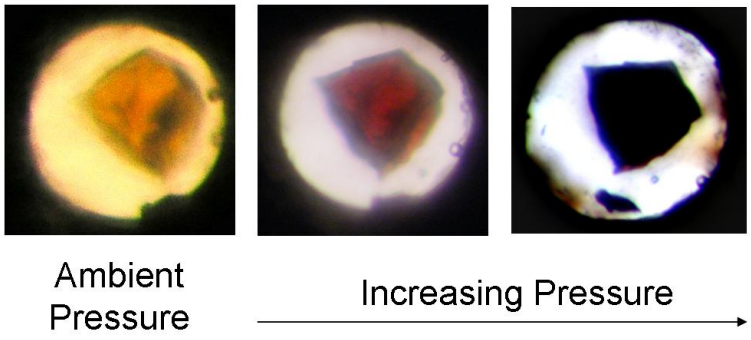

Figure 8.2. Colour change observed in 1 on increasing pressure

A diffraction pattern was recorded of the sample at pressures equating to both the red and the black phases. Diffraction from the sample was very weak and resolution was limited to 20° in 2θ. The high pressure red phase equated to a different cell than either of the two thermally accessible phases and has a volume comparable to that of the mixed spin phase (three times the volume of the room temperature fully high spin phase). The unit cell associated with the high pressure black phase could not be determined. The unit cell parameters are shown in Table 8.1 along with those of the known thermally accessible phases. Due to the limited resolution of the data, the triclinic unit cell and the large number of parameters expected for a cell with such a large volume, further data processing of the data and structure solution were not attempted.

Table 8.1. Summary of the cell parameters and spin state of 1 at 150 K, 100 K and at high pressure

	150 K	100 K	High Pressure
Spin State	HS	⅔HS, ⅓LS	
a/Å	8.52(1)	8.46(1)	14.15(1)
b/Å	13.82(1)	25.34(1)	17.04(1)
c/Å	17.66(1)	25.73(1)	23.44(1)
α/°	109.70(1)	76.31(1)	69.03(1)
β/°	94.44(1)	89.70(1)	77.18(1)
γ/°	105.30(1)	84.53(1)	75.60(1)

In this preliminary study it is clear that the structural behaviour of the sample under pressure is different from that observed thermally. A further investigation of this system using a higher intensity source would be beneficial to the understanding of how spin crossover is influenced by pressure and to the wider question of structure-property correlations in SCO systems. Employing a variety of techniques including high pressure Raman, Mössbauer and magnetometry studies would aid in the development of a wider picture of how this sample behaves across a wide range of temperatures and pressures.

8.2 [Fe(bbp)(NCSe)$_2$]•4,4'-bipy

Crystals of the previously unknown compound [Fe(bbp)(NCSe)$_2$]•4,4'-bipy (**2**) (Figure 8.3) were obtained from the same pot as [Fe(bbp)$_2$]2(NCSe)•4,4'-bipy. The Fe^{II} centre is in the HS state down to 30 K, evidenced by the bond lengths and the yellow colour of the sample. To the best of our knowledge there are no reported five coordinate Fe^{II} complexes that exhibit spin crossover behaviour and consequently the lack of a spin transition in this sample is not unexpected.

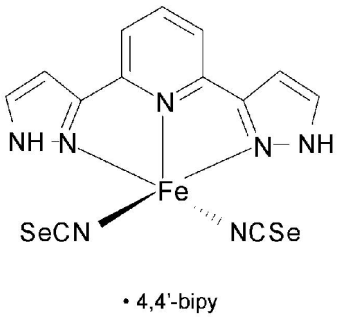

Figure 8.3. [Fe(bbp)(NCSe)2]•4,4′-bipy (2)

The asymmetric unit at all temperatures consists of one [Fe(bbp)(NCSe)$_2$] molecule and an uncoordinated 4,4′-bipyridine ligand. These molecules form dimers involving the amine group of the bbp ligand and the nitrogen atoms of the free bipyridine, as shown in Figure 8.4. Hydrogen bonding distances and angles are given in Table 8.2.

Table 8.2. Hydrogen bond geometries for 2

D-H···A	H···A (Å)	D···A (Å)	D-H···A (°)
N1-H1A···N8	1.919(3)	2.796(4)	173.9(2)
N5-H5···N9^{i}	1.928(3)	2.802(4)	171.8(2)

Symmetry codes: i = 1-x, 1-y, -z

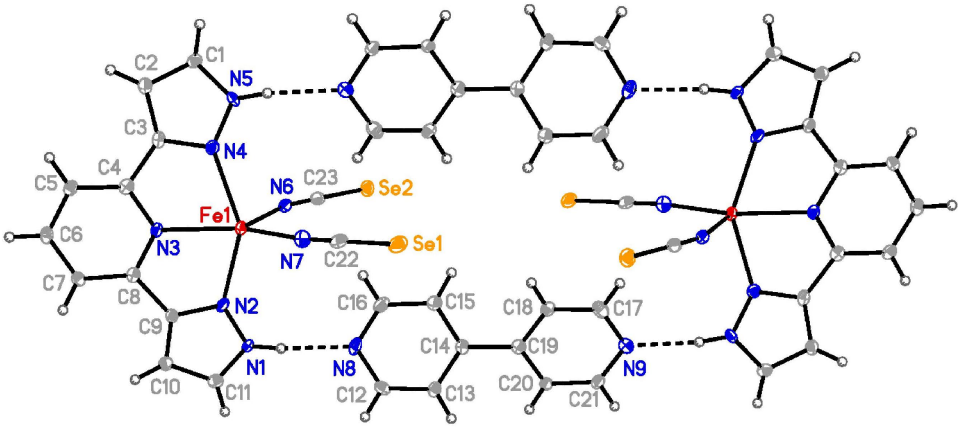

Figure 8.4. Hydrogen bonded dimer of 2 at 30 K. ADPs are drawn at 50% probability. Only unique atoms are labelled

There is an additional short contact present between Se1 and Fe1′ of a symmetrically equivalent molecule (-x, 2-y, -z), shown in Figure 8.5. The Fe – Se distance is 3.4481(6)

Å, which is more than 1 Å longer than the average Fe – Se bond distance found in the literature.[3]

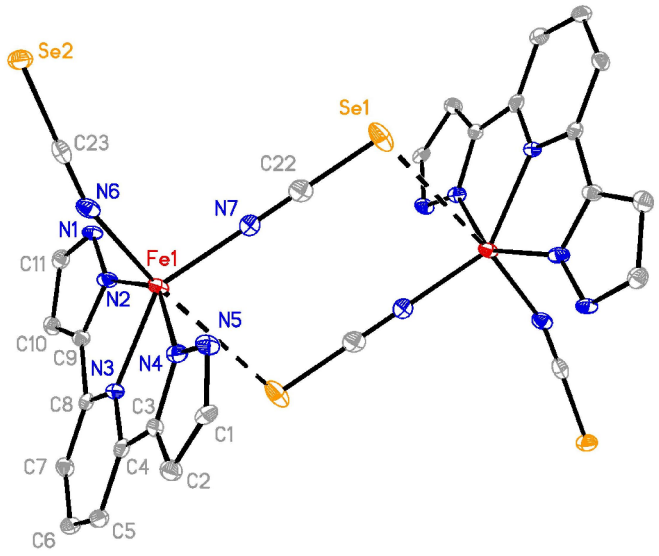

Figure 8.5. Short contacts formed between iron and selenium in 2 at 30 K

Under pressure this sample also changes colour from yellow to red, implying a change from high to low spin. As mentioned previously, it is unprecedented for five-coordinate Fe^{II} to undergo spin crossover. It would seem more likely that an increase in pressure induces a change in the coordination environment at the iron centre to include the selenium of the adjacent molecule, creating a dimer of two six-coordinate Fe^{II} centres in a LS ground state. Unfortunately data could not be collected from the sample in this state as there was no obvious diffraction from the sample observable. This may be the result of the relatively low intensity of X-rays available using the in-house diffractometer or result from disintegration of the crystal following a reconstructive phase transition.

Further investigation of this sample under high pressure, again using a variety of techniques would reveal whether this hypothesis of the formation of an Fe – Se bond is indeed the case. Spin crossover resulting from a change in the coordination sphere within the crystalline state has been reported before, but it is not very common.[4]

Table 8.3. Crystallographic information for 2

	[Fe(bbp)(NCS)$_2$].bipy		
Empirical formula	$C_{23}H_{17}N_9Se_2Fe$		
Temperature /K	30(2)		
Crystal system	Triclinic		
Space group	Pī		
a/Å, b/Å, c/Å	8.6713(15),	11.909(2),	12.713(2)
α/°, β/°, γ/°	82.397(3),	79.668(3),	70.100(3)
Volume/Å^3	1210.9(4)		
Z	2		
ρ_{calc}mg/mm^3	1.737		
μ/mm^{-1}	3.660		
Crystal size/mm	0.19 × 0.18 × 0.11		
Theta range for data collection	1.82 to 27.04°		
Reflections collected	6895		
Independent reflections	4668		
R_{int}	0.0247		
Data/restrains/parameters	4668/0/316		
Goodness-of-fit on F^2	1.027		
Final R indexes [I>2σ (I)]	R_1 = 0.0376, wR_2 = 0.0867		
Final R indexes [all data]	R_1 = 0.0532, wR_2 = 0.0934		
Largest diff. peak/hole /e·Å^{-3}	0.783/-0.534		

8.3 [Fe(L3)(CN)$_2$]•H$_2$O

A complex in which spin crossover properties *do* originate in a change of coordination at the metal centre is [Fe(L3)(CN)$_2$]•H$_2$O (where L3 = [2,13-dimethyl-6,9-dioxa-3,12,18-triazabicyclo[12.3.1]octadeca-1(18),2,12,14,16-pentaene) (**3**), shown in Figure 8.6. As described in Chapter 1.5, this compound has the highest known T_{LIESST} of any mononuclear species published to date.[5] The thermal spin transition behaviour has been studied previously using diffraction techniques.[4] A complete thermal spin transition is associated with a reversible breaking of one Fe – O bond, changing from a seven-coordinate species in the HS state, to six-coordinate in the LS state.[4,6] It is also possible to achieve a partial spin transition if the species is cooled through the temperature range at a slower rate.

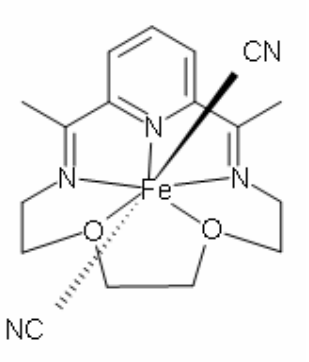

Figure 8.6. $[Fe(L3)(CN)_2]\cdot H_2O$, 3

It has been noted by P. Guionneau *et al.* that the change in volume of the coordination polyhedron upon thermal spin crossover is the largest known to date.[4] However this massive change in volume is not manifested on the macroscopic scale, with a total decrease in the volume of the sample within the usual range expected for species exhibiting spin crossover behaviour. It was decided to examine the sample under hydrostatic pressure in an attempt to investigate if the differences in the volume of the HS and LS states might be exploited using this technique. A crystalline sample of **3** was obtained from Dr. Philippe Guionneau at the ICMCB in Bordeaux. A suitable single crystal was selected, cut to the appropriate dimensions to fit within the confines of the gasket and loaded into the DAC using the methods detailed in Chapter 2.3.

No colour change was observed as a result of increasing the pressure although the sample is a very deep red under atmospheric conditions; any darkening of the crystal resulting from a spin transition would not necessarily be obvious. The structure of the **3** at 6.5 kbar is isostructural with that from the literature determined under ambient conditions.[4] The structure at 6.5 kbar is shown in Figure 8.7, and selected structural parameters are shown in Table 8.4 along with those of the HS and LS structures published previously.[4,7]

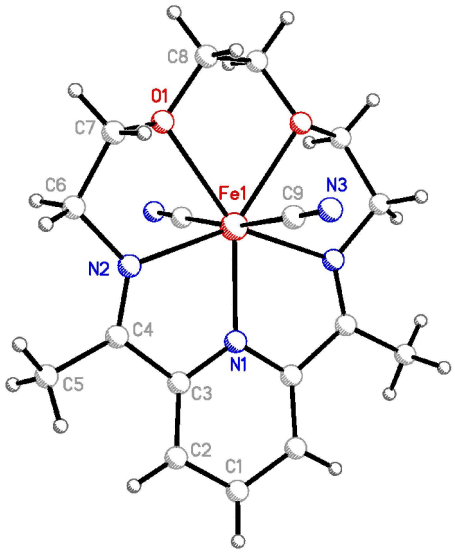

Figure 8.7. Molecular structure of $[Fe(L3)(CN)_2]$ at 6.5 kbar. Only unique atoms are labelled

Table 8.4. Selected structural parameters for 3

	6.5 kbar	Thermal HS[7]	Thermal LS[4]
Fe1 – N1 (Å)	2.11(1)	2.113(2)	1.836(2)
Fe1 – N2 (Å)	2.210(8)	2.213(1)	1.914(2) 2.058(2)
Fe1 – O1 (Å)	2.342(7)	2.341(2)	2.243(1) 3.202(2)
Fe1 – C9 (Å)	2.16(1)	2.215(2)	1.960(2) 1.956(2)
V_{coord} (Å^3)	17.2(1)	17.0(1)	10.0(1)
Unit Cell Volume (Å^3)	1909(1)	1896.2(1)	1793.9(1)

The volume of the unit cell is slightly larger at 6.5 kbar than at ambient pressure, which is highly unusual and may point towards anomalies in the data rather than a real increase in the volume. As described in Chapter 2.3.9, pressure was measured after the diffraction experiment and hence the measured pressure may not be equal to the pressure applied to the sample during the X-ray diffraction data collection. In spite of this unexpected behaviour it is clear from the volume of the coordination polyhedron, the bond lengths and the fact that the iron centre is still seven-coordinate that during

the diffraction experiment the iron centre was still in the HS state. Selected crystallographic parameters for **3** at 6.5 kbar are given in Table 8.5.

When the pressure is further increased the quality of the diffraction from the sample is substantially reduced and even unit cell determination proved impossible. It is possible that this may be a result of a significant reconstructive phase transition possibly resulting from a spin transition, but further experiments using a variety of techniques would be required to further explore the behaviour of this complex under high pressure. The use of high pressure magnetic and Mössbauer measurements would be invaluable to determine if it is possible to induce the LS state using pressure. If it is possible to achieve this LS state, high pressure Raman and powder diffraction techniques may shed light upon the structure of this phase, even if the phase transition is destructive in single crystals.

Table 8.5. Selected crystallographic parameters for $[Fe(L3)(CN)_2]\bullet H_2O$ at 6.5 kbar

$[Fe(L3)(CN)_2]\bullet H_2O$ at 6.5 kbar	
Empirical formula	$C_{17}H_{21}N_5FeO_3$
Formula weight	1701.27
Crystal system	Monoclinic
Space group	C2/c
a/Å, b/Å, c/Å	17.373(2), 12.0817(13), 10.1573(15)
β/°	116.387(9)
Volume/Å^3	1909.8(4)
Z′ / Z	1 / 2
Crystal size/mm^3	0.11 × 0.19 × 0.21
Theta range for data collection	4.25 to 21.92°
Reflections collected	2399
Independent reflections	697 R_{int} = 0.0555
Data/restraints/parameters	697/132/125
Goodness-of-fit on F^2	1.124
Final R indexes [I>2σ (I)]	R_1 = 0.0825 wR_2 = 0.2256
Final R indexes [all data]	R_1 = 0.1026 wR_2 = 0.2497
Largest diff. peak/hole / e Å^{-3}	0.674/-0.725

[1] Dr P. Rosa ICMCB, CNRS, Université Bordeaux 1, 87, Avenue du Dr. A. Schweitzer 33608 Pessac cedex, France, *Private Communication*

[2] A. E. Goeta, L. K. Thompson, C. L. Sheppard, S. S. Tandon, C. W. Lehmann, J. Cosier, C. Webster and J. A. K. Howard, *Acta Cryst.*, 1999, **C55**, 1243

[3] Cambridge Structural Database Version 5.30

[4] P. Guionneau, F. Le Gac, A. Kaiba, J. Sánchez Costa, D. C. and J.-F. Létard, *Chem. Commun.*, 2007, 3723

[5] S. Hayami, Z.-Z. Gu, Y. Einaga, Y. Kobayashi, Y. Ishikawa, Y. Yamada, A. Fujishima and O. Sato, *Inorg. Chem.*, 2001, **40**, 3240

[6] S. M. Nelson, P. D. A. McIlroy, C. S. Stevenson, E. König, G. Ritter and J. Waigel, *J. Chem. Soc. Dalton Trans.*, 1986, 991

[7] P. Guionneau, J. Sánchez Costa and J.-F. Létard, *Acta Cryst.*, 2004, **C60**, m587

9 Concluding Remarks and Future Work

It is clear that structure and properties are intrinsically linked for spin crossover (SCO) compounds. Understanding structural phase transitions and cooperative interactions is vital to elucidating the mechanism of the SCO phenomenon in the solid state. Identifying the mechanism of this process is necessary in order to develop this class of materials towards potential applications. X-ray diffraction techniques provide a means of studying these species at a molecular level, providing insights into how specific structural features alter the SCO behaviour of many transition metal compounds.

The crystallographic phase transitions that often accompany spin transitions can lead to deterioration in the crystal quality, disorder and twinning, all of which can make structure solution and refinement from single crystal X-ray diffraction data rather more complicated. However, a full and accurate description of the structure can often yield significant information about the system, which cannot be obtained using other techniques. This was demonstrated by the five different structural phases observed in [{Fe(bbp)$(NCS)_2$}$_2$4,4'-bipy]2MeOH (Chapter 3). Close attention to the symmetry and space group of the mixed spin phase was required to reveal that the distribution of high spin (HS) and low spin (LS) iron centres was ordered throughout the lattice. In this case, a structural phase transition is decoupled from the spin transition, occurring at a significantly higher temperature. This phase transition breaks the inversion symmetry of the molecule, resulting in two crystallographically inequivalent iron centres in the dinuclear molecule prior to the phase transition. The symmetry breaking provides a mechanism through which the ordering of the mixed spin phase can be rationalised. The application of hydrostatic pressure to this species results in a spin transition to a 100% LS state, which is not thermally accessible and shows no evidence of the symmetry breaking structural phase transition that is observed in the thermal behaviour of this compound. Comparison between the thermal evolution of the complex and its behaviour under pressure provides information as to how the structural phase transitions can influence SCO properties.

An ordered mixed spin phase is also observed in the thermal behaviour of [Fe(bapbpy)$(NCS)_2$] (Chapter 4). Determination of the meta-stable high spin (HS*) state in this species also required careful treatment of the crystallographic data as a

result of the multiple structural phase transitions observed. As a result of incomplete conversion to the HS* state, it was necessary to distinguish diffraction from this phase from that of the residual LS component, which is further complicated by the presence of non-merohedral twinning in the LS phase. The study proved that the HS* state is isostructural with the high temperature HS state, rather than any of the other thermodynamically stable structures observed in this species.

Continuing the theme of stepped spin transitions and ordered intermediate states, the Ferric species $[Fe^{III}(L1)]ClO_4$ (Chapter 5) was studied by variable temperature single crystal and powder diffraction. Single crystal studies revealed an ordered intermediate phase with a ratio of ⅔ HS to ⅓ LS. A subsequent transition of a further ⅓ of the iron centres to the LS state occurs at lower temperature, but unfortunately the crystal is destroyed during the transition. Powder diffraction studies reveal that the contraction in volume of the species during the second transition is of comparable magnitude to the first; unfortunately these data were not of sufficient quality to determine if this mixed spin phase is also ordered.

It is interesting to note that the first phase transition in $[Fe^{III}(L1)]ClO_4$ is structurally similar to that observed in $[Fe(bapbpy)(NCS)_2]$. Both species are in the space group C2/c in the HS phase at high temperature, with the Fe atom sitting on a site of 2-fold symmetry, resulting in an asymmetric unit consisting of half a molecule ($Z' = ½$). As temperature decreases, a partial spin transition coupled to a crystallographic phase transition results in a tripling of the unit cell volume and an increase in Z' to 1½, creating two crystallographically distinct iron sites. The space group of the larger cell in both cases is also C2/c; the 2-fold symmetry of one of the two metal sites is broken, resulting in a HS:LS ratio of 2:1 for $[Fe^{III}(L1)]ClO_4$ and 1:2 in the case of $[Fe(bapbpy)(NCS)_2]$.

The relationship between structural features and SCO properties was further demonstrated by the investigation of $[Fe(picen)(NCS)_2]$ (Chapter 6). It was possible to determine that the partial spin transitions observed in this species were not ordered, but rather HS and LS Fe^{II} sites were randomly distributed throughout the lattice. This was demonstrated by analysis of the atomic displacement parameters of those atoms which differ most in position between the HS and LS states.

The percentage conversion from the HS to LS state in [Fe(picen)$(NCS)_2$] is dependent on the rate of cooling of the sample and was determined structurally through analysis of the volume of the Fe-N_6 octahedron. In cases such as these, where the HS and LS states are not crystallographically distinguishable (in which the occupancy of each state cannot be explicitly refined), this method provides a way of determining the relative proportion of iron centres in each spin state.

The HS* state of [Fe(picen)$(NCS)_2$] proved it to be isostructural with the high temperature HS structure. It would appear that faster rates of sample cooling result in partial conversion to this HS* state, mediated by the fact that no structural phase transition is involved. This behaviour is believed to be possible as a result of the temperature of the thermal spin transition ($T_{½}$) and the temperature at which the HS* state rapidly decays (T_{LIESST}) being similar.

Like [Fe(picen)$(NCS)_2$], the species [Fe(L2)]$2ClO_4$ (Chapter 7) also shows a SCO mechanism involving a random distribution of spin states throughout the crystal. In this case the spin transition is very gradual, occurring across a range of more than 200 K, located across room temperature. Indeed it was structural features of the room temperature species that first alluded to the SCO properties seen in this sample. The bond lengths at room temperature were intermediate between those expected for HS and LS states, and were shown in this study to be directly correlated to the spin state. Again, structural parameters (in this case Σ values) were used to determine the proportions of HS and LS iron centres in the lattice as a function of temperature, and hence construct a spin transition curve.

The gradual nature of the spin transition in [Fe(L2)]$2ClO_4$ has been rationalised in terms of the structural behaviour of the complex. Not only is there no crystallographic phase transition observed within the temperature range of the spin transition, but it is also evident that cooperative interactions between iron sites are weak.

A series of preliminary investigations on a range of Fe^{II} species under hydrostatic pressure have also been undertaken (Chapter 8). While few structural conclusions can be drawn at this stage, it is clear that pressure has a strong effect on these species and significant further work in the area of pressure induced spin transitions is clearly merited.

Future Work

Many of the suggestions made for future work in Chapters 3 to 8 will be attempted during postdoctoral work at the CNRS institutions Laboratoire de Chimie de Coordination, in Toulouse and the Institut de Chemie de la Matière Condensée de Bordeaux, France. The primary objectives of these studies will be to thoroughly characterise a range of spin crossover samples under high pressure using a variety of techniques, including Raman spectroscopy, magnetic susceptibility and X-ray diffraction.

We intend to explore how pressure affects spin crossover, and how this differs when a material under pressure is subject to non-linear phenomena, such as crystallographic phase transitions. The mechanism of spin crossover is hoped to be better understood by examining the interactions that are present throughout the sample and hence provide targets in the development of SCO materials with properties better suited to potential applications.

Appendix A Additional Information

Courses Attended

- 08/2006 The UK Molecular Magnets Network 3rd meeting, University of Edinburgh
- 01/2007 The BCA/PCG Rietveld Refinement Workshop, Durham University.
- 04/2007 The 11th BCA/CCG Intensive Course in X-ray Structural Analysis, Durham Universtiy.
- 06/2009 Erice International School of Crystallography – High Pressure Crystallography.

Conferences Attended

- 11/2006 CCG Autumn Meeting, University of Glasgow, UK
- 04/2007 BCA Spring Meeting, University of Kent at Canterbury, UK
- 04/2008 BCA Spring Meeting, University of York, UK
- 08/2008 21st Congress of the International Union of Crystallography, Osaka, Japan.
- 11/2008 CCG Autumn Meeting, University of Newcastle-Upon-Tyne, UK
- 04/2009 BCA Spring Meeting, University of Loughborough, UK

Poster and Oral Presentations Outside Durham University

- 04/2007 **Poster** Structural Studies of Spin Crossover Dinuclear Fe(II) Complexes. BCA Spring Meeting, Canterbury.

- 04/2007 **Oral** Thermal And Light-Induced Spin Crossover In Fe (II) Networks. BCA Spring Meeting, Young Crystallographers Group, Canterbury.

- 04/2008 **Poster** Manipulating Spin States of a Dinuclear Fe(II) Complex BCA Spring Meeting, York. **Awarded the poster prize from the Chemical Crystallography Group for best poster.**

- 08/2008 **Poster** Structural Studies Of Spin Crossover Compounds Under Extreme Environmental Conditions. IUCr Congress, Osaka, Japan. **Awarded the Oxford Cryosystems low temperature poster prize.**

- 04/2009 **Poster** Structure-property correlations in Spin Crossover Complexes. BCA Spring Meeting, Loughborough.

- 04/2009 **Poster** Structure-Property Correlations in Spin Crossover Complexes. International Review of Chemistry, Leeds – representing Durham University as a young academic.

Publications

- *Alkyl and Aryl Dicationic Derivatives of Cyclic Triphosphenium Ions.* Keith B. Dillon, Andrés E. Goeta, Judith A. K. Howard, Philippa K. Monks, Helena J. Shepherd and Amber L. Thompson, *Dalton Trans.*, 2008, 1144. **Cited as a Hot Article.**

- *Crystal and Molecular Structures of Some Six-Coordinate Tin(IV) Halogeno Complexes with Phosphorus Containing Ligands.* A. S. Batsanov, R. M. K. Deng, K. B. Dillon, A. E. Goeta, J. A. K. Howard, J. Meldrum, P. K. Monks, H. Puschmann, and H. J. Shepherd, *Heteroatom Chemistry*, 2009, **20**, 3, 136

- *The Synthesis, Crystal and Molecular Structures of Two Saccharinate-Metal Complexes with Dipyridylamine as a Co-Ligand.* R. K. Deng, K. B. Dillon, A. E. Goeta, M. Mapolelo and H. J. Shepherd, *Inorg. Chim. Acta*, 2009, **362**, 5109

- *The Molecular Structure of a 2-aryl-1,3,2-dioxyphospholane and its Coordination Behaviour Towards Platinum(II) Species.* K. B. Dillon, A. E. Goeta, P. K. Monks and H. J. Shepherd, *Polyhedron*, 2010, **29**, 606

- *Saccharinate – Metal Complexes with 1,10-phenanthroline (phen) or 2,2'-bipyridine (bipy) as co-ligands; the Synthesis and Crystal and Molecular Structures of* $[M(phen)_2(H_2O)_2]\ (sac)_2.\ H_2O$ *(M = Co or Zn),* $[Cd(phen)_2(sac)(H_2O)]\ (sac).\ H_2O$*,* $[Hg(phen)_2(sac)]\ (sac).\ 2.5\ H_2O.$ *and* $[Hg(bipy)_2(sac)_2].$ A. S. Batsanov, C. Bilton, R. M. K. Deng, K. B. Dillon, A. E. Goeta, J. A. K. Howard, H. J. Shepherd, S. Simon and I. Tembwe. *Submitted to CrystEngComm.*

- *Crystallographic Elucidation of Pure Structural, Thermal and Light-Induced Spin Transitions in an Iron(II) Binuclear Complex.* A. Kaiba, H. J. Shepherd, D. Fedaoui, P. Rosa, A. E. Goeta, J.-F. Létard and P. Guionneau. *Dalton Trans.*, 2010, **39**, 2910

- *A Two-Step Structural Phase and Spin State Transition in a Mononuclear Fe(III) Complex.* S. Shakespeare, H. J. Shepherd, M. Griffin, C. J. Harding, J.-F. Létard, P. Guionneau, A. E. Goeta, H. Müller-Bunz and G. Morgan. *In preparation for Angew. Chem.*

- *Structural Origin of the Gradual Spin Transition in a Mononuclear Iron(II) Complex.* Helena J. Shepherd, Patrick Rosa, Ian M. Fallis and Andrés E. Goeta. *In preparation for CrystEngComm.*

Index to files on Compact Disk – Appendix B

	Crystallographic_Data_Tables
Chapter 3	Phase_1_290_tables.doc
	Phase_2_140_K_tables.doc
	Phase_3_tables.doc
	Phase_4_tables.doc
	Phase_5_17kbar_tables.doc
Chapter 4	Fe_bapbpy_NCS2_HS_fraction_tables.doc
	Fe_bapbpy_NCS2_LS_twin30K_tables.doc
Chapter 5	FeL1_ClO4_160K_tables.doc
	FeL1_ClO4_200K_tables.doc
Chapter 6	Fe_picen_NCS2_120K_HS_tables.doc
	Fe_picen_NCS2_Flash_tables.doc
	Fe_picen_NCS2_Fast_tables.doc
	Fe_Picen_NCS2_medium_tables.doc
	Fe_Picen_NCS2_slow_tables.doc
Chapter 7	120K.doc
	165K.doc
	210K.doc
	250K.doc
	295K.doc
	335K.doc
	350K.doc
	370K.doc
	390K.doc
	410K.doc
	430K.doc
Chapter 8	molecule_2_30K.doc
	Molecule_3_High_Pressure.doc

	Crystallographic_Information_Files
Chapter 3	Phase_1_290.cif
	Phase_2_140_K.cif
	Phase_3.cif
	Phase_4.cif
	Phase_5_17kbar.cif
Chapter 4	Fe_bapbpy_NCS2_HS_fraction.cif
	Fe_bapbpy_NCS2_LS_twin30K.cif
Chapter 5	FeL1_ClO4_160K.cif
	FeL1_ClO4_200K.cif
Chapter 6	Fe_picen_NCS2_120K_HS.cif
	Fe_picen_NCS2_Flash.cif
	Fe_picen_NCS2_Fast.cif
	Fe_Picen_NCS2_medium.cif
	Fe_Picen_NCS2_slow.cif
Chapter 7	120K.cif
	165K.cif
	210K.cif
	250K.cif
	295K.cif
	335K.cif
	350K.cif
	370K.cif
	390K.cif
	410K.cif
	430K.cif
Chapter 8	molecule_2_30K.cif
	Molecule_3_High_Pressure.cif

Files with a .doc extension are Microsoft Word files created using Microsoft Office Professional Edition Word 2003. These are files containing the following crystallographic information for each structure presented herein:

Atomic Coordinates and Equivalent Isotropic Displacement Parameters, Anisotropic Displacement Parameters, Bond Lengths, Bond Angles and Hydrogen Atom Coordinates.

Files with a .cif extension are Crystallographic Information Files (CIFs), created using Olex2. They may be viewed as text or opened using a suitable crystallographic viewer, such as Mercury or Olex2.

A detailed description of the information contained within CIFs is available from the International Union of Crystallography.